

DTIC FILE COPY

4

MRL-R-1055

AR-005-134



DEPARTMENT OF DEFENCE

DEFENCE SCIENCE AND TECHNOLOGY ORGANISATION

MATERIALS RESEARCH LABORATORY

MELBOURNE, VICTORIA

REPORT

MRL-R-1055

AD-A200 995

EXPERIMENTS WITH A SMALL INJECTED RAILGUN

D.F. Stainsby and D.R. Sadedin

DTIC
ELECTE
DEC 07 1988
S & H D

Approved for Public Release

DISTRIBUTION STATEMENT A

Approved for public release
Distribution Unlimited

DSTO
MELBOURNE

C Commonwealth of Australia
JUNE 1987

88 12 6 038

**DEPARTMENT OF DEFENCE
MATERIALS RESEARCH LABORATORY**

**REPORT
MRL-R-1055**

EXPERIMENTS WITH A SMALL INJECTED RAILGUN

D.F. Stainsby and D.R. Sadedin

ABSTRACT

Experiments aimed at gaining insight into the plasma arc and rail damage in railguns are described and discussed. The railgun body was constructed of clear polycarbonate to allow streak photographs of the plasma to be taken. A powder-gun injector was used to reduce initial rail damage. The development of the injector and projectiles is described. Rails with plain surfaces, alternating aluminium inserts, and lengthwise insulating stripes were studied. Both aluminium and copper foils were used for plasma initiation. The results from the experiments enable plasma formation to be explained in terms of the vapourization energy of the foil and material taken up from the bore. Magnetic pick-up coils were used to study plasma length and current distribution and the theory of the coils and a look-up table of calculated waveforms is given. A non-metallurgical study of rail damage has been made, and damage mechanisms are identified. A qualitative model of the plasma is described, in which two current conduction modes at the rail-plasma boundary are identified. These are an ohmic (direct contact) mode, and an arc-root mode. The severe rail-surface damage observed is thought to be due to boundary conduction in the ohmic mode rather than to the current-carrying arc-roots leaving and entering the rails.

Approved for Public Release

© Commonwealth of Australia

POSTAL ADDRESS: Director, Materials Research Laboratory
P.O. Box 58, Ascot Vale, Victoria 3082, Australia

CONTENTS

	<u>Page No.</u>
1. RAILGUN DEVELOPMENT AT MRL	1
2. EXPERIMENTS USING 500 mm LONG "RIPPER" RAILGUNS	3
2.1 Introduction	3
2.2 Objectives	4
2.3 Equipment and Operation	4
2.4 Summary of Experiments	11
3. POWDER-GUN INJECTOR AND PROJECTILE DEVELOPMENT	15
3.1 Introduction	15
3.2 Ramjet Cartridge Injector	15
3.3 7.62 mm Cartridge Injector	18
3.4 Projectile Development	21
4. RESULTS, ANALYSIS AND INTERPRETATION	22
4.1 Streak Photographs	22
4.1.1 Velocities and Propulsive Forces	28
4.1.2 Development of the Plasma	29
4.1.3 Aluminium Versus Copper Foils	31
4.2 Currents and Voltages	32
4.2.1 Discussion of Experimental Records and Energy Distribution	32
4.2.2 Estimate of L' from In-Bore Data	47
4.3 Magnetic Pick-Up Coils	50
4.3.1 Need for Calculated Waveforms	50
4.3.2 Interpretations of Waveforms Obtained	50
4.4 Rail Damage	61
4.4.1 Armature Dissipation	61
4.4.2 The Plasma Initiating Foil	70
4.4.3 I^2R Contribution (Joule Heating)	72
4.4.4 Rail Material; the RIPAL Experiments	72
4.4.5 Rail Construction; the RIPLAM Experiment	79
4.4.6 Arc-Track Damage Evidence	82
4.4.7 Summary of Damage Data	91
4.5 Conjectural Model of the Developed Plasma	93



Dist	Special
A-1	

Codes
1/or

CONTENTS
(contd)

	<u>Page No.</u>
5. SUMMARY AND CONCLUSIONS	94
5.1 Summary and Discussion	94
5.2 Conclusions	96
6. ACKNOWLEDGEMENTS	97
7. REFERENCES	98-99
APPENDIX 1 <i>Tabulation of Data</i>	1-3
APPENDIX 2 <i>Calculated Magnetic Pick-up Coil Waveforms</i>	1-12

EXPERIMENTS WITH A SMALL INJECTED RAILGUN

1. RAILGUN DEVELOPMENT AT MRL

Early in the MRL railgun program it was generally thought by railgun researchers that experimental railguns utilizing plasma-arcs would attain velocities of about 10 km/s. Barrel strength was a prime consideration in the attainment of such velocities from railguns and led to the constructions shown in Fig. 1 [1] for barrels about 1 m long. The rails were held in place by four ceramic pieces arranged to form a box section, around which an epoxy-kevlar composite was wound.

The early MRL experiments independently showed that velocities of 10 km/s would not be readily achievable and there was need for much more knowledge of the in-bore processes during the acceleration. Optical fibres were inserted as sensors into the rails to examine in-bore effects, but with limited success [2]. Damage to the fibre ends, for example, was a problem. Another problem was that rail damage was so severe that only one shot could be obtained from a pair of rails. It was difficult to remove and replace the rails using the barrel constructions shown in Fig. 1. Liquid nitrogen was used to shrink the rails to make this possible.

The above factors led to the construction of railguns with bodies consisting of two halves bolted together, enabling rails to be replaced quickly and making it easy to insert optical and magnetic probes wherever and whenever desired. The desire to study the plasma during acceleration led to the suggestion that clear plastic be used for the bodies. Perspex was tried, but cracked badly at the corners of the bore. Clear polycarbonate was tried next, together with rails which had rounded corners. These bodies (Fig. 2) were very successful. They could be used many times before any cracks developed. The clear bodies enabled the plasma to be photographed by streak and framing cameras and yielded, with directness and certainty, information that would be very difficult to obtain by other methods.

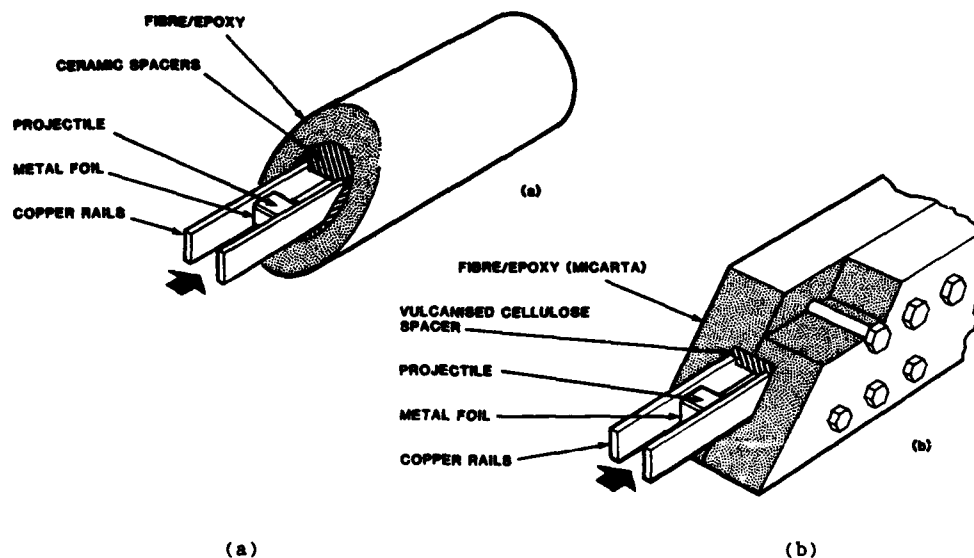


FIGURE 1 Railguns using (a) ceramic spacers and fibre glass wound barrels and (b) fibre/epoxy clamped barrels.

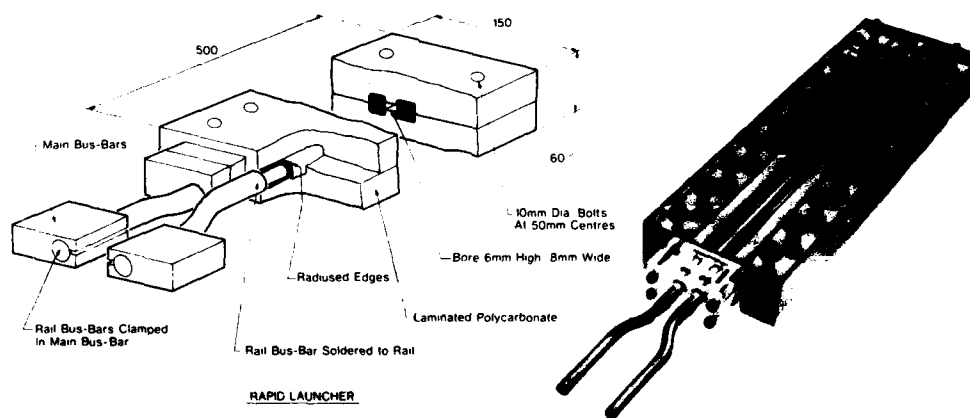


FIGURE 2 Railguns using clear polycarbonate bodies

The railguns using clear bodies were designated 'Rapid' and 'Ripper'. The Rapid guns used 12.5 mm x 12.5 mm rails, had a 6 mm x 8 mm bore and were 500 mm long. The square rails enabled four firings to be obtained from 'new' rails by rotating the rails. Some results from a series of Rapid firings have been reported previously [1,2,3].

The Ripper guns used 16 mm x 5 mm rails, a more likely geometry for actual railguns, and a larger, square bore, 10 mm x 10 mm, which is a more likely cross-section. A powder-gun injector stage was also added to the Ripper bodies to reduce plasma-initiation rail damage by giving the projectile a velocity of about 1 km/s before it entered the railgun. Two versions of Ripper guns were constructed. One version was 500 mm long and was used for the experiments described in this report and in Reference 8. The other version was 2.4 m long and was used in experiments to connect a second-stage electrical power source to the gun by 'puff-switching' [4].

The work reported here covered the period November 1984 to November 1985, and formed part of the MRL railgun program which commenced in 1979 and finished in June 1986. The final phase of the program is reported in Reference 4.

2. EXPERIMENTS USING 500 mm LONG 'RIPPER' RAILGUNS

2.1 Introduction

As was indicated above, three important aspects of railgun investigations are the rail damage mechanisms, the details of how the plasma-arc is established, and how the plasma carries current from one rail to the other.

Rail damage is particularly severe when a projectile is accelerated from zero velocity [5]. The surface metal in the starting region melts because of the heat from the plasma-arc and resolidifies into lumps and ridges. The damage is so severe that the use of the rails for a second shot is generally not possible. If however the projectile enters the railgun at about 1 km/s, the breech region of the rails is exposed to the arc for a much shorter time and reduced thermal damage is expected. At a sufficiently high injection velocity, the residual damage should be of a different kind, more related to the current flow between the rails and the plasma. Injection, however, requires different and more complex means of electrical switching and of causing plasma arc initiation than the simple methods that work well for railguns using static starts.

While logically a reduction in the plasma dwell time by injection was expected to reduce damage, an understanding of the process of establishing the plasma would be required to make a significant impact on early-damage reduction. This subject is dealt with in some detail in the report.

Study of the developed plasma, on the other hand, is intrinsic to obtaining a better understanding of the propulsion mechanism. In simple terms, if the plasma was an ideal sliding conductor it would have zero electrical resistance and zero drag and would transmit to the projectile a force, F , which is closely estimated by:

$$F = \frac{1}{2} L' I^2,$$

where L' is the high frequency inductance per unit length of the rails, and I is the rail current. In practice, however, neither the zero resistance condition nor total force value is obtained. This is evidenced by the failure of existing theoretical models to accurately predict railgun performance.

Apart from the standard current and muzzle voltage measurements, as many means of probing the plasma as possible are desirable to investigate its mechanisms. Spectroscopy is one such means, and gives valuable information concerning plasma temperature, composition and degree of ionization [6]. Streak photography, together with time and position markers that enable data from other sources such as magnetic pick-up coils to be accurately correlated with the photographic detail, is another means. Both techniques were used for the experiments discussed in this report. In addition, interpretations regarding the plasma model have been made from rail damage observations.

2.2 Objectives

The objectives of the investigations reported here were:

- (i) To obtain and study examples of rail damage free of the gross damage caused by stationary starts;
- (ii) To obtain and study information pertaining to the plasma arc, in particular breech and muzzle voltages, currents, magnetic pick-up coil waveforms and streak photographs;
- (iii) To develop a compact and simple injector as an important aid in the above investigations.

2.3 Equipment and Operation

A 500 mm long Ripper railgun with a powder-gun injector (Fig. 3) was used. Fig. 4 shows one of the experimental arrangements. The rail material was a copper - 0.6% cadmium alloy approximating B52873:C108. The alloy had been selected for earlier experiments on the basis of greater strength and wear resistance than high-conductivity copper. Conductivity of the alloy is 80 to 95% that of pure copper. The rails (16 mm x 5 mm cross-section) were rubbed to a smooth finish on the bore sides with 800 grade and finer emery paper to remove surface burrs and nicks. The two-piece clear laminated polycarbonate body was clamped between a base plate and two upper plates using 12 mm diameter coarse thread, medium-tensile-strength bolts at 25 mm intervals. The bolts were tightened with an air wrench to 80 Nm torque. Fig. 3 shows a section through the railgun.

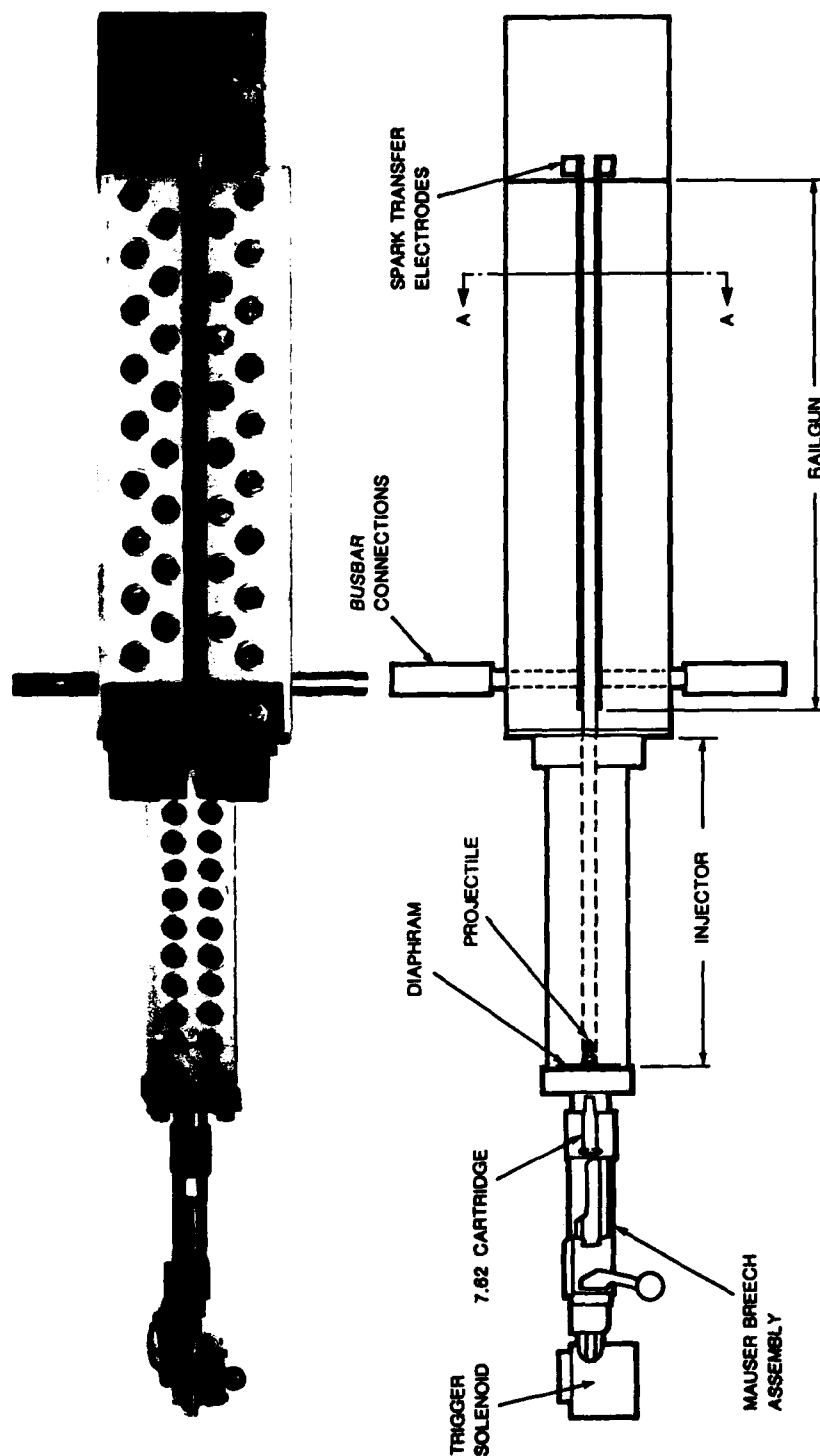


FIGURE 3 (a) 500 mm Ripper railgun with powder-gun injector attached.

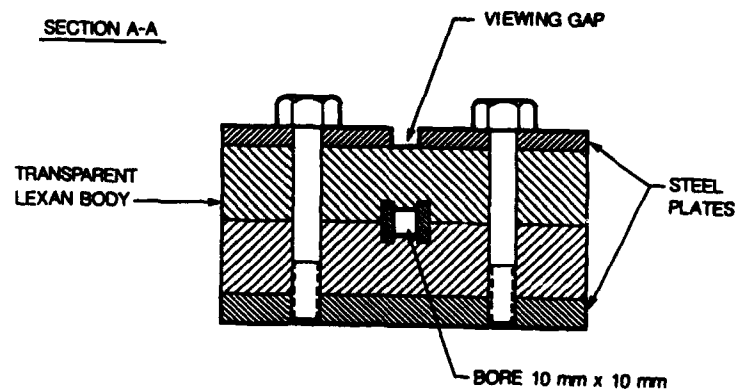


FIGURE 3 (Contd) (b) Section A-A through Ripper gun-body.



FIGURE 4 Experimental arrangement used during development of injector.

The capacitor bank and a $6.3 \mu\text{H}$ inductor were used for the power source. The capacitor bank was discharged into the inductor via a main switch and the railgun (Fig. 5). At peak current the capacitor bank was crowbarred by a spark-gap which was triggered by diodes and an exploding fuse-wire [7].

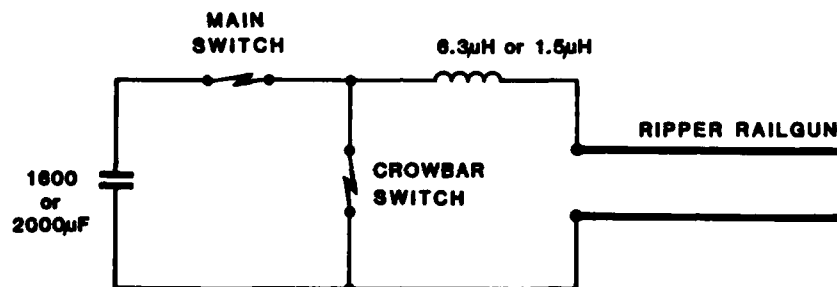


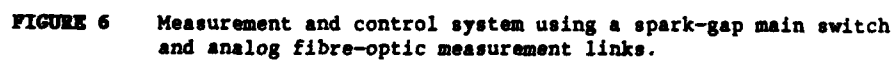
FIGURE 5 Power source for Ripper firings

Two sizes of capacitor bank were used. In the first experiments the bank consisted of eight $200 \mu\text{F}$ Maxwell type 3378 10 kV capacitors in parallel (Fig. 4). For these experiments a spark-gap was used as the main switch to connect the capacitor bank to the inductor and railgun circuit. The spark-gap was triggered by a spark introduced into the gap upon detection of the arrival of the projectile at the end of the powder-gun.

For the later experiments the capacitors were assembled into racks containing 5 units in parallel and an ignitron was used for the main switch instead of the spark-gap. Two racks of capacitors i.e $2000 \mu\text{F}$ were used. The diode-triggered spark-gap was still used to crowbar the capacitors.

The measurement and control system used in the experiments is shown in Fig. 6.

Current supplied to the railgun was measured with a Rogowski belt placed around one of the inductor busbars and connected to a simple low-pass RC filter with a time-constant of 15 ms. Voltages were generally measured with the aid of 1000:1 high impedance dividers, but in later experiments some measurements of the muzzle voltage were made using a current transformer to monitor the current through a shunt resistor across the muzzle.



Injection velocity was estimated firstly by measuring the time interval between the arrival of the flash of the powder gun at two points. This was done with two fibre optic probes - one placed 20 mm in front of, and the other 20 mm behind the interface between the injector and the railgun. Secondly, the above velocity was compared with that deduced from the position of the earliest arc-damage on the rails and the known delay from injection flash to the main-switch trigger.

Exit velocity was measured principally by recording the time interval between the projectile breaking a 0.5 mm diameter pencil-lead (break-wire) mounted 150-200 mm beyond the railgun muzzle and the projectile passing through a printed foil (grid on copper-clad polyester) break-screen. This was mounted on the front of the projectile catch tank which was placed 0.5 m to 1 m down-range. A muzzle flash detecting probe was used to complement the pencil-lead break and to provide evidence on effectiveness of obturation. The probe consisted of a 1 mm optical fibre inserted in a 1 mm diameter stainless steel tube mounted flush with the muzzle face. The steel tube provided protection and restricted the probe's field of view.

Magnetic pick-up coils as shown in Fig. 7(a) were used in all experiments. Groups of smaller coils were used in some experiments. Coils were oriented to respond to the plasma flux and not the rail flux i.e. the coil axis was directed along the railgun barrel. The multiple coils were used to study dynamic activity within the plasma. The results are reported elsewhere [8]. Coil locations are shown in Fig. 7(b).

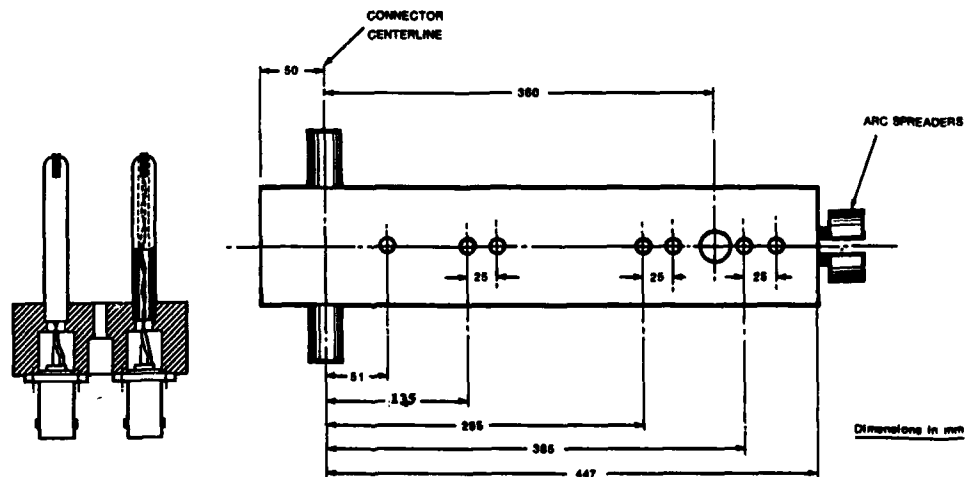


FIGURE 7 Magnetic pick-up coils and locations covering all reported shots. The larger hole was for arc-root investigations. Coils consist of 10 turns upon 5 mm former. Centre of coil was 7.5 mm beneath the bottom of the bore (12.5 mm below centre of bore).

A streak camera (Hycam) was used to photograph the plasma arc as it travelled along the railgun. A mirror mounted above the railgun (Fig. 4) transmitted an overhead view to the camera. A set of position marker bars was generally laid along the railgun to provide a distance calibration for the streak photograph.

The control signal network and the equipment and operating times are shown in Fig. 8. When the fire button was pressed the streak camera was started and a delayed pulse generator was triggered. A period of 700 ms was allowed for the film to come up to speed, at which time the delayed-pulse generator sent a pulse to release the trigger of the powder-gun injector. The cartridge then fired, driving the projectile down the barrel. As the projectile passed the first of the fibre optic probes in the injector muzzle, the flash from the burning gases generated a signal which was used to trigger a second delayed pulse generator. After 35 μ s this generator sent a pulse to the spark generator circuit which, after a further 20 μ s, produced the spark to close the main switch.

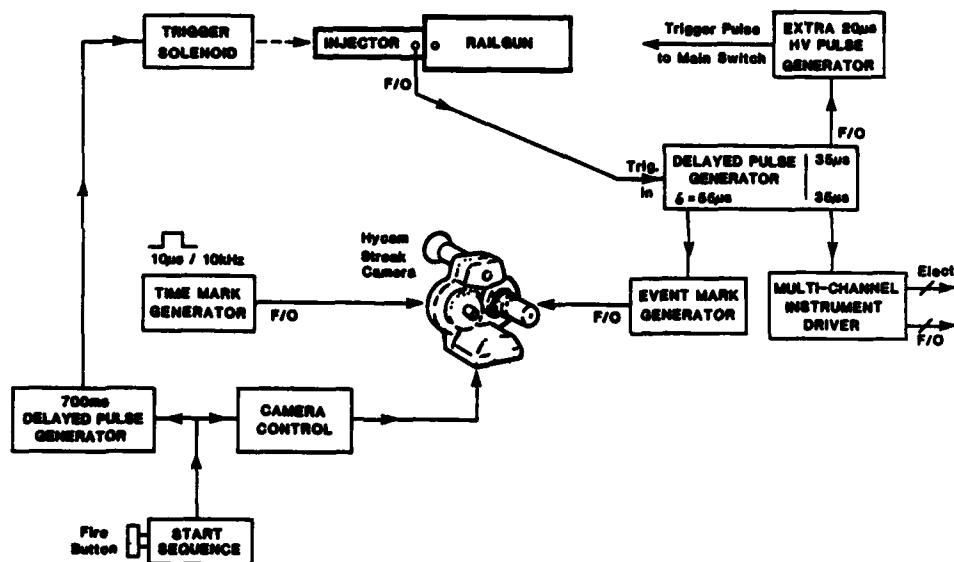


FIGURE 8 Control signal network

A second output from the latter delayed pulse generator was used to start the transient recorders, which were set to retain either 256 or 512 samples of pre-trigger record depending on the sampling rate. A marker pulse,

10 μ s wide, was coupled in synchronism with the recorder triggering into all recorders capable of the necessary circuit modification. The marker pulse on these records thus appears approximately 20 μ s before main switch initiation.

The firing of the gun consists of several high power electrical discharges which are electrically very noisy and much effort was required to reduce the effects of electrical noise on both control and recording equipment. The open-air main arc-switch was particularly troublesome and it was prone to disrupt data recording equipment at the instant it was triggered. One type of recorder, the Datalab DL910, was particularly susceptible, and would sometimes be 'paralysed' for several seconds by the main switch.

Noise effects were minimized by using a battery and inverter to power some instruments, by using isolation transformers for others and by earthing equipment clusters at one point only. As much as possible, inter-equipment electrical connections were avoided. Extensive use was made of fibre-optics in triggering circuitry. It was also found that noise was reduced by terminating the railgun muzzle with a resistor of about 100 Ω , which corresponds roughly with the railgun characteristic impedance when it is viewed as an electrical transmission line.

2.4 Summary of Experiments

Following the development of a suitable powder-gun injector, five experimental programs were carried out using 500 mm long Ripper railguns. Rails from each of the five programs are shown in Fig. 9. The data from the 12 most successful shots are used in this Report.

The features of the five programs are as follows:

- (i) Aluminium initiating foils and a 6.3 μ H storage inductance were used for the firings designated RIP 301 to RIP 306.
- (ii) Aluminium foils and a 1.5 μ H storage inductance were used for the firings designated RIP 307 to RIP 311.
- (iii) A matrix of 9 small magnetic pick-up coils was inserted as close to the bore as possible (Fig. 7) to detect individual arcs within the plasma. These firings were designated SUBAC 1 to SUBAC 4.
- (iv) Aluminium strips were keyed into rail surfaces to study the transport of material both across and along the bore for the firings designated RIPAL 1 and RIPAL 2.
- (v) Three channels were machined lengthwise in the rail faces and filled with an epoxy (heavily loaded with silica) for the single experiment designated RIPLAM.



ABOVE: From the top—RIP310, RIP306, RIP307.
RIP306 was an 82 kA firing

SUBAC4 RAILS



SUBAC3 RAILS

FIGURE 9 Rails from RIP and SUBAC firings shown folded out.
Rail polarity is marked at the muzzle end

RIPAL2 RAILS



RIPAL1 RAILS

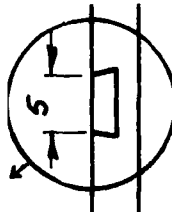


FIGURE 9 continued
 Rails from RIPAL and RIPALM firings
 Rail polarity is marked at the muzzle end
 Holes were drilled in rails after firings

The 1600 μF capacitor bank and the spark-gap main switch were used for programs (i) and (ii). For programs (iii) and (v) copper initiating foils were used, the capacitor bank was 2000 μF and the ignitron was used as the main switch in place of the spark-gap. The storage inductor was 6.3 μH .

Except for SUBAC 3, all firings were made with the capacitor bank charged to 6 kV. The voltage in the case of SUBAC 3 was 5 kV.

The storage inductance was reduced from 6.3 μH to 1.5 μH in (ii) because with the higher value of inductance the injection velocity of about 1400 m/s caused the projectile to travel too far in the railgun (about 250 mm) before the current reached its peak value. This left only about 200 mm for the inductive drive phase. The region of stable plasma and well defined electric propulsion was thus very short. By reducing the inductance (shorting-out turns on the 6.3 μH inductor), the time to peak current was reduced and the period of inductive drive was increased. Despite this advantage, the 6.3 μH system was reinstated for subsequent experiments, in order to retain some point of reference for rail damage investigations.

The change to copper initiating foils in programs (iii) and (v) was not dictated by the requirements of the experiments, but by practical reasons associated with reliable plasma initiation. Aspects of reliability and foil selection are further discussed in Section 3.

The special purpose of the SUBAC series was to obtain evidence for the plasma-arc model proposed by Marshall [9]. According to this model, the plasma is connected to the rails via numerous "sub-arcs" which move along the interface between the rails and the bulk plasma. The RIPAL and RIPLAM experiments also contained groups of pick-up coils to test this model. This aspect of the experiments is reported elsewhere [8].

The RIPLAM experiment was designed to test the idea, developed by MRL workers, that if the major current conduction from the rails to the plasma occurred on arc spots or arc tracks, then not all the rail surface was needed. The use of insulated channels embedded in the rail surface, therefore, might restrict the current to a lesser, but adequate, area of copper without increase in rail damage. The hard insulated channels would suffer less damage, enabling the rails to be re-used by providing a smooth projectile riding surface. It was recognized that obturation problems could arise in subsequent shots using the same rails, as a result of differences in wear rates of the copper and insulating strips.

3. POWDER GUN INJECTOR AND PROJECTILE DEVELOPMENT

3.1 Introduction

The addition of a powder-gun injector to the Ripper railgun required solutions to a number of problems which only became evident as experimentation proceeded.

For example, initiation of the plasma armature was a problem. Aluminium foils placed directly across the rear end of the cuboid projectiles, as previously used in stationary-start railguns, were damaged by the powder blast. Initially it was thought that the hot, brightly glowing gases from the powder-gun might be conductive enough to break down and form a plasma armature when they entered the railgun behind the projectile. This would have eliminated the need for a foil behind the projectile and, possibly, also the need for a main switch. Early experiments showed, as had been inferred from a study by Chung [10], that the powder-gun gases were not conductive enough and would have required seeding.

Another problem was due to the low mass of the projectiles (0.5 g - 1 g). It was found that such low mass projectiles caused insufficient confinement, and hence inadequate pressure, for the powder to burn properly.

3.2 Ramset Cartridge Injector

The first powder-gun injector used Ramset cartridges (0.22 inch calibre). This gun was easily and quickly constructed and the Ramset cartridges were readily available in a range of strengths. Fig. 10 shows this injector. Fig. 11 shows a firing of the injector and railgun. The glow in the injector body due to the burning powder should be noted. As stated above, it was thought that the glow might indicate that the gases would be sufficiently conductive to break down and form a plasma armature.



FIGURE 10 Ramset injector. Projectiles were placed about 20 mm inside the plastic body and the Ramset cartridge was held in the steel breech block.



FIGURE 11 Firing of Ripper railgun with Ramset injector attached. Injection velocity for this firing was 400 m/s.

The injector was first tested on its own, i.e. not connected to the railgun. The various projectiles in use at that time (Fig. 12) were fired from it and their exit velocities were measured. Some of the results are given in Table 1.

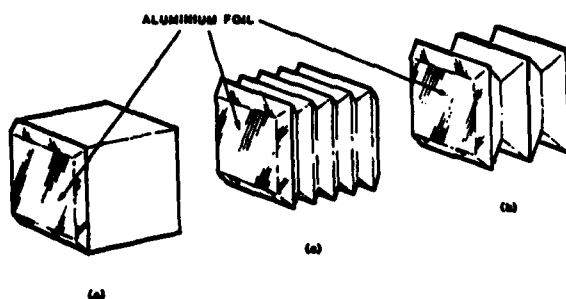


FIGURE 12 Projectile shapes initially used. Material was red-fibre or polycarbonate. Foil glued to rear of projectile.

TABLE 1

Projectile C velocities obtained with Ramset cartridges

Cartridge Colour	Strength	Velocity (m/s)
Brown	Minimum	238
Green	Weak	289
Yellow	Medium	231
Red	Strong	367
Violet	Very Strong	400
White	Especially Strong	405
White	Especially Strong	419

As it was desired to obtain the highest possible injection velocity, white cartridges were used for further injector experiments.

At this stage a problem due to burning rate and projectile mass was becoming evident. Unburned powder was sometimes found scattered around the injector muzzle. This was at first thought to be evidence of poor obturation by the projectile.

A series of firings with the Ramset injector attached to the railgun was then carried out. As indicated earlier, one result of these tests was that the burning gases were found to be insufficiently conductive to break

down and form a plasma-arc (with 6 kV applied to the rails). An initiating foil was therefore still required at the back of the projectile. However when projectiles with aluminium foils were used the breakdown was unreliable. Recovered projectiles were found to have incompletely vapourized portions of the foils still attached to them. This suggested that the foils had not properly contacted the rails when the projectiles entered the railgun. It was also evident that the spark-gap main-switch was unreliable when used in conjunction with the poorly contacting foils. This led to the replacement of the spark-gap switch by the ignitron.

The projectiles used up to this time were cuboid types (Type (a)) developed for stationary-start railguns (Fig. 12). Red-fibre projectiles were unsatisfactory in the injector application because they broke into several pieces. To improve obturation, particularly in the injector-to-rail transfer region, Marshall devised the 'nested pyramidal shells' construction (Figs. 13,15). The pyramids were moulded from various materials including polycarbonate (which has high impact strength), polypropylene, and polyethylene (which is relatively soft). Combinations of pyramidal shells made of these materials together with the effect of the concave rear shape were expected to result in good strength and obturation properties. However, polypropylene shells proved to be too brittle, particularly those pressed with high levels of talcum or carbon loading. It was expected that good obturation would occur because the gas pressure would force the rim into firm contact with the bore walls. Another useful feature of the design was that projectile mass could be easily adjusted by varying the number of pyramids.

3.3 7.62 mm Cartridge Injector

To prepare for the possibility that an injection velocity of 400 m/s would not be high enough to significantly reduce rail damage, steps were taken to develop an injector based upon a 7.62 mm Mauser rifle and a steel body (Fig. 3).

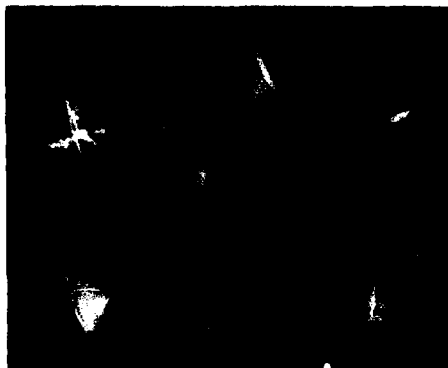


FIGURE 13 'Nested-pyramids' projectiles and pyramids.

This size was chosen because of the availability of a rifle, primed cartridge cases and various powders. Experiments to find a suitable charge were then undertaken.

Initial tests were undertaken with a sawn-off rifle firing cartridges sealed with dummy cylindrical plastic projectiles having similar masses to the railgun projectiles (0.2 to 0.5 g). These showed that powder No. AR4001 ('T'-powder) was the most suitable. T-powder is a high bulk, fast burning propellant. Velocities in the region of 1100 m/s were obtained using 0.7 g of powder.

Initial firings of the injector, however, were not satisfactory. Velocities were inconsistent, misfires occurred, and much of the powder was unburned as was shown by 'peppering' of the velocity break-screens. The cartridges had been loaded with 1 g of T-powder and then crimped at the ends.

The cause of this poor performance was thought to be insufficient chamber pressure in the injector due to the poor confinement offered by the low mass of the projectile. To test this theory, diaphragms were placed between the steel body and the rifle breech, thereby containing the charge in a smaller volume and enabling proper burning to occur before the bursting of the diaphragm. Various materials were tried, including Mylar sheet, 18 SWG aluminium and different thicknesses of steel shims. Only the thicker steel shims (0.25 mm and thicker) gave any significant improvement.

Following a series of tests using the newly developed nested pyramid projectiles, three factors were found to be necessary for consistently successful results from burst diaphragms:

- (i) steel shim 0.5 mm thick,
- (ii) the shim to be scored diagonally (with a scribe),
- (iii) the breech end of the injector bore to be rounded (3 mm radius).

The last factor ensures that the diaphragm segments do not break off and damage the foil, projectile, or bore. Fig. 14 shows a diaphragm before and after use, and injector detail in that region.

It was found unnecessary to vent the powder-gun gases to prevent them entering the railgun and continuing to accelerate the projectile. Such acceleration, if it occurred, would be useful in a practical gun but would have confused the study of electrical acceleration effects in an experimental gun. Had venting been necessary it would have added to the injector complexity, and created a hazard for the integrity of the projectile during passage past any venting arrangement. A streak photograph taken of a powder-only shot with the railgun attached showed negligible velocity increase in the railgun barrel. The decision not to provide venting was further justified in a later powder-only experiment using a 2.4 m long railgun [4]. In this experiment magnetic strips were inserted into the projectile and its velocity was determined by pick-up coil outputs. The velocity remained at 1212 m/s for the first 600 mm and then gradually diminished to 794 m/s at exit.

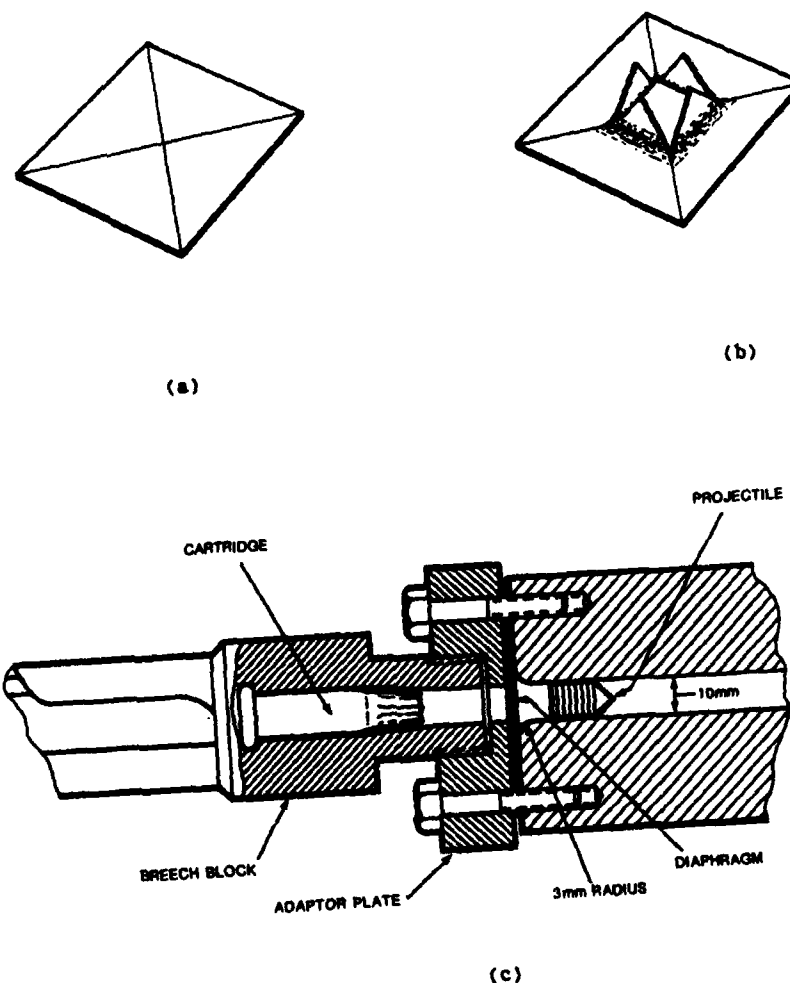


FIGURE 14 Burst diaphragms (a) prior to use. Note the diagonal scoring. (b) After use. Note the 'banana-peeling' of the sectors due to the scribing and to the rounding of the breech-end of the injector bore (c).

3.4 Projectile Development

Test firings with the injector attached to a railgun showed that the pyramidal projectiles provided excellent obturation. However, the aluminium foil placed in the cavity at the rear was still damaged by the powder blast. An extra pyramid was placed behind the foil to protect it. Contact between the foil and the rails was still unreliable and examination of a recovered projectile showed that the foil still suffered blast and heat damage from the powder. To overcome this, the pyramid behind the foil was cut down by about 0.1 mm and a second full height pyramid was placed behind it to shield the foil edges from the heat of the burning powder. Mis-fires still occurred when simple aluminium foils were used.

The final improvement was to use copper-clad polyester film for the foil, with the polyester facing the rear. This projectile design is shown in Fig. 15. Folding the foil into the gap formed by the cut down pyramid provided an extended foil-bore contact area, while the natural spring of the polyester backing ensured that there was contact with the rails.

The pyramids were sometimes, but not always, held together with a small amount of adhesive (e.g. silicone rubber). Sometimes, when no cement was used, the pyramids separated in flight outside the railgun muzzle. It should be noted that only the portion of the projectile ahead of the foil is accelerated by the railgun. The two rear pyramids separate from the forward ones when the copper is vapourized and do not experience electrical propulsion. They appeared to have no influence on gun performance or rail damage.

With the above 7.62 mm cartridge injector and projectiles, injection velocities between 1300 and 1400 m/s were reliably obtained for 0.8 g projectiles. Together with the use of the ignitron for the main switch, the uncertainty of firing, which was much more significant for injected shots than for stationary projectile shots, was overcome.

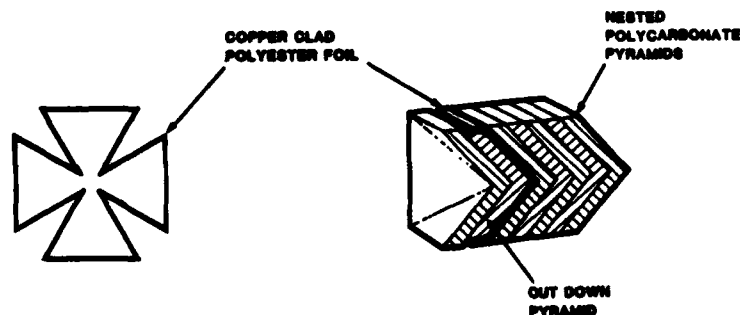


FIGURE 15 Final projectile design. (Polyethylene pyramids were sometimes used in the fifth and seventh positions)

4. RESULTS, ANALYSIS AND INTERPRETATION

4.1 Streak Photographs

Streak photography provides a position-versus-time record of the plasma [2]. The vertical axis (the short axis) of the photographs corresponds to displacement from the breech end of the railgun and the horizontal axis corresponds to time. Distance calibration is obtainable from markers on the railgun body. A slight parallax error (1%) is introduced by the unavoidable spacing between bore-top and distance marker bars. The length of film occupied by the event is determined by film speed past the camera slit, and so the time-scaling on the photographic record can vary from firing to firing.

Eight examples of streak photographs are given in Fig. 16 from six of the firings described in Section 2.4. Three of the figures are of prints from reverse-developed films. This has no experimental significance. Displacement markers can readily be seen as horizontal lines across the streak in Figs 16(d) to (h).

Three types of information are available from the streak records. Firstly, the velocity of the leading and trailing edges of the plasma can be determined from their slopes using the relationship:

$$v = \frac{A}{B} \tan \alpha,$$

where A and B are the distance and time calibration factors and α is the slope angle physically measured. If the leading edge is sharp it can be assumed that the plasma is against the rear surface of the projectile and that the leading edge velocity is also the projectile velocity. Accuracy is estimated at ± 50 m/s for absolute velocity measurement, and ± 15 m/s for relative measurements.

Secondly, the 'length' of the plasma can be found from the vertical distance through the streak. The lengths so obtained, however, need to be interpreted with care because they are affected by the film and print exposures. It was found that good exposures for the 80 kA current-peak firings were obtained using an ND2 filter at f22 with a camera slit width of 0.1 mm. This exposure recorded the higher range of intensities from the plasma arc but suppressed lower effects such as the glow of the gases which filled the barrel behind the plasma arc. Over-exposure on printing further defines the hottest and, presumably, the current-carrying portion of the plasma. Such prints were used for the measurement of plasma length.

Thirdly, the physical development of the plasma and some of the activity within it can be deduced, particularly when information from the streak photograph is considered in conjunction with pick-up coil and rail damage information.

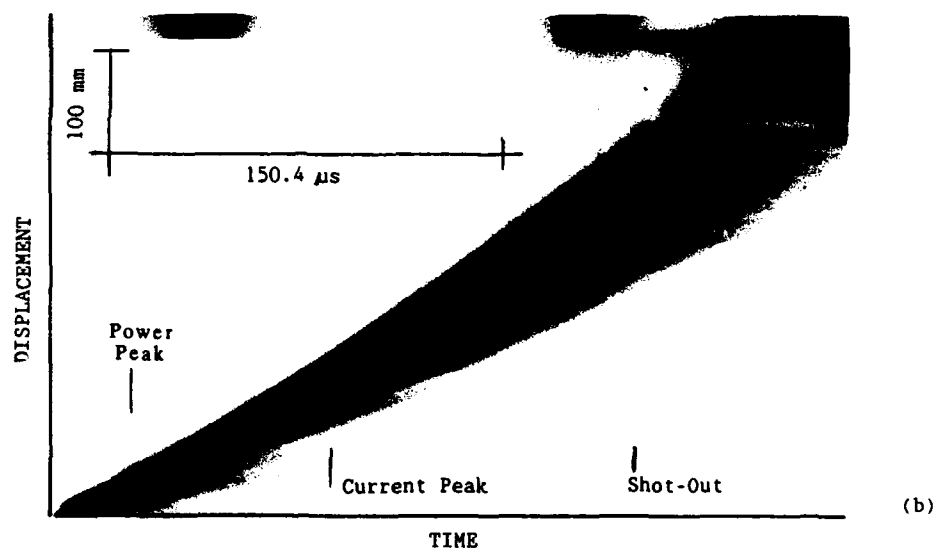
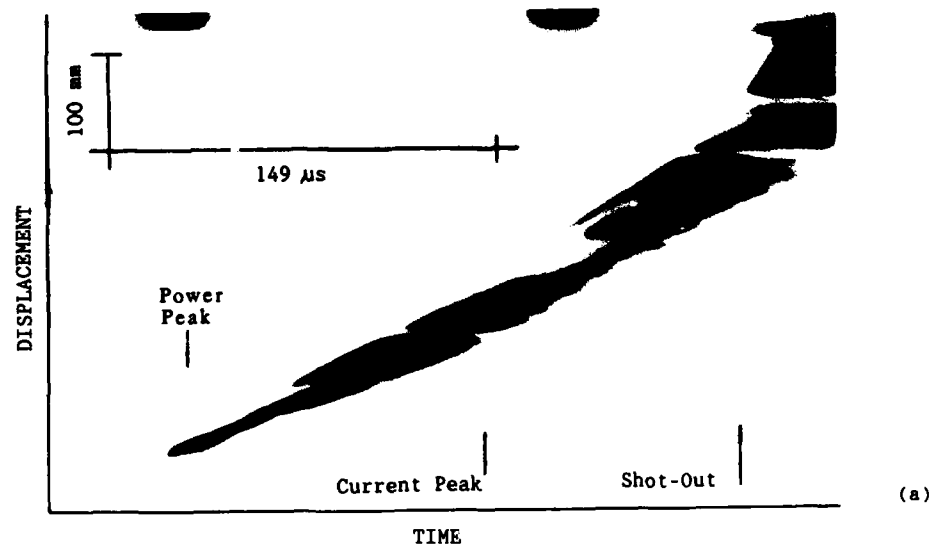
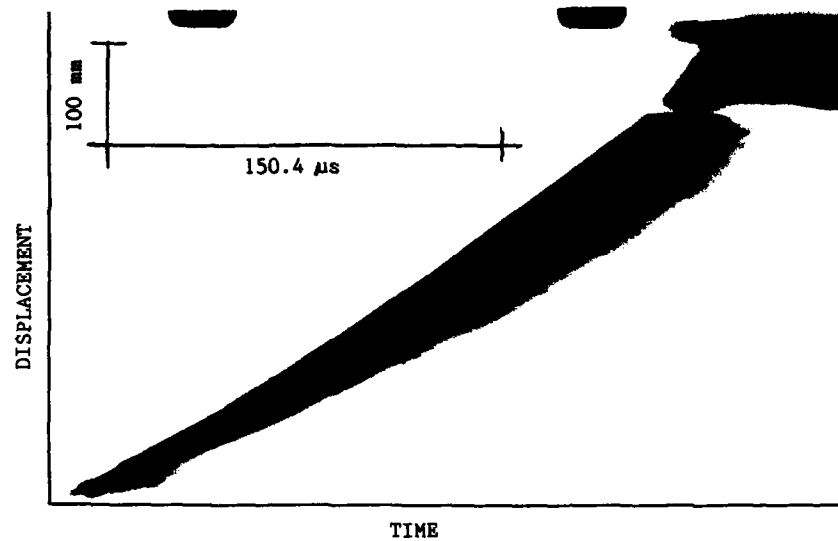
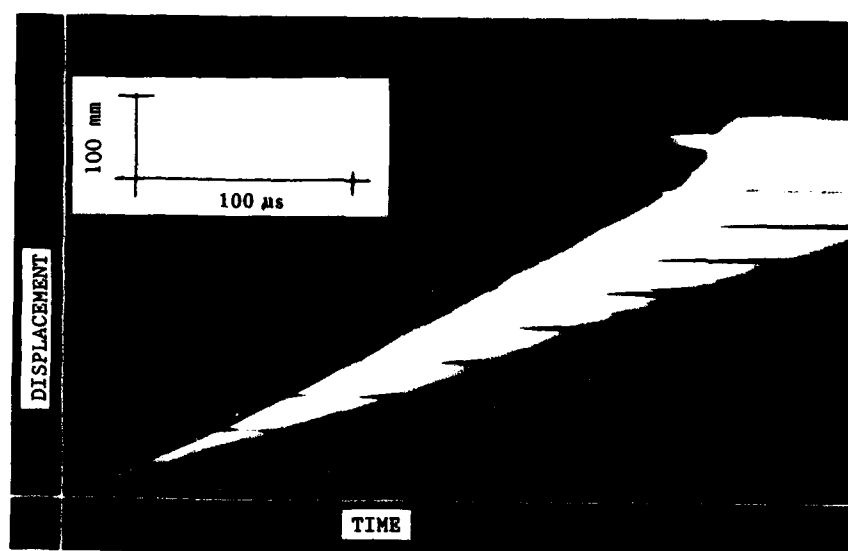


FIGURE 16 Streak photographs from Ripper railgun firings

Top: Firing RIP 305; film underexposed
 Bottom: Firing RIP 310; Streak processed to expose more low-intensity information



(c)



(d)

FIGURE 16 (Contd) Streak photographs from Ripper railgun firings

Top: RIP310; lower intensities suppressed
 Bottom: SUBAC 2; film overexposed

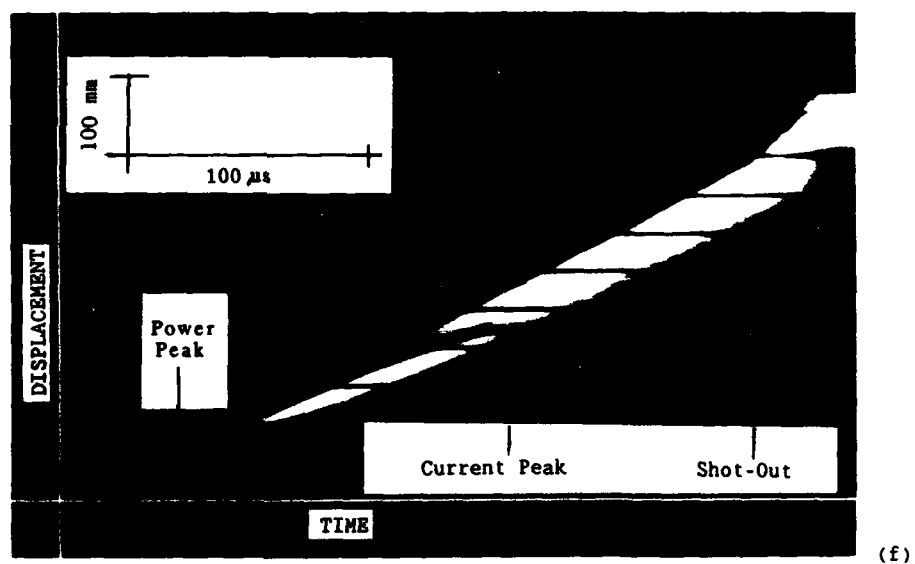
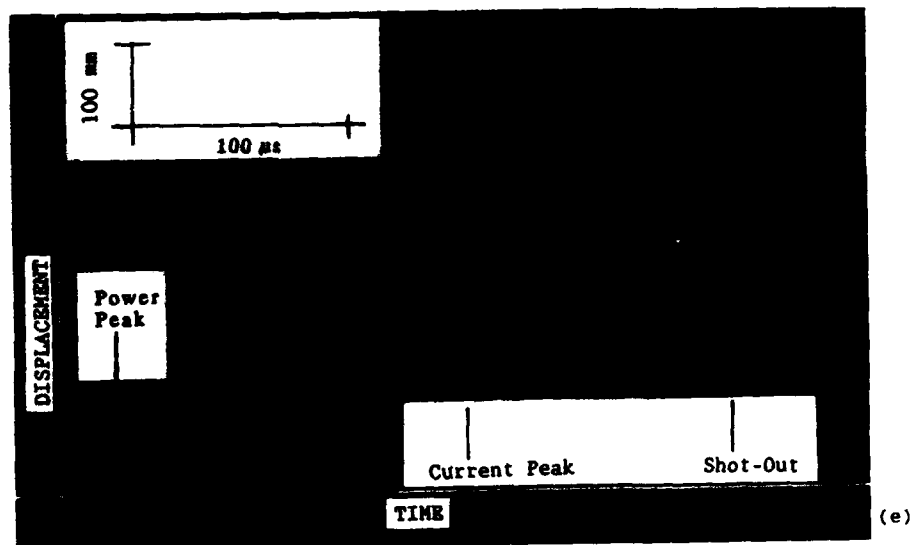
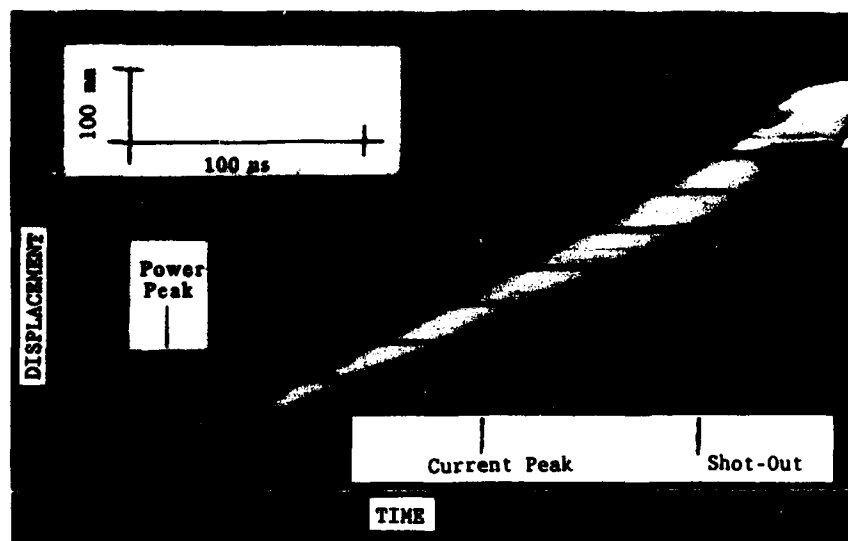


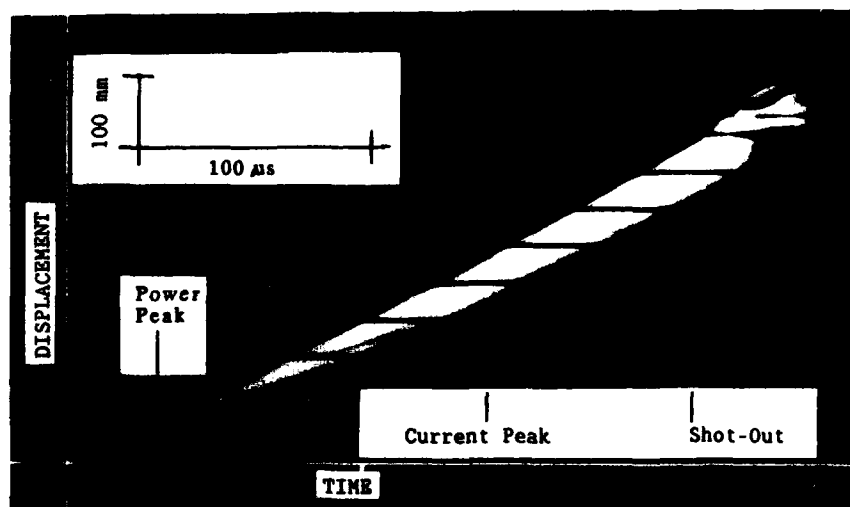
FIGURE 16 (contd) Streak photographs from Ripper railgun firings

Top: SUBAC 2; overexposure limits background suppression

Bottom: SUBAC 4



(g)



(h)

FIGURE 16 (contd) Streak photographs from Ripper railgun firings

Top: RIPAL 1; marred film
Bottom: RIPAL 2

From the records in Fig. 16, the following specific points should be noted:-

(i) The underexposed RIP 305 streak shows contrasting patches angling across the print. Such patches are discussed in some detail in Sections 4.3.2. and 4.4.7.

(ii) The RIP 310 (130 kA current peak) streak record has two interesting features. The first feature is the series of bumps on the leading-edge of the streak, just after electric shot-start. It suggests that the projectile has experienced two jolts, has been slowed down again each time, and finally has been pushed steadily until reaching a constant velocity second phase, which persists for a significant proportion of the barrel length. This phase also appears to commence with a small velocity step, suggesting perhaps a sudden reduction in projectile drag. This is a possibility with the pyramid style of projectile construction if the stack of shells relaxes after a high pressure phase. Hot material can be seen following along slowly behind the intense, current-carrying portion of the plasma in both Figs 16(b) and (d). The print exposure of Fig. 16(c) better defines the hot plasma core, and shows more detail in the plasma initiation phase.

(iii) The RIPAL 1 streak shows a negative marred by electrostatic discharges. The discharges had sufficient luminous energy to expose the film. This effect is repeated over the entire film length. All discharges have originated from sprocket holes. Both the camera and film processor were examined and discounted as likely causes. This implies that the film was defective as supplied, the discharges presumably having occurred during spooling at some late stage of manufacture.

The projectile trajectory in the first 150 mm is probably not given by the visible edge of the plasma streak. It is more likely that some obscuration has occurred. For this streak, and the following streaks, it is sensible to fit a smooth transition from the known ignition point of the foil and injection 'slope' to the streak-front sharp edge at approximately 130 mm depending on the streak.

(iv) The SUBAC 2 and 4 streaks are the result of films being exposed differently, the SUBAC 2 film being overexposed (during the shot). While overexposure enabled the background to be studied, 'hard' printing was required to reduce the background (Fig. 16(e)). In the process, the sprocket hole images (which normally can be used as a backup on timing markers) have disappeared, but the marker bars have emerged. The print of Fig. 16(e) is still not optimum for plasma length measurement.

(v) The SUBAC 4 streak shows an excellent example of a feature associated with all the streak records obtained from injection-assisted shots (specifically the 80 kA peak current shots), but which is visible to varying extents. This effect is considered in Section 4.3.2, and an explanation is proposed.

4.1.1 Velocities

Velocities obtained from the slopes of the leading edges of the RIPAL 1 and 2 streaks and the SUBAC 2 streak are given in Fig. 17. The differences between the experiments were that in the RIPAL experiments the rails contained the aluminium strips mentioned previously and the accelerated projectile masses were about 10% less (0.8 g compared to 0.88 g).

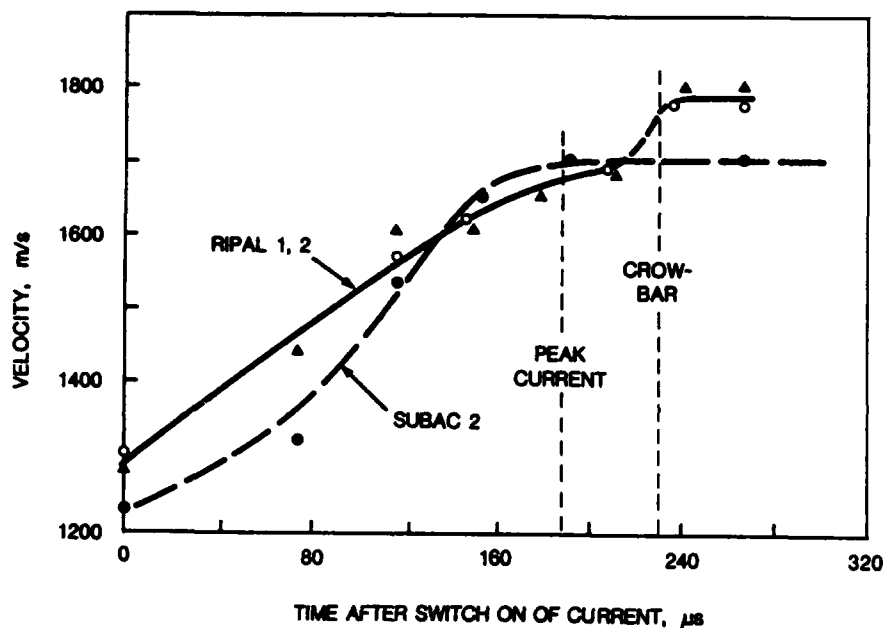


FIGURE 17 Velocity of leading edge of plasma for three firings, denoted RIPAL 1,2 and SUBAC 2

An important use of the in-bore velocity profile is to compare the actual velocity with that to be expected from the Lorentz forces. Velocities measured at exit are often in poor agreement with models which use data, such as friction, effective inductance and arc drops, extrapolated from different experiments. Sometimes the exit velocities are greater than can be explained by the possible variation of the above factors. Two factors which may be responsible for these discrepancies are the explosive-like formation of the plasma and the length of the railgun. If the railgun is short, the initiating foil explosion may contribute significantly to the exit velocity and mask the

effects of friction and a low value of L' . This effect has been noted elsewhere [11]. The following calculations show that a large additional force was present in the RIPAL firings.

The current in the railgun circuit rises sinusoidally as the capacitor energy is transferred to the inductor. If the current reaches a peak value, I_p , and the projectile force is $F = 1/2 L' I^2$, the velocity increment Δv , during the quarter cycle rise to peak current is:

$$\Delta v = \frac{L' I_p^2 T_{1/4}}{4M}$$

where L' is the high frequency inductance per unit length, $T_{1/4}$ is the quarter cycle time and M is essentially the projectile mass. For the Ripper geometry used in the RIPAL firings, from Kerrisk's equations the theoretical L' is $0.407 \mu\text{H/m}$. The peak current was 82 kA, the time to peak was $184 \mu\text{s}$ and the projectile mass was 0.8 g. The above expression yields:

$$\Delta v = 157 \text{ m/s}$$

The accuracy of this value is about $\pm 5\%$. Since the injection velocity was $1300 \pm 20 \text{ m/s}$ (App. 1), the above calculation predicts a velocity of $1457 \pm 28 \text{ m/s}$ at an instant $184 \mu\text{s}$ after the commencement of current flow. Figs 16 and 17 show that the actual velocity at this time was 1680 m/s , with an accuracy of $\pm 50 \text{ m/s}$. Therefore an increase of $380 \pm 50 \text{ m/s}$ over the injection velocity was obtained. In terms of energy increments, the theoretical increment would have been 120 J to 227 J whereas in fact the projectile gained 336 to 542 J. The same calculations performed on other shots confirmed the phenomenon of excess velocity. It is likely, therefore, that the effect was common to all shots.

An additional force, which was much greater than the Lorentz force, was evidently present. The explosively generated component of the gas pressure of the plasma, which exists while the plasma expands to its equilibrium length, is the obvious source of this force.

4.1.2 Development of the Plasma

The discussion in Section 4.1.1 of excess velocity leads to consideration of the development of the plasma.

The plasma is initiated by vapourization of the foil behind the projectile. Referring particularly to the copper foil shots, the streak photographs, Fig 16, show that the plasma develops over a period of about $150 \mu\text{s}$ after the turn-on of current. For 30 to $40 \mu\text{s}$ after current commences the plasma may not be visible. At about $50 \mu\text{s}$ it is just visible and has a length of a few mm. Thereafter it grows for about another $100 \mu\text{s}$ to a length of about 50 mm. The 'hot' portion of the plasma then either remains constant in length, or grows very slowly.

The above observations can be explained in terms of the energy needed to reach various physical states of the foil, the power supplied to the plasma and the attainment of equilibrium by the plasma. The development can be considered in four stages:

(i) The mass of the copper foil used in the RIPAL 2 experiment was about 38 mg. Based upon the data in the table below, the foil would be molten after absorbing 14 J and would be vapourized after absorbing 240 J. Using muzzle voltage and current records (Fig 19(h)), the energy supplied to the plasma can be plotted (Fig 18(a)). From this it is found that 14 J was supplied to the foil in the first few microseconds following current turn-on and that 240 J was supplied after about 35 μ s. The muzzle voltage reached peak voltage at this time. This is consistent with the completion of vapourization of the foil, since vapourization separates its atoms and raises its resistivity and consequently raises the voltage across it.

Energy Steps Associated with Ionizing Copper

Condition	Energy (J/mg)	
	Increment	Progressive Total
To heat to melting point	0.36	
Latent heat of fusion	0.2	0.56
To heat to boiling point	0.93	1.5
Latent heat of vapourization	4.8	6.3
To achieve first level ionization	11.6	17.9

(ii) From 35 μ s to 70 μ s the muzzle voltage (i.e. the plasma voltage drop) falls rapidly, which suggests the onset of ionization leading to arcing in the metallic vapour. This is consistent with the first strong appearance of the plasma on the streak photographs at about 50 μ s after current turn-on. (The initial vapourization of the copper foil, at a temperature of about 3000 K, is not always recorded. This is because the film exposure is primarily set to record the developed plasma, which has a temperature of at least 10,000 K). Note that, while the fall of muzzle voltage in this time frame is rapid, it is nevertheless progressive, i.e. the development of plasma is progressive. In fact, the energy necessary to achieve 100% first-level ionization (viz. 670 J) has not been supplied to the armature until about 66 μ s, which is close to the end of the phase being discussed. Furthermore, some of this energy will have been lost. In this phase the armature resistance is still controlled by the metal vapour. The conduction is therefore probably still diffuse in the body of the 'plasma' armature.

(iii) The electrical energy supplied after 70 μ s raises the temperature and pressure of the ionized vapour, which may now be termed a plasma, and it expands. Vapourization of the foil causes ohmic contact with the rails to be lost and the consequent arcing to the rails means that rail material enters

the plasma and contributes to its growth. As the plasma develops, its heat also causes material to enter from the polycarbonate walls.

The expansion of the plasma, due to the electrical energy input and the materials that enter it from the bore, generates force on the projectile in addition to the Lorentz force. Because of the superimposed Lorentz force the plasma as a whole moves toward the muzzle. At the rear (the lower edge on the streak photographs) of the plasma the thermally-induced pressure is opposite to the Lorentz force and so the particle velocity there will be lower than at the front. As the rear end falls behind the main body of the plasma it cools and its conductivity decreases, the current through it drops and the Lorentz forces decrease. This effect results in a spreading of the plasma. Condensation occurs onto the rails and sides of the bore. Figs 16(b) and (d) provide evidence of both the increase in plasma length, and the loss of material to the rear of the plasma.

(iv) The plasma eventually attains a stable length (Figs 16(c) and (h) particularly) as a result of two equilibrium conditions which are probably inter-related, viz:

- (a) the equality of the electrical power supplied to the plasma and the energy losses due to radiation and conduction, and,
- (b) the equality of the rates at which material enters the plasma from the rail and wall materials and the rate of deposition from the trailing edge.

4.1.3 Aluminium Versus Copper Foils

Having considered the development of the plasma initiated with a copper foil, it is informative to now assess differences in the plasma development phase when an aluminium foil is used for initiation. From the table below, and that of Section 4.1.2, it can be seen that aluminium needs more energy per gram than copper to attain all of the higher energy states. This is particularly significant for vapourization and ionization.

Energy Steps Associated with Ionizing Aluminium

Condition	Energy (J/mg)	
	Increment	Progressive Total
To heat to melting point	0.66	
Latent heat of fusion	0.4	1.1
To heat to boiling point	1.9	3.0
Latent heat of vapourization	11	14
To achieve first level ionization	21.5	35.5

In principle the muzzle voltage, power, and energy plots should reflect the difference. Plots of the above parameters from experiments using aluminium foil do show increases compared with copper during the plasma initiation phase (Figs 19, 31, 33).

Because of the higher energies entailed, plots for aluminium-foil shots emphasize non-linearities mainly caused by change in the 'foil' resistance during plasma development. Fig. 18(b) shows plots of current and its time derivative ($I\dot{}$), muzzle voltage, and capacitor voltage for the first 100 μ s of electric shot-life. Times corresponding to the calculated energies for the foil to melt, to start vapourizing, to completely vapourize, and to ionize to the first level are marked. Muzzle voltage waveform features can be readily associated with the higher three energy states of the foil.

The current waveform has a definite break in slope at the commencement of vapourization. The slope changes from an initial 206 MA/s to 135 MA/s and maintains the new slope for about 30 μ s through foil vapourization and initial plasma development. The changing foil/plasma resistance is reflected also in the discharging capacitor voltage waveform and the $I\dot{}$ waveform, which are clearly non-cosine.

A further feature of the RIP307 muzzle voltage waveform, which may bear on the way in which the plasma initiates, is the step of approximately 100 volts which occurs at electric shot-start and is maintained at least for about the first ten microseconds. If the foil to rail connections were purely resistive, the muzzle voltage would approximately follow current at that time. The existence of a voltage step, however, is more consistent with the presence of arcs from the foil edge(s) to the rail(s). Arc marks have in fact been observed in the vicinity of electric shot-start on the rails of a number of shots. The growth of muzzle voltage after 10 μ s is closer to the expected profile, but may consist of the foil $I\dot{}R$ voltage plus an edge-arc voltage component.

The model of the plasma during growth and stabilization, which emerges in the previous Section 4.1.2 and above, will be re-examined later in this report in the light of other experimental evidence presented in Sections 4.2, 4.3, and 4.4.

4.2 Currents and Voltages

4.2.1 Discussion of Experimental Records and Energy Distribution

A selection of records is given in Fig. 19. The records cover five broad areas of interest:

- (1) The broad features of the current plots are the sinusoidal rise to peak current, the operation of the crowbar switch after the peak current is reached, the more-or-less linear fall of current until shot out and the increase or decrease in slope at shot out.

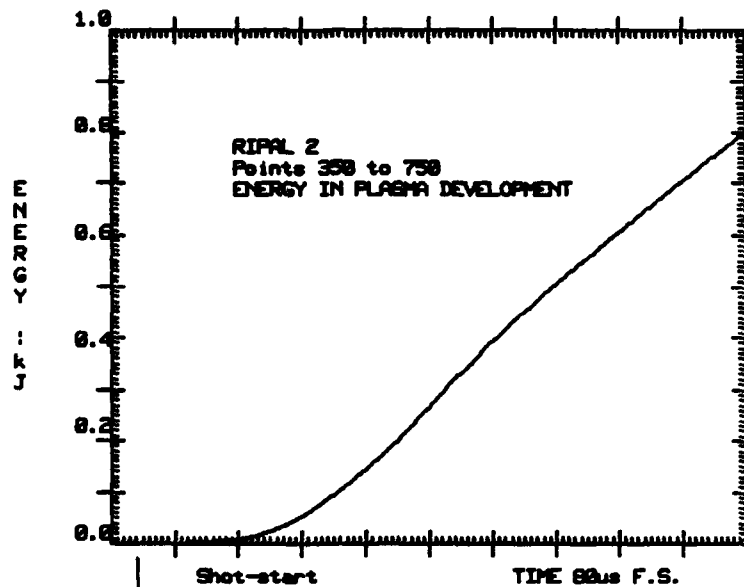


FIGURE 18(a) Armature energy plot for RIPAL firing. Copper foil - 40 mg

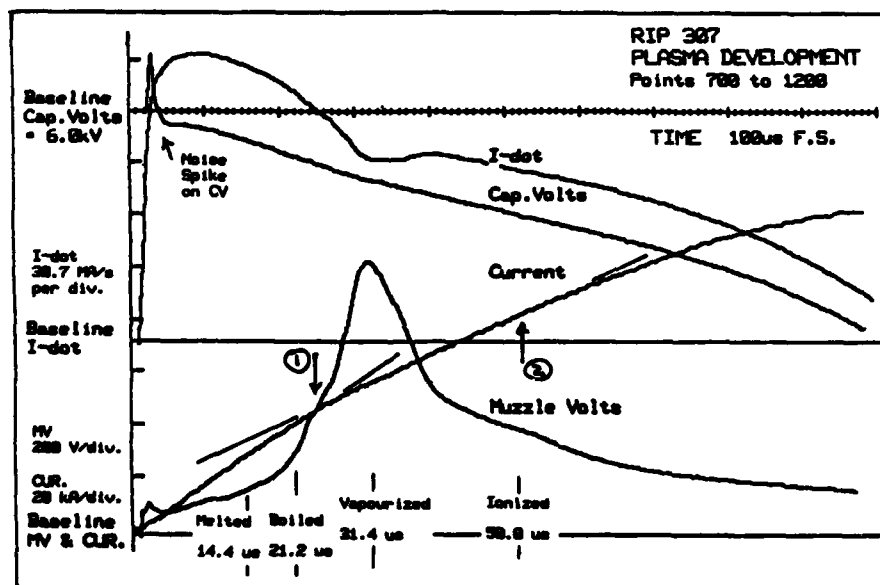


FIGURE 18(b) Plot of various gun parameters during the plasma development phase. Variations from 'constant-loss' waveforms are highlighted. The aluminium foil mass was 38 mg.

The rise of current to peak value is usually closely sinusoidal, but its amplitude is less than that which would be obtained if all the energy of the capacitor bank was transferred to the inductor. By plotting or recording the time derivative of the current waveform (Fig. 19(j)), the influence of other events can be detected. The foil explosion and the modulation of the rundown, after crowbar, by oscillation in the crowbar circuit, are examples.

Figs 19 (f) and (j) show that the crowbar switch operated from 20 μ s to 40 μ s after peak current instead of exactly at the peak. During this time the capacitor bank was reverse-charged to about 1 kV. As was discussed in the case of the foils behind the projectiles, time is required to supply the vapourization energy to the fine wire which triggers the crowbar switch. Although the mass of the wire (1 mg) and the vapourization energy (6 J) are much less than for the foils, the impedance of the diodes limits the power to the wire so that it does not vapourize in a correspondingly shorter time. Another reason for the delay is that the main switch and railgun arc voltages cause a delay in the time at which the capacitor bank voltage reverses compared to the time at which peak current occurs. The delay, A_t , is given by:

$$A_t = \sqrt{LC} \arcsin \left(\frac{V_A}{V_C - V_A} \right)$$

where L is the circuit inductance (6.3 μ H), C is the capacitance (2000 μ F), V_C is the voltage to which the capacitor bank is charged (6 kV) and V_A is the sum of the main switch and railgun arc voltage drops (100 V + 200 V). For the values quoted, A_t is about 6 μ s. This is a minor component of the total delay. It is possible that the crowbar electrodes require a minimum bias of about 1 kV to establish a stable arc, and the large delay is unavoidable.

After the crowbar operates, the railgun circuit consists of the inductor, the arc drops of the crowbar switch and of the railgun plasma, resistance of the inductor and busbars and the increasing inductance and resistance of the railgun. These latter two quantities are small compared with the other quantities and the decline of current after crowbar is determined primarily by the crowbar and railgun plasma arc drops, the power supply resistance and the circuit inductance. The decline of current after crowbar in Figs 19 (e) to (i) are about 88 A/ μ s. Since the sum of the arc voltage drops was about 300 V, the above decline implies that the sum of the inductor and busbar resistances was about 3.5 m Ω .

(ii) Muzzle voltage records are actually recordings of the voltage drop across the plasma armature. Figs 19 (a) to (i) are records from the series. There are three main features:

- (a) The region containing the voltage spike near the beginning.
- (b) The following almost constant low-voltage region.
- (c) Finally the region in which there is a rise in voltage when the plasma arc expands as a muzzle flash at exit from the rails.

The first two regions provide vital information for constructing plasma models.

The region containing the voltage spike is produced during the transition from ohmic conduction of the foil to initial arc conduction. As was discussed in Section 4.1.2, the time at which the spike occurs agrees with simple calculation of the time required to supply the foil with the necessary vapourization energy. Spike voltages were in the range 800 V to 1200 V for all firings.

The extended low voltage region implies a copious and stable rate of production of electrons. The electrons are probably produced by both surface emission from the rails and ionization within the plasma [12] that is rapidly produced by the initial arcs. The voltages are in the range 140-180 V, for currents in the range 60 kA - 120 kA. There is often a shallow minimum in the voltage in this region. We have not been able to correlate the minimum with any other features. Voltages lower than 140V have never been observed in MRL experiments. Despite the common features, it can be seen that there is considerable variation between waveforms in the low voltage region.

The dip in muzzle voltage at shot-out for some shots results from the use of large spark-spreading electrodes on the ends of the rails for those shots.

Some records in the SUBAC, RIPAL, and RIPLAM group of firings were very noisy in the time band around peak current, the RIPAL 2 muzzle voltage record (Fig. 19(h)), being particularly bad. The problem only occurred after the mechanical and electrical change-over to an ignitron main switch, and was confined to pre-crowbar events. The cause was not determined. For the RIPAL2 record, therefore, it was not possible to distinguish between what might be a real effect of an aluminium insert and noise. The large negative voltage spike on the RIPAL 2 record at about 170 μ s is probably associated with the fault.

(iii) Figs. 19 (k) and (l) show armature conductance plots for a selection of the firings. This is the so-called static conductance, i.e. the simple ratio of armature current to muzzle voltage. Peak conductance occurs close to or a little after peak armature current, and peak values are greater at the greater currents. For the 82 kA (peak) firings, peak static conductance is in the range 500 S to 600 S. For the copper-foil RIP 306 and RIP 311 shots, the variation in conductance during plasma development, and the dip corresponding to full vapourization of the foil are conspicuous.

Plasma resistivity has not been calculated. This would require detailed data on plasma length and current distribution in the plasma.

(iv) Further important information which can be derived from the current record is the distribution of the energy of the capacitor bank during transfer to the inductor.

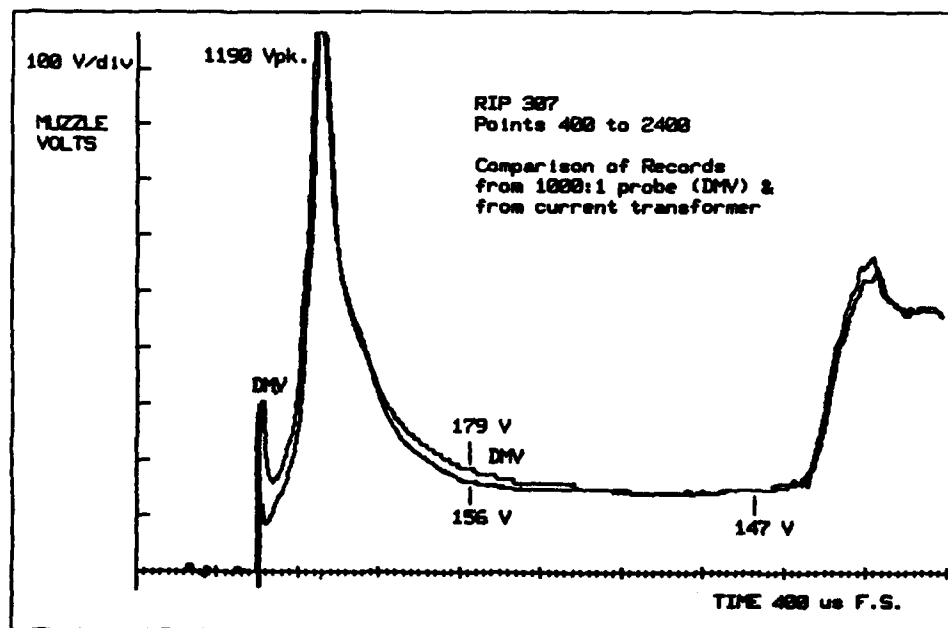
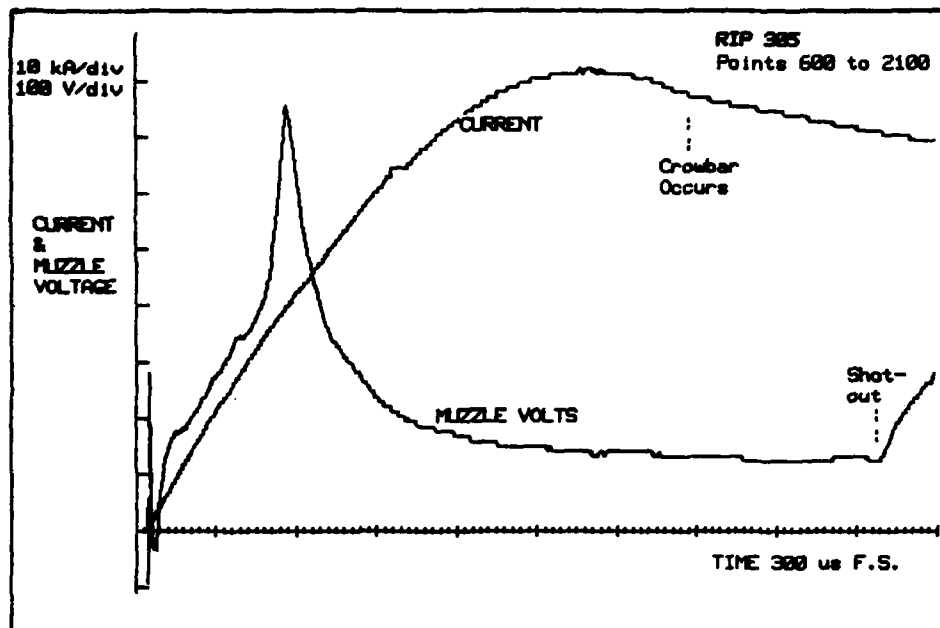


FIGURE 19 (a) and (b) Current and muzzle voltage plots

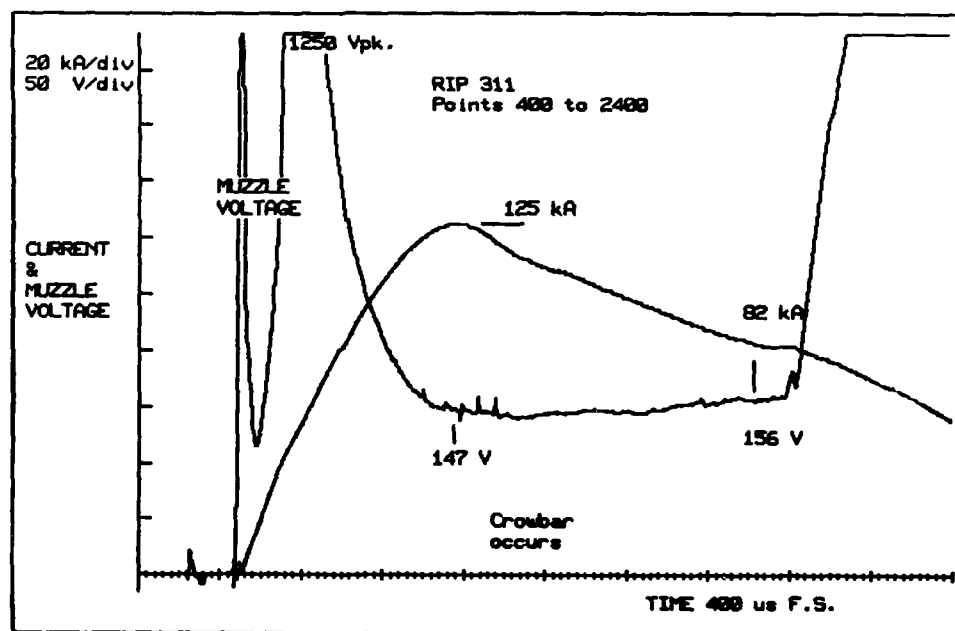
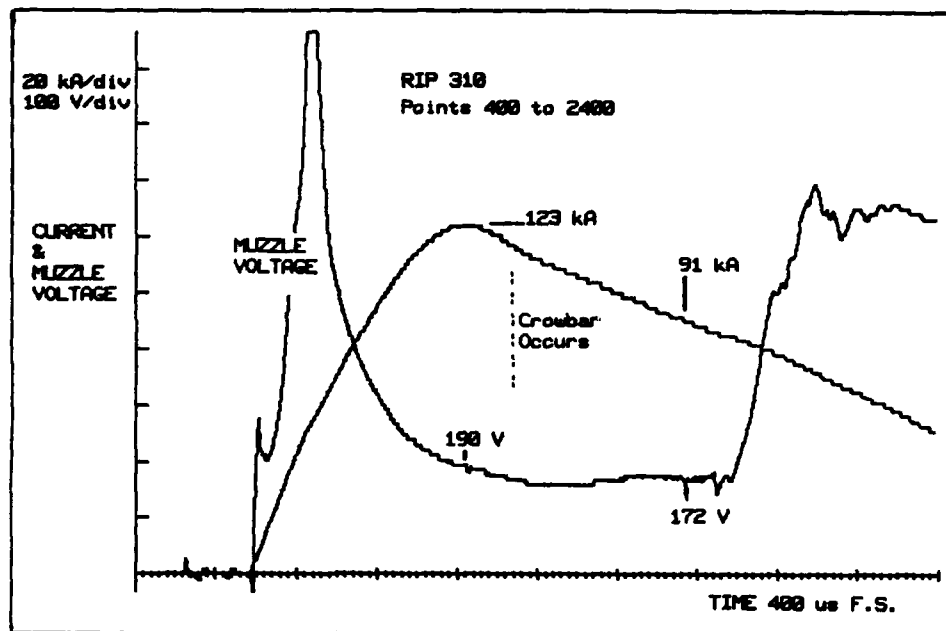


FIGURE 19 (contd) (c) and (d) Current and muzzle voltage plots

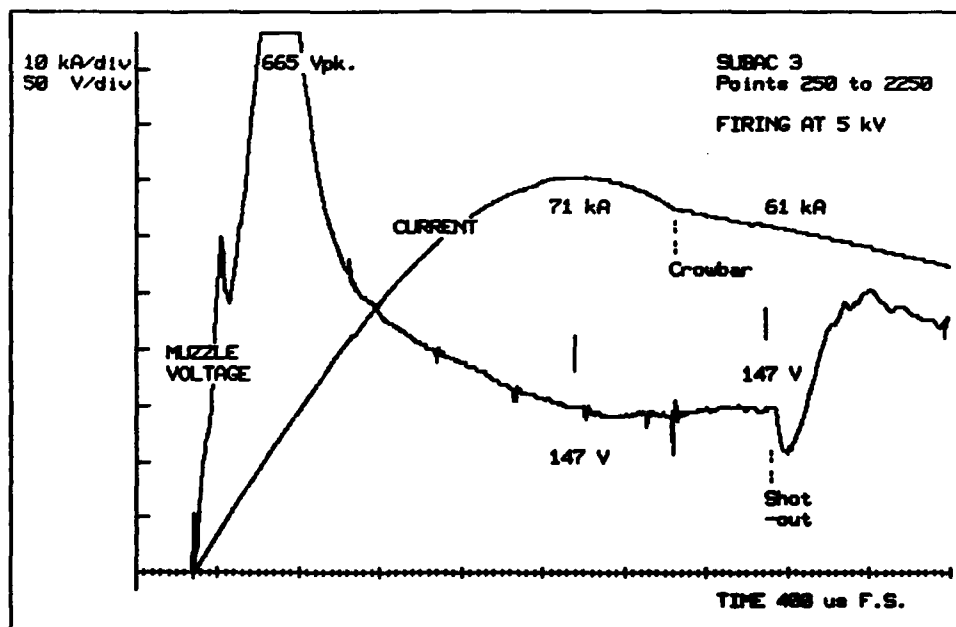
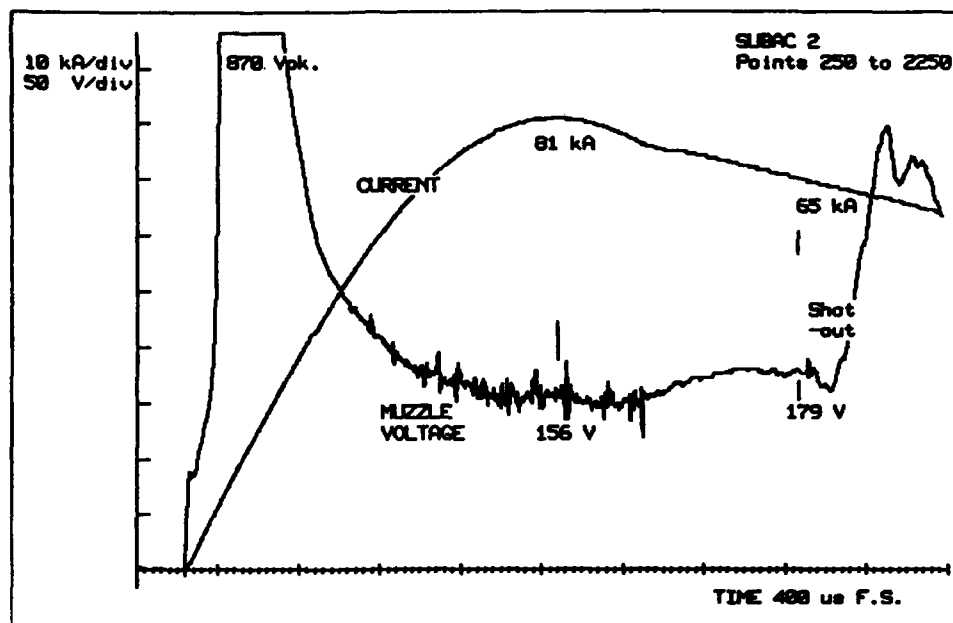


FIGURE 19 (contd) (e) and (f) Current and muzzle voltage plots

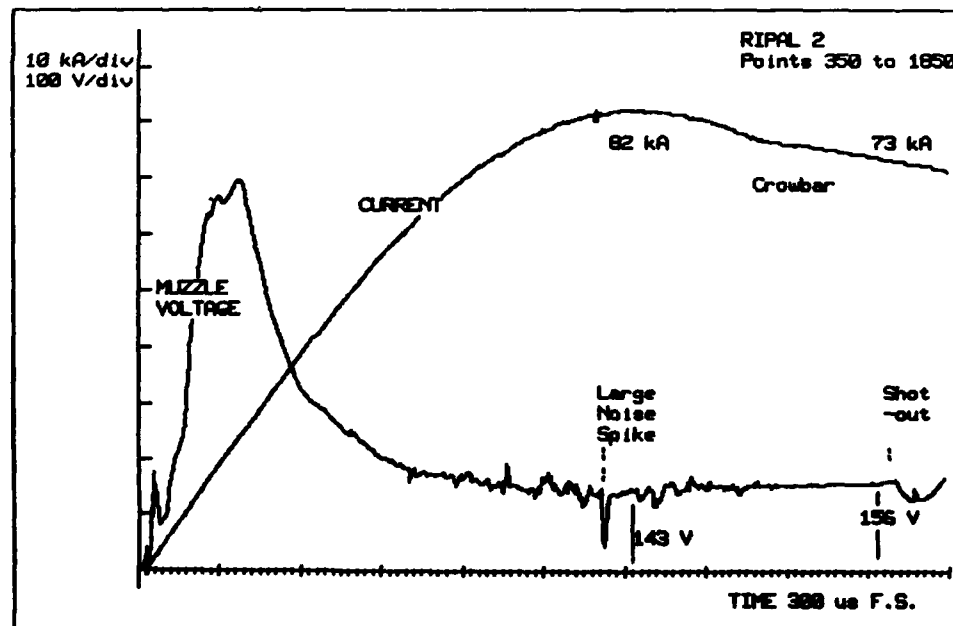
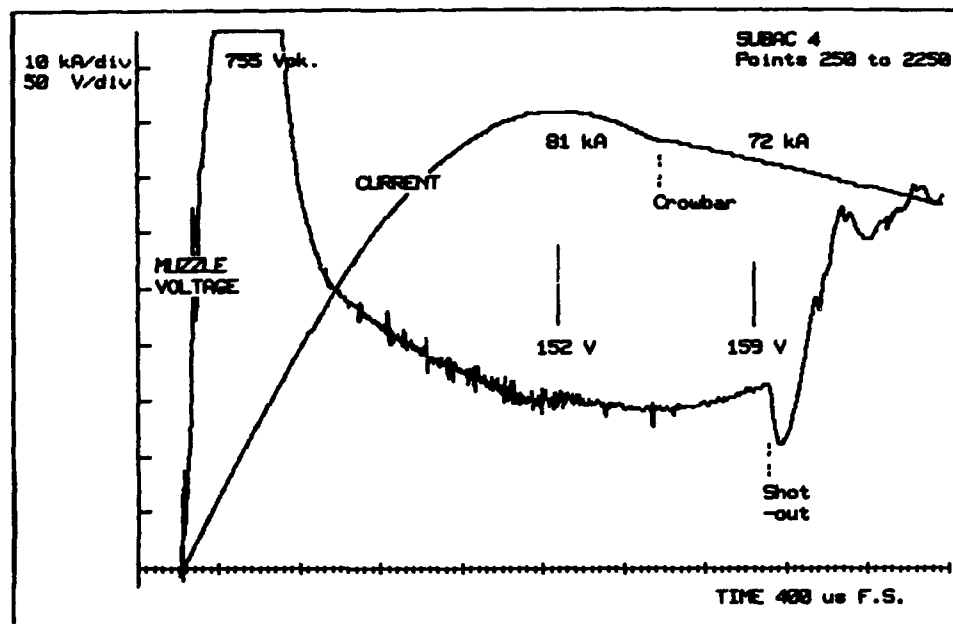


FIGURE 19 (contd) (g) and (h) Current and muzzle voltage plots

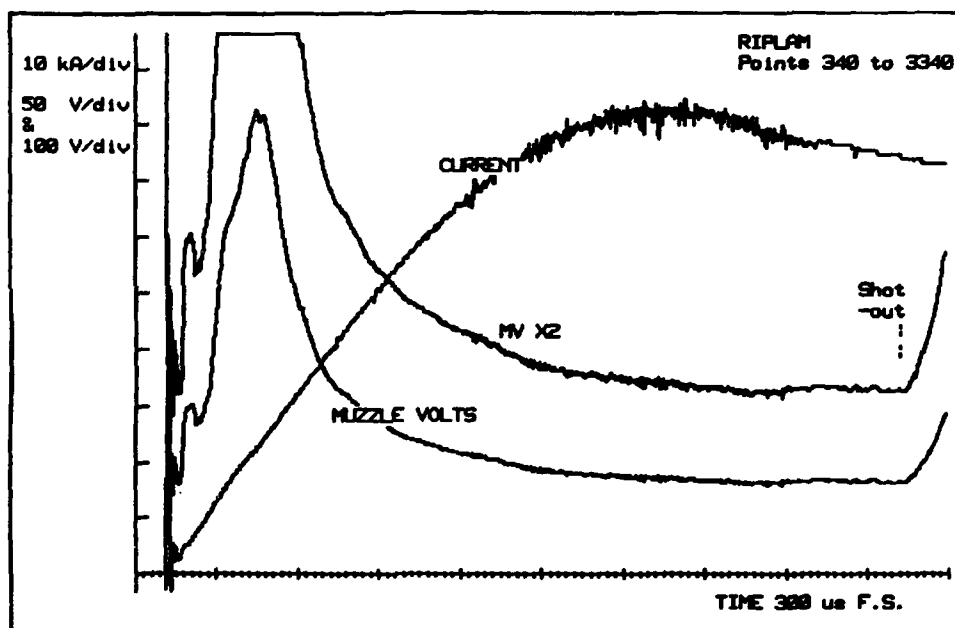


FIGURE 19 (contd)

(1) Current and muzzle voltage plot for the shot using rails with insulating stripes.

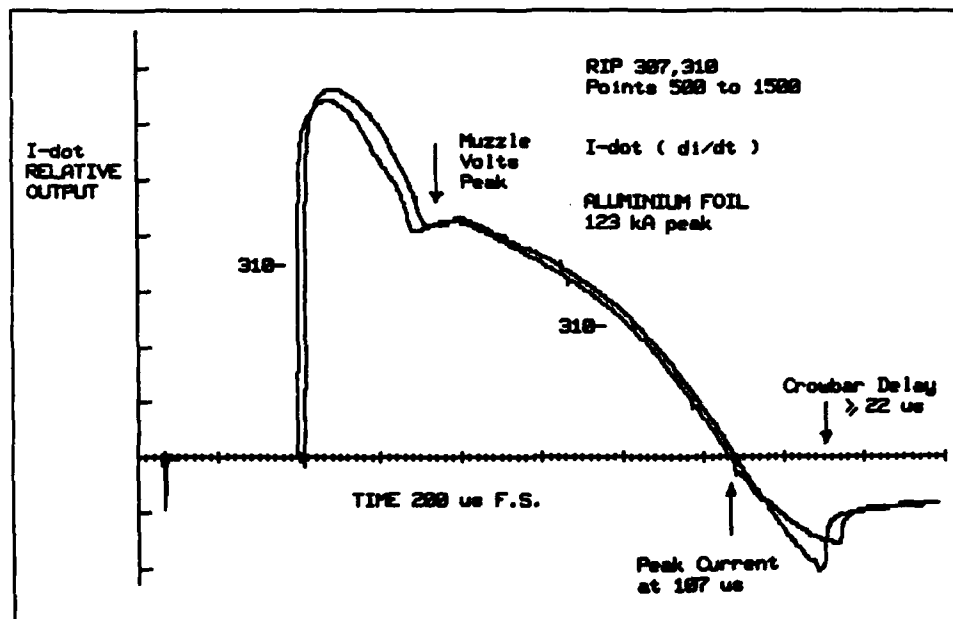
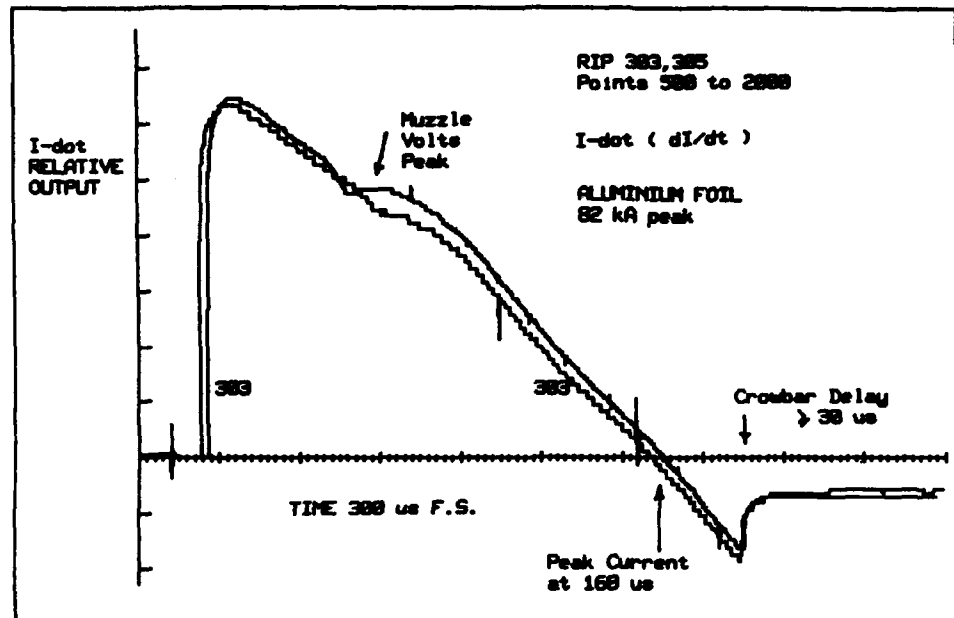


FIGURE 19 (contd)

(j) Typical di/dt for aluminium-foil shots. Constant circuit damping would cause a cosine-shaped waveform.

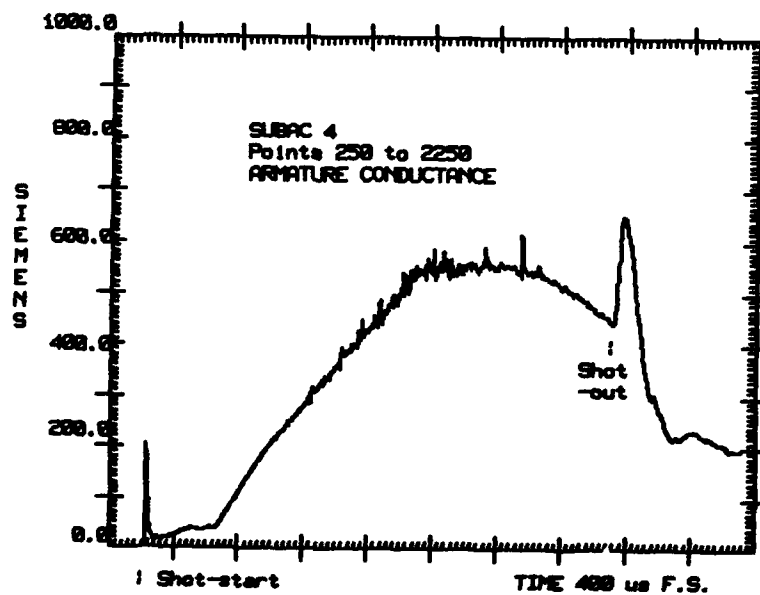
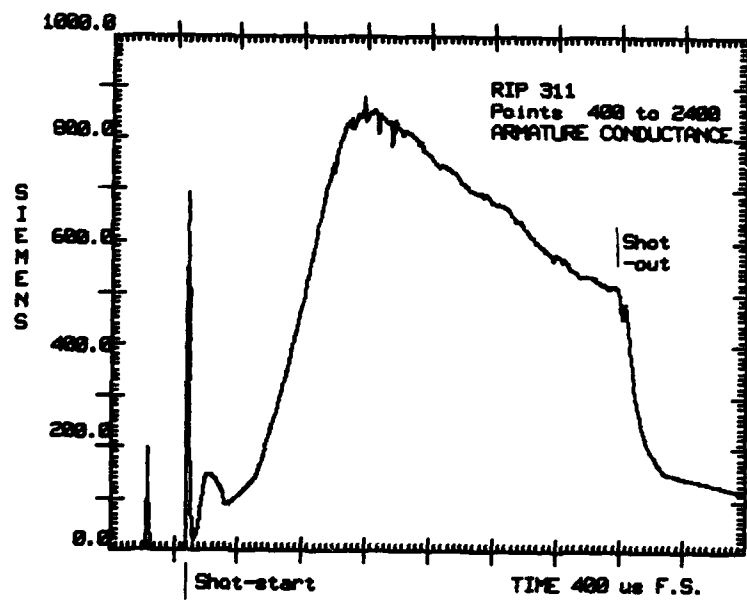


FIGURE 19 (contd) (k) Plasma conductance plots for the aluminium-foil RIP 311 (1.5 μ H) and for the copper-foil SUBAC 4

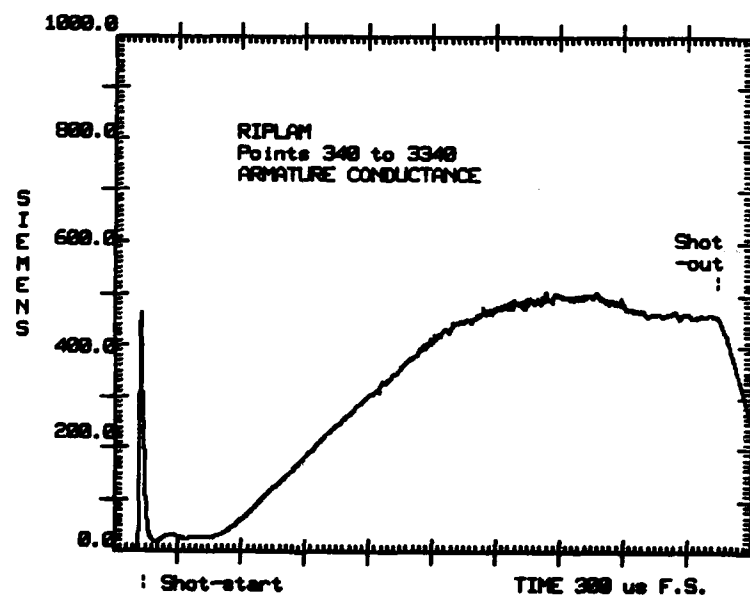
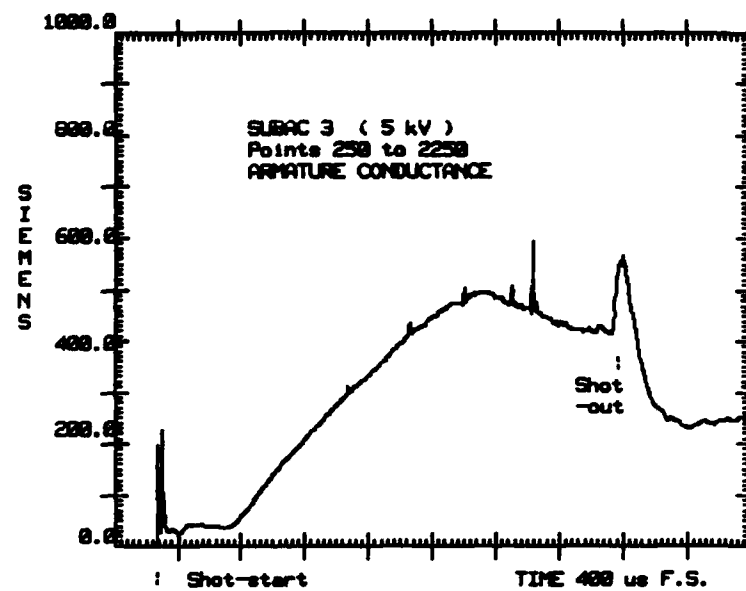


FIGURE 19 (contd) (1) Whole-of-life plasma conductance plots for copper-foil SUBAC 3 (5kV) and RIPLAM (striped rails)

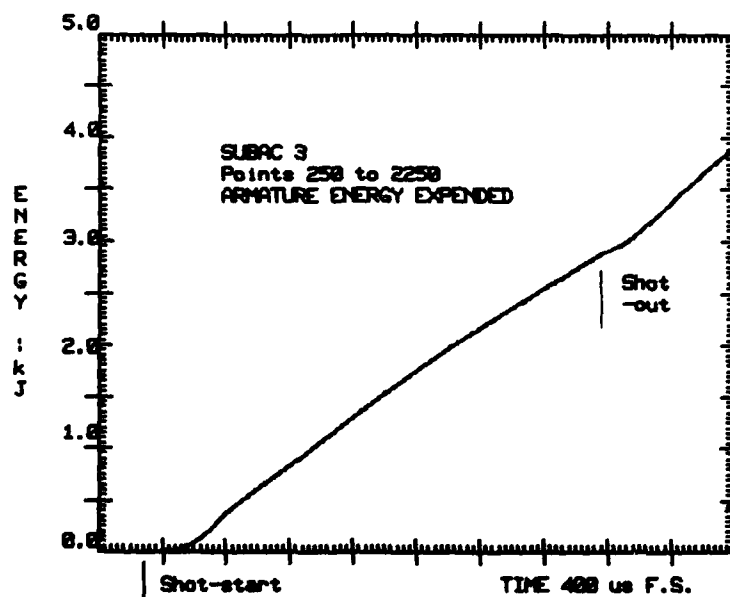
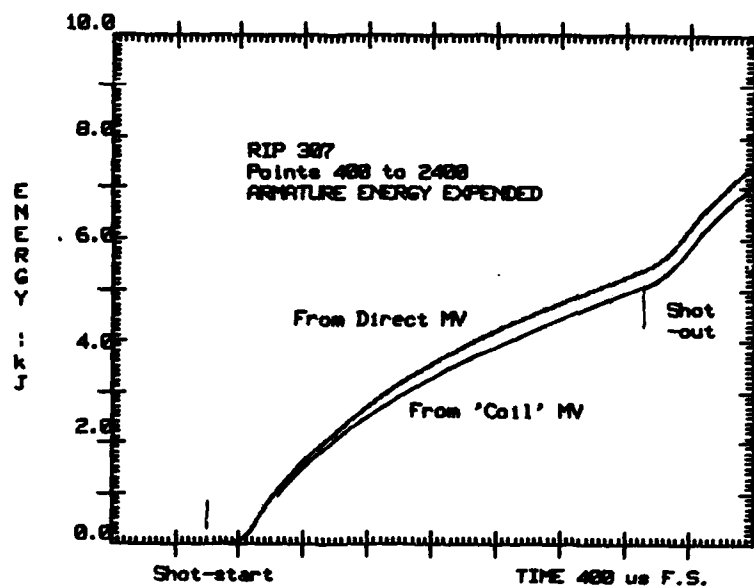


FIGURE 19 (contd) (m) Whole-of-life energy plots for the 1.5 μ H RIP 307 and the low-energy (5kV) SUBAC 3.

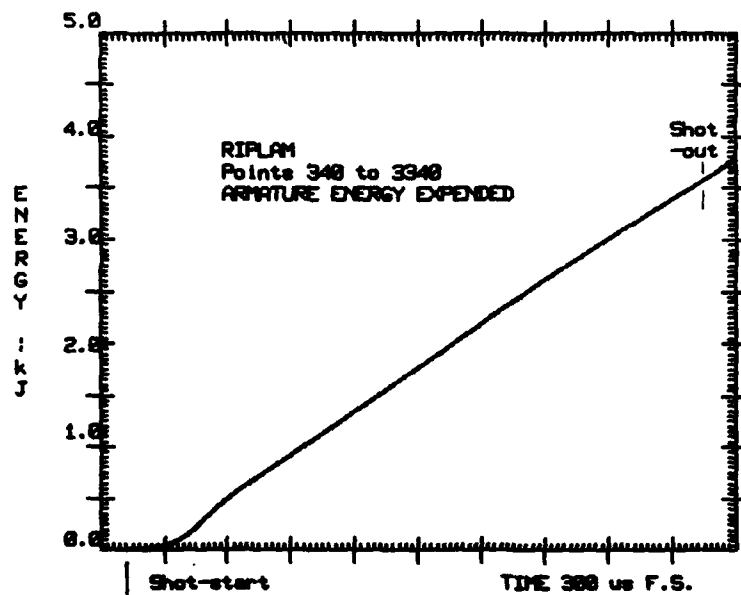
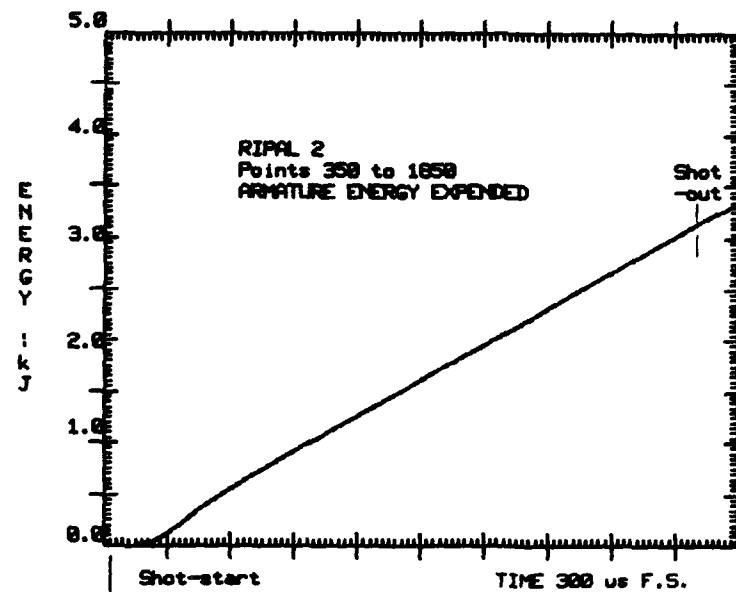


FIGURE 19 (contd) (n) Whole-of-life energy plots for copper-foil RIPAL 2 (with aluminium insets) and RIPLAM (striped rails).

To calculate the energy distribution accurately it is first necessary to evaluate the circuit resistance and stray inductance. Since, for copper-foil shots, the current plots (Fig 19) are closely sinusoidal, the total inductance, L , can be found from the measured quarter cycle time, $T_{1/4}$, and the known capacitance, C , from

$$T_{1/4} = \frac{\pi \sqrt{LC}}{2}$$

Substituting the measured value of $T_{1/4}$ from Fig 19 (e), viz 184 μ s, and $C = 2000 \mu$ F, yields $L = 6.9 \mu$ H. The measured value of the inductor was 6.3 μ H; therefore the stray inductance is approximately 0.6 μ H.

The resistance during charging can be found from the measured peak value of the current, I_p , and an expression for the peak value of a lightly damped sinusoidal current, viz:

$$I_p = (V_c - V_A) \sqrt{\frac{C}{L}} \exp\left(-\frac{R}{2L} t\right);$$

where V_c is the capacitor bank voltage and V_A is the sum of the arc drops. From Fig 19 (e) $I_p = 82$ kA at $t = 184 \mu$ s. Setting $V_c = 6000$ V and $V_A = 300$ V and solving for R yields:

$$R = 12.6 \text{ m}\Omega$$

Since (from (i) above) the crowbar-circuit resistance is 3.5 m Ω this leads to the circuit diagram for the railgun during charging of the inductor as given in Fig 20, and to the energy distribution at peak current as listed below.

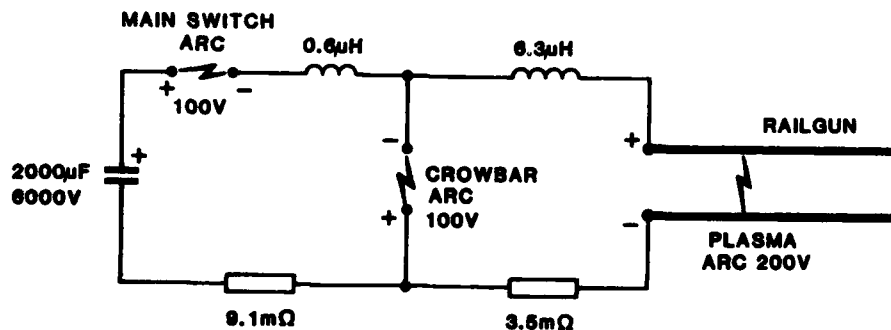


FIGURE 20 Circuit parameters during charging of inductor

Energy Distribution - kJ

Initial energy of capacitor bank	36
Energy transferred to 6.3 μ H storage inductor	21.2
Energy in 0.6 μ H stray inductance	2
Energy in 12.6 m Ω resistance	8
Energy in arc drops	3
Energy unaccounted for	1.8

From the energy plot of Fig. 19 (n) for RIPAL 2, i.e. the energy calculated from current and voltage data, the total energy expended in the armature to the time of peak current was 2 kJ. This agrees with a calculated estimate of 2 kJ, i.e. two thirds of the listed 3 kJ.

(v) The breech voltage is related to the plasma voltage drop, the current and the rail resistance and flux linkage induced voltage components by:

$$V_B = RI + L \frac{\partial I}{\partial t} + I \frac{\partial L}{\partial t} + V_p;$$

where V_B = breech voltage
 R = resistance of rails from breech to projectile position
 L = inductance of rails from breech to projectile position
 V_p = plasma voltage drop which might include a dI/dt component.

Fig. 21 shows two breech voltage records. For RIPAL 1, excessive noise before crowbar makes the record difficult to interpret. Subtraction of the muzzle voltage to determine rail losses is possible in principle, but generally the result is not very useful because, for these experiments, noise is of a similar magnitude to the additional components from changes in the parameter values.

The above expression for V_B has been used to obtain an estimate of L' as shown in the next Section.

4.2.2 Estimate of L' from In-Bore Data

When the crowbar switch operates, the current waveform changes suddenly from sinusoidal to a ramp with a short settling interval. The change in dI/dt should cause a voltage step, ΔV , to be present in the voltage waveforms, where ΔV is given by $(\Delta V_B - \Delta V_p)$; i.e.

$$\Delta V = L A \left(\frac{\partial I}{\partial t} \right)$$

Since the plasma has negligible inductance, ΔV is zero and hence:

$$\Delta V_B = L A \left(\frac{\partial I}{\partial t} \right)$$

Such a step in V_b can be seen in Figs. 21 and 22. Its magnitude is not accurately available from these records, but with deliberate attention to its measurement this voltage step would enable the in-bore inductance gradient to be calculated.

Two calculations of the inductance gradient were made.

(1) RIPAL 1 Experiment

Fig. 21 shows the current and breech voltage waveforms at the time of crowbar. From the sinusoidal current waveform, given closely by:

$$I = 81.42 \sin 0.484t \quad \text{kA},$$

where t is in microseconds, the slope, just prior to crowbar at $t = 228 \mu\text{s}$, is 237 MA/s. By measurement on the current plot, the slope just after crowbar is 86 MA/s. The term $A(dI/dt)$ is thus $(237 - 86) = 151 \text{ MA/s}$.

The increment in breech voltage, ΔV_b , indicated on Fig. 21 is approximately 39 V. The inductance from the breech, where the voltage was measured, to the position of the plasma centroid at the time of crowbar was thus:

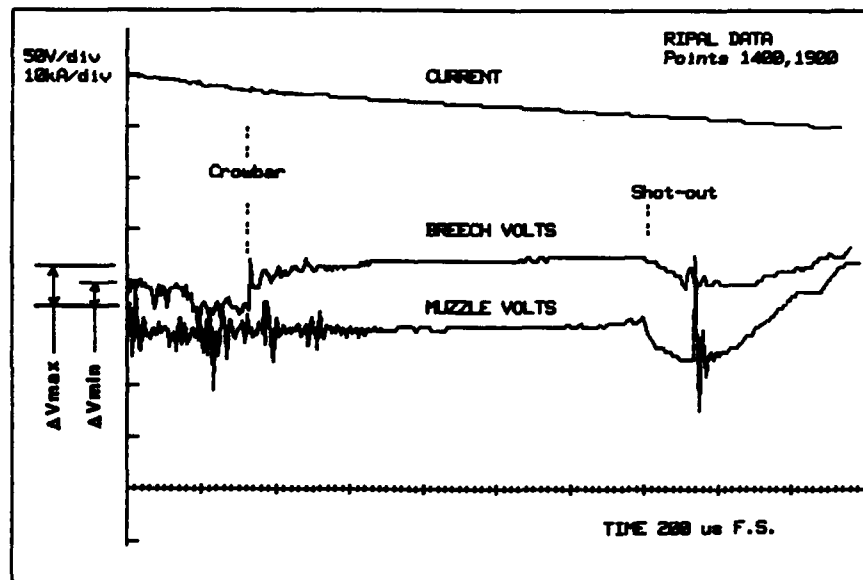


FIGURE 21 Current and breech voltage at crowbar, RIPAL 1 experiment

$$L = \frac{AV}{\Delta(\frac{dI}{dt})} = \frac{39}{151} \mu H = 0.26 \mu H$$

Using the streak photograph, Fig 16, the position of the plasma centroid at crowbar ($t = 228 \mu s$) was 374 mm from the input electrodes. The inductance per unit length of the rails was thus $0.25/0.374 = 0.70 \mu H/m$. The accuracy of this estimate is probably $\pm 30\%$ and is mostly determined by the AV_B measurement.

The above value considerably exceeds $0.407 \mu H/m$, the theoretical high frequency value of the inductance per unit length for the Ripper geometry.

(ii) Low Inductance Shot (Fig 22)

Similar calculations using the current and breech records of RIP 307 yielded a value for L' of $0.71 \mu H/m$. Fig. 22 includes an I-dot ($= dI/dt$) graph. I-dot data was obtained directly from a Rogowski belt. This data improved the accuracy of the $\Delta(dI/dt)$ value since only the ratio of I-dot amplitudes before and after crowbar is required. Nevertheless the error in measuring the breech voltage AV_B remains significant.

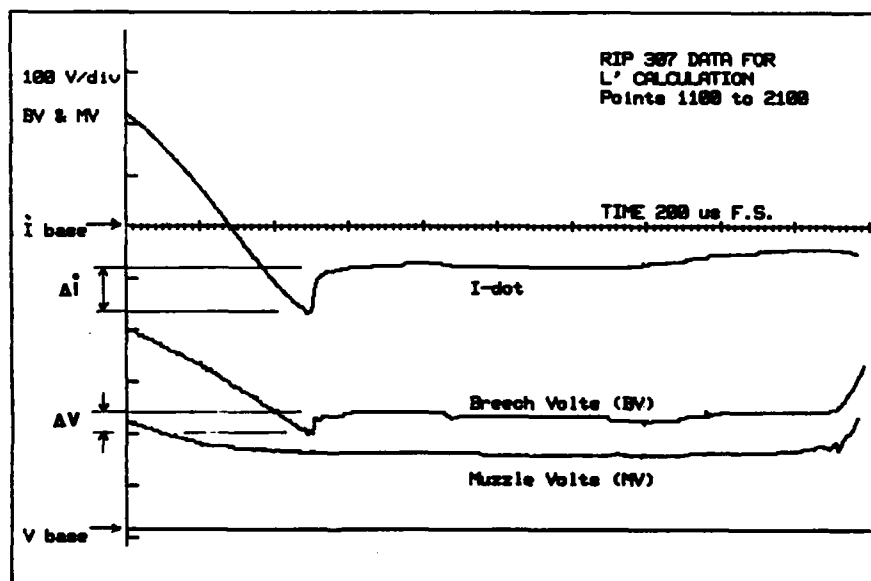


FIGURE 22 Current and breech voltage at crowbar, low inductance shot, RIP 307

It might be expected that both these measurements would produce a low figure for L' , since displacement has been non-electrically boosted. However the converse is true. Therefore the breech voltage increment is much greater than would be expected on the basis of the simple analysis. Considering the 'better' RIP 307 data, it seems unlikely that ΔV could be in error by a factor of two. This approach has not been pursued further, and the difficulty remains unresolved.

An alternative approach, not pursued, uses the fact that dI/dt is zero at peak current. Then L' is given by

$$L' = \frac{\left(\frac{V_B - V_P}{I_{pk}} \right) - R_{pk}}{u_{pk}}$$

where u is the plasma velocity, and all values are for peak current. Alternatively, rail losses could be evaluated for an assumed L' .

4.3 Magnetic Pick-up Coils

4.3.1 Need for Calculated Waveforms

Small coils placed close to the railgun bore and oriented to intercept only the plasma flux give information about the plasma length, time of arrival of the plasma at the coil position, and the current distribution within the plasma. The direct use of coil outputs to determine the time at which the plasma passed the coil is standard railgun practice. For other purposes it is necessary to compare the pick-up coil waveforms with waveforms obtained by calculation for various representative current distributions and geometrical factors.

Although pick-up coil calculations have been carried out previously [13,14], they have not been extended to a presentation of results suitable for the above additional interpretations. In Appendix 2, calculated waveforms are presented together with the plasma geometry and current distributions from which they arise.

4.3.2 Interpretations of Waveforms Obtained

Pick-up coils were used in all experiments at the locations shown in Fig. 7. The limited number of recording channels available meant that it was not possible to monitor all coils in any one firing. Representative outputs from the breech, centre and muzzle coils are given in Figs. 23-28. The outputs from the grouped coils for the sub-arc investigations are discussed elsewhere [8]. The coils were located 7.5 mm below the bottom of the bore; i.e. at 0.75 H in terms of the parameters used in Appendix 2 and Figs. 46 to 49.

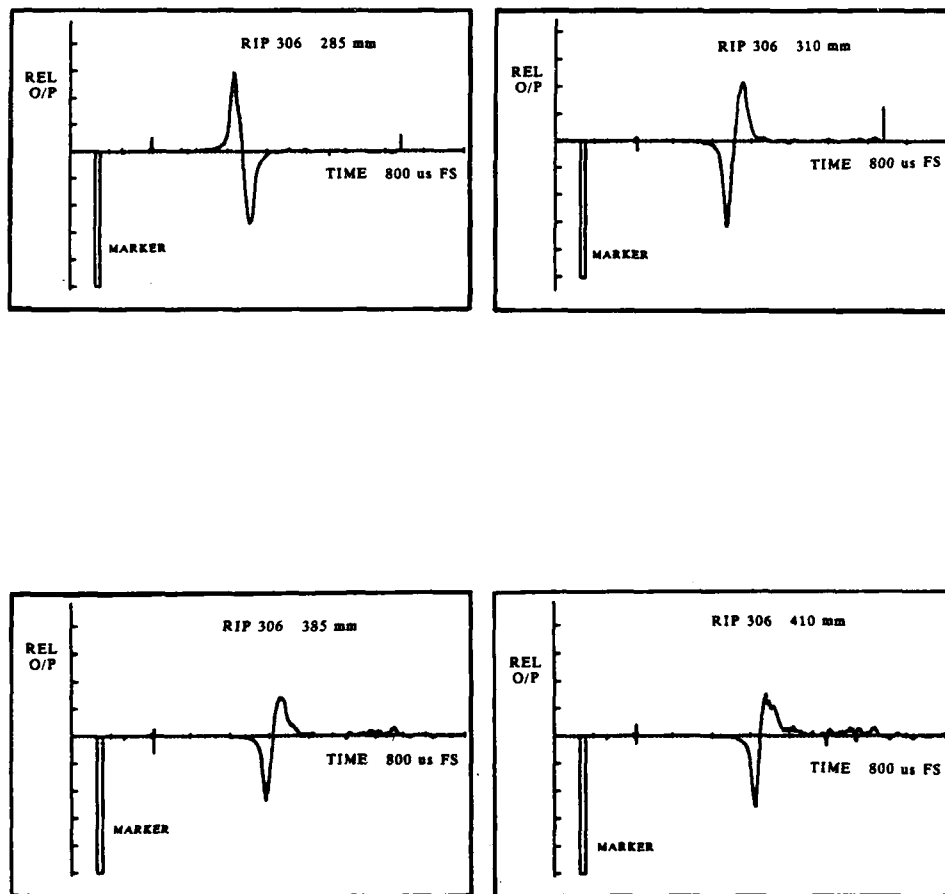


FIGURE 23 Pick-up coil waveforms at 4 locations, RIP 306: 285 and 310 mm; 385 and 410 mm from centre of current input electrodes

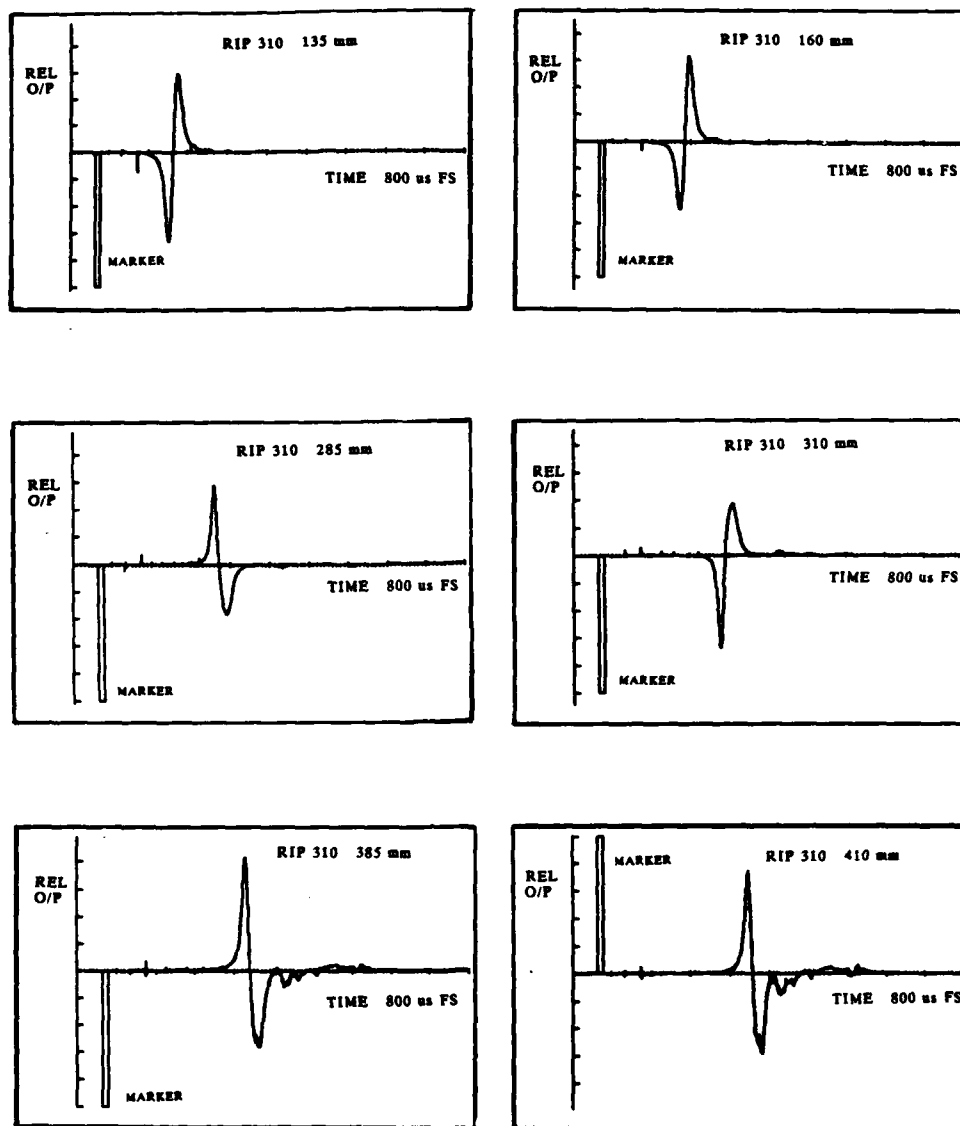


FIGURE 24 Pick-up coil waveforms at 6 locations, RIP 310: 135 and 160 mm; 285 and 310 mm; 385 and 410 mm from centre of current input electrodes

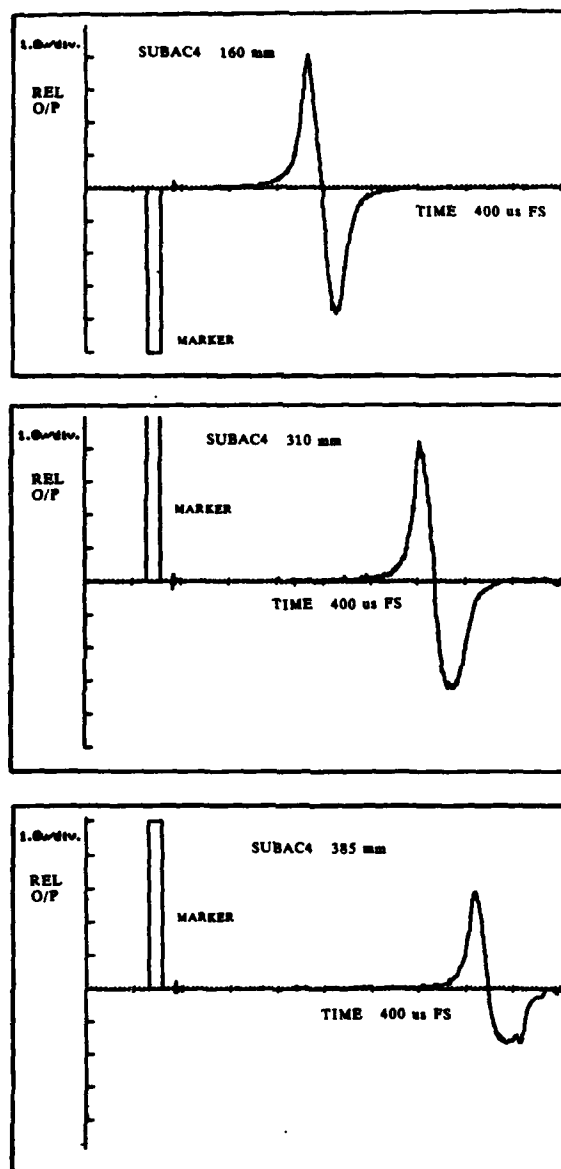


FIGURE 25 Pick-up coil waveforms, SUBAC 4: 160 mm, 310 mm and 385 mm from centre of current input electrodes

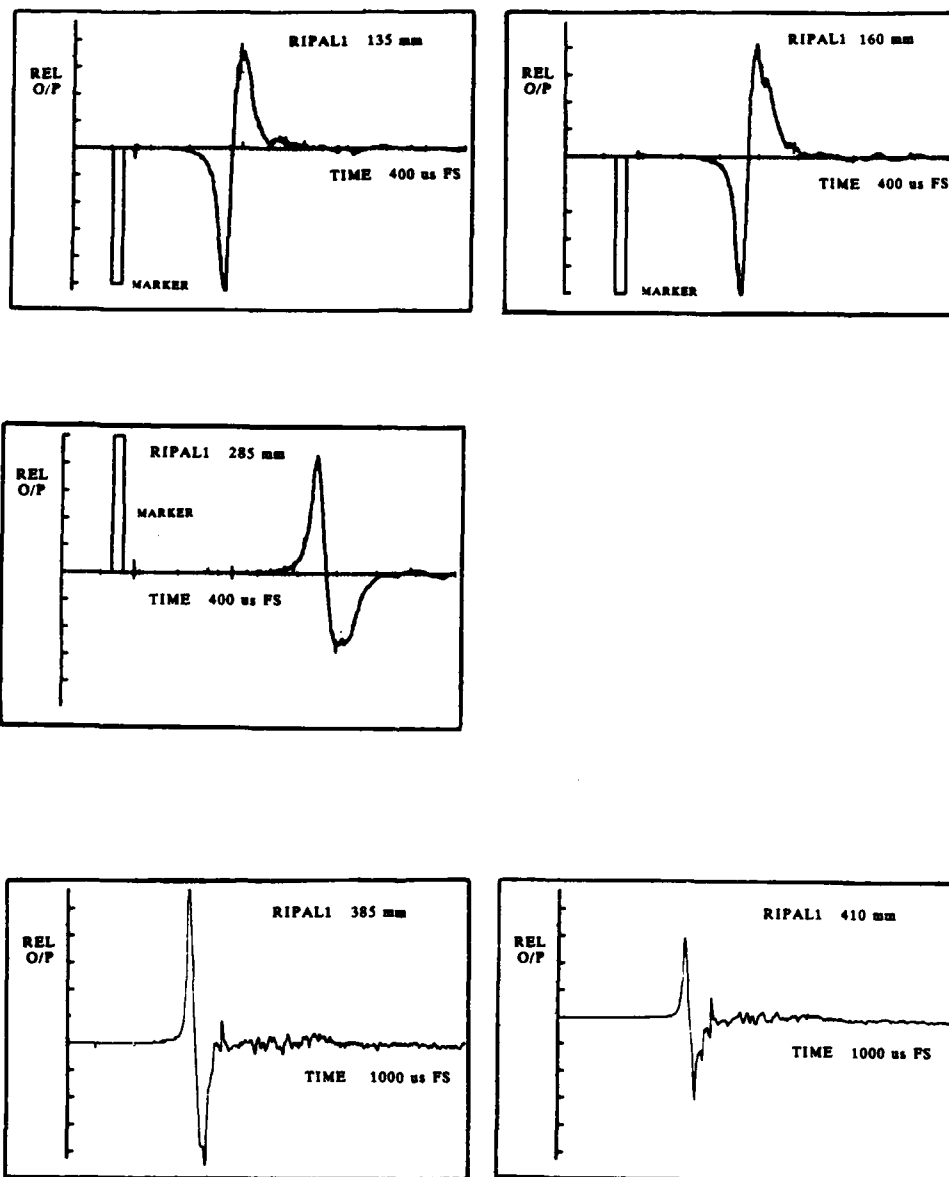


FIGURE 26 Pick-up coil waveforms at 5 locations, RIPAL 1; 135 mm, 160 mm, 285 mm, 385 mm and 410 mm from centre of current input electrodes

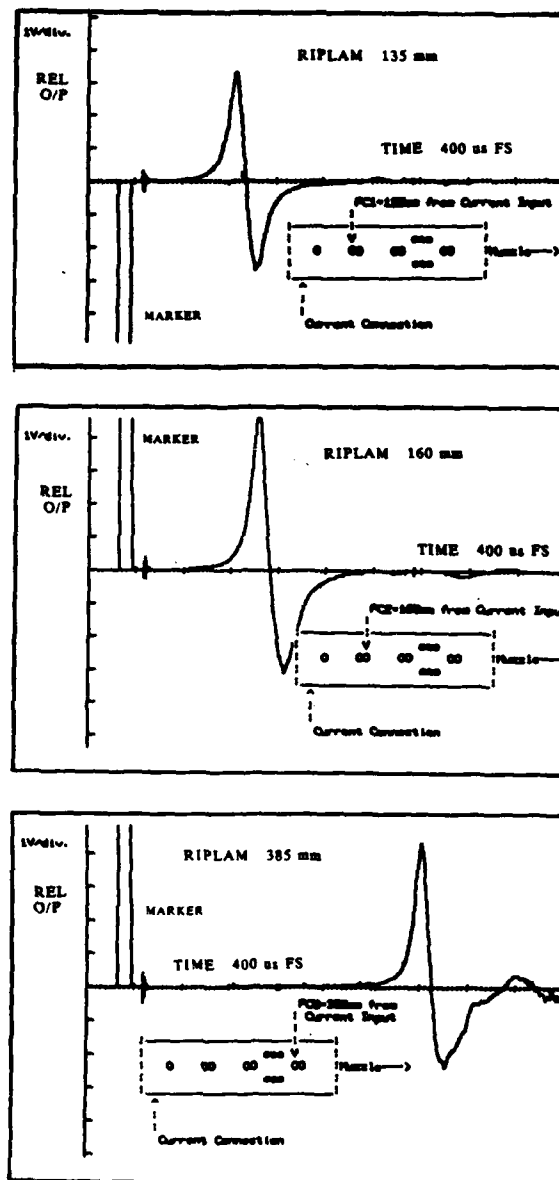
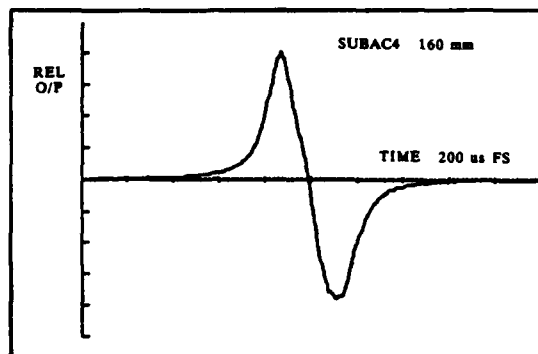
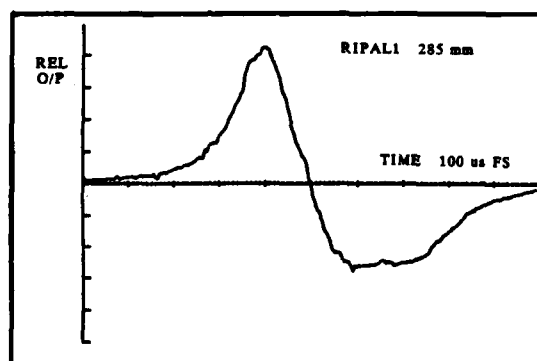


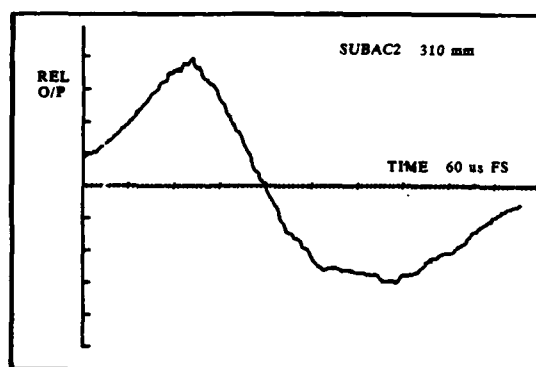
FIGURE 27 Pick-up coil waveforms, RIPLAM experiment: 135 mm, 160 mm and 385 mm from centre of current input electrodes



SUBAC 4
160 mm



RIPAL 1
285 mm



SUBAC 2
310 mm

FIGURE 28 Expanded magnetic pick-up coil waveforms

(1) Times of Occurrence of Peaks and Zero Cross-overs

The times at which the peaks and the zero cross-overs of the output waveforms occur are tabulated in Appendix 1 together with data relating the position of electric-shot-start to the coil position datum.

The calculated waveforms show that the coil output passes through zero when about half the current has passed the pick-up coil. For non-uniform current distributions this also corresponds to the region of greatest current density in the plasma. The zero cross-overs may therefore be used to plot the position of the so-called current 'centroid' versus time and this is commonly done to obtain a position-versus-time plot from barrels when streak photography cannot be used. In the experiments reported here the coils were frequently used in pairs to obtain spot velocities which could be used in conjunction with streak photography to determine the distribution and motion of current within the plasma.

Unfortunately, the data gathered is incomplete. It is clear, though, that the velocities of the current centroid can differ from those obtained from the streak leading edge. For example, the RIPAL 2 zero cross-over times at 135 mm and 160 mm differed by 18 μ s, and hence imply a velocity of 1400 m/s. The velocity obtained from the streak leading edge however is

1550 m/s. The RIPAL 1 zero cross-over time difference was 15 μ s, indicating a velocity of 1667 m/s. Since the two streak records are virtually identical, the results suggest that the current centroid may move within the plasma.

The times at which the peaks and zero cross-overs occur can be plotted on the streak photographs to gain further information about the current distribution and centroid location within the plasma. An example is given in Fig. 29. As discussed in Appendix 2 and below, the location of the peaks in relation to the current distribution is dependent on several factors.

(ii) Plasma Length Estimates and Current Distribution

The calculated waveforms in Appendix 2 show that the peaks of the waveforms occur when the ends of the plasma (or, strictly when the ends of the current-carrying portions of the plasma) pass the coil, provided however that the coil is close to the plasma and the current is uniformly distributed. Under these conditions the length of the plasma may be estimated by multiplying the time interval between the peaks by the velocity at the coil location. Comparison of the lengths determined in this way with the lengths of the hottest portion of the plasma from a streak photograph enables the uniformity of the actual current distribution within the plasma to be inferred.

The lengths obtained from the pick-up waveforms in these experiments were generally less than those obtained from the streak photographs. Examples for two firings are given below. The RIPAL 2 data at 310 mm and 385 mm gave pick-up coil determined lengths which were only about 60% of the streak photograph determined lengths.

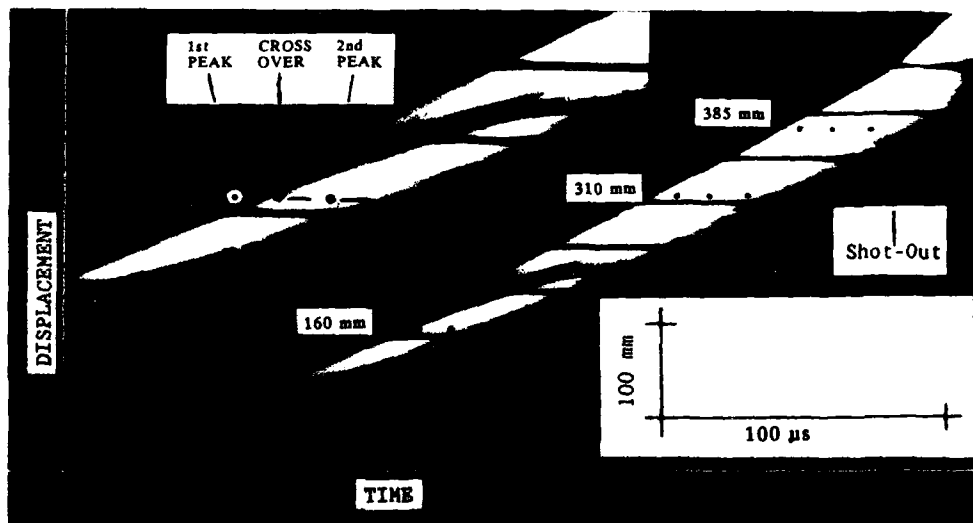


FIGURE 29 SUBAC 4 streak showing dark layer and locations of pick-up coil peaks and zero cross-over, 160 mm, 310 mm, and 385 mm
Inset: expansion at the 160 mm B-dot region

Length Estimates in mm (Pick-Up Coil/Streak)

Shot	Location, mm from current connector C/L		
	160	310	385
SUBAC 4	37/43	-	57/68
RIPAL 2	32/44	45/73	44/73

Reference to the calculated pick-up coil waveforms in Appendix 2 shows that the distance between peaks can be expected to be less than the plasma length if the current distribution is not uniform. The above results thus suggest that the current was not distributed uniformly over the length of the plasma.

In the RIPLAM shot a pick-up coil was placed 51 mm from the current input electrodes. Its output was produced about 20 μ s after the current turn-on, i.e. while the foil was still vapourizing. The apparent plasma length obtained from the time between the waveform peaks (9.5 μ s) was 11.4 mm. Although no streak photograph was taken of this shot, the shot was virtually identical to other shots which produced very similar streaks. All these other streaks show that the plasma is at most a few millimeters long at this stage. Thus, in this case, the pick-up coil data suggests a plasma which is at least four times the actual length. However, reference to the waveforms in Appendix 2 shows that for short plasmas the pick-up coil peaks will in fact occur well before and well after the plasma passes the coil.

The RIPLAM B-dot data produced a further interesting result. Comparisons of the data in Appendix 1 for shots SUBAC 4 and RIPLAM showed that the shot parameters and velocities were very similar. The only significant difference between the experiments was the difference in rail construction. The result to be noted is that the plasma length, as calculated from the B-dot data, was shorter for RIPLAM in the established-plasma shot-phase than for SUBAC 4. Of particular interest are the values at 385 mm. These results are significant because of the two types of rail construction, and imply that the RIPLAM construction resulted in shorter plasma length. Since a streak photograph was not taken of the RIPLAM shot, comparisons of the streak photograph and pick-up coil determined plasma lengths with SUBAC 4 streak are not possible.

(iii) The Nature of the Current Distribution in the Plasma

The calculated waveforms show that if the current distribution is non-uniform but symmetrical about the centre of the plasma length, the leading and trailing peaks have odd-symmetry. If the current distribution is unsymmetrical the peak produced when the region of greater current density passes the pick-up coil is sharper and of greater amplitude than that produced

when the region of lower current density passes the coil.

Examination of the actual pick-up coil waveforms shows that as distance from the breech increases, the leading peaks become sharper and of greater amplitude than the trailing peaks. The difference is greater for the centre coils and greater again for the muzzle-end coils, as compared with the breech end coils. (It should be noted that the polarity of plotted peaks is arbitrary because of the difficulty of identifying the ends of coils). Fig 28(a) shows waveforms at the 135 mm, 285 mm and 385 mm locations which show the trend more clearly.

The above results suggest that the current is approximately symmetrically distributed over the plasma length when the plasma is near the breech end and that thereafter the current tends to concentrate at the plasma leading edge and tapers to zero at the rear of the plasma.

Another inference from the pick-up coil waveforms is that the current within the bulk of the plasma, although non uniformly distributed, is nevertheless diffusely distributed. This follows because if the current passed from one rail to the other as relatively few arcs (like lightning strikes), then the pick-up coil waveforms would always exhibit odd-symmetry, like those due to short plasmas.

(iv) Interpretation of Dark Layers on Streaks

As indicated previously, plotting the time and position co-ordinates of the peaks and zero cross-overs on the streak photographs gives useful information. This however requires accurate determination of the zero time and zero position co-ordinates on the streak photograph by, for example, the super-position of time and position markers on the streak.

An interesting result of plotting as described above is the interpretation of dark regions frequently seen on streak records. Fig 29 shows such a dark region on the SUBAC 4 streak record. A dark region may be due to an opaque layer obscuring the plasma beneath it (a cloud, in effect), or it may indicate a genuine current-distribution anomaly.

The plot of the leading and trailing peaks and zero cross-over co-ordinates on the streak shows that the leading peak was in the dark region, and close behind the projectile i.e. it shows that the dark region in fact had high current density and therefore must have contained hot plasma. This reinforces the argument that the dark region was caused by an opaque layer between the plasma and the polycarbonate wall of the bore. The probable source of this opaque layer is discussed later. Fig. 16(a) shows that similar effects occurred for RIP 305.

The position of the pick-up coil waveform co-ordinates on the streak also suggests that the current was mostly carried by the forward part of the plasma.

4.4 Rail Damage

The range of experiments covered in this report provided an opportunity to study damage from the perspectives of:

- (i) armature power;
- (ii) the plasma initiating foil;
- (iii) I²R contribution;
- (iv) rail material;
- (v) rail construction and
- (vi) arc track damage.

The studies are of a non-metallurgical nature based on microscope-assisted visual observation, together with a number of measurements using a Talysurf surface-roughness instrument. Reference may need to be made to the earlier Section 2.4 for a general description of the experiments, and to Appendix 1 for specific parameters and shot details.

4.4.1 Armature Dissipation

Power dissipation in the plasma armature varies during shot life, and the typical history for a group of shots depends on that group's specific parameters. This is demonstrated in Fig. 30 which depicts four power histories considered as representative of the firings conducted. It might be expected that such marked differences in the peak value of power, and history, would in some way be reflected in rail damage differences. Such differences are in fact evident.

The proposition to be examined here, however, is that the severity of rail damage is correlated to the energy density at the plasma-rail interface. In this case, armature length and velocity become relevant factors. For a square-bore gun of wall width and height ω , the surface energy density Δ is approximately:

$$\Delta = \frac{Pt}{4\omega (\lambda + \omega/2)}$$

where P is the power dissipated in the armature, t is exposure time, and λ is the plasma armature length. Using the relationship $t = \lambda/v$, where v is the plasma velocity, the expression becomes:

$$\Delta = \frac{P}{4\omega v} \frac{\lambda}{(\lambda + \omega/2)}$$

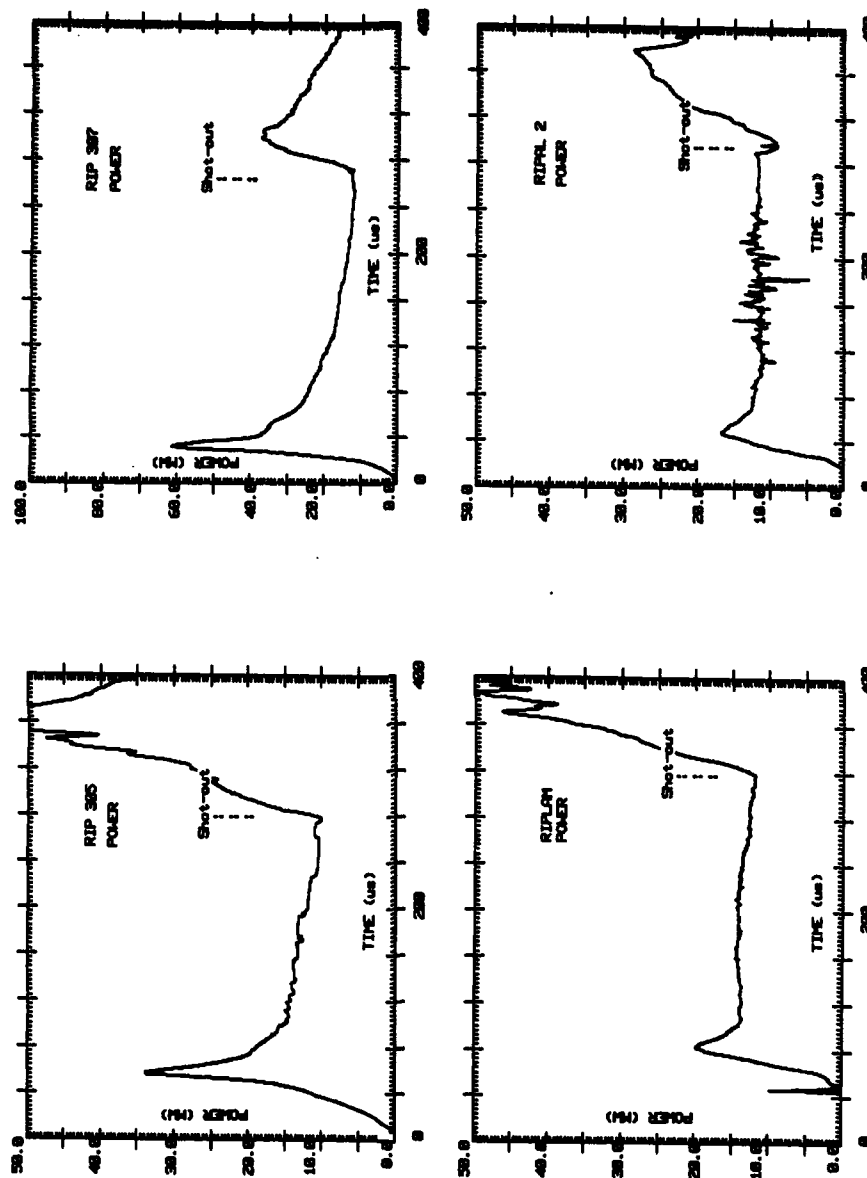


FIGURE 30 Armature power history for four firings representative of all shots

A useful simplification for armature lengths in excess of 50 mm (i.e. $\lambda \gg \omega/2$) is $A \propto (P/v)$. If the proposition was true, A could be used as a damage indicator. However, from the table below it is seen that armature lengths are generally too short for the $\lambda \gg \omega/2$ condition to apply, and hence the simplified form of A is inappropriate for this set of experiments. The table shows data for three conditions, or phases, of the four firings. These correspond firstly to the time of peak armature power, secondly to the time of peak armature (rail) current, and thirdly to a time close to shot-out, but before any shot-out disturbances occur. They were selected as being the most significant from a rail damage aspect.

**Estimated Armature Length for Representative Shots
at Three Phases of each Firing**

Firing Phase	Armature Length (mm)			
	RIP306	RIP307	RIPAL2	RIPLAM
Peak Power*	10	15	3	2.5
Peak Current	50	30	45	35
Shot-out	60	50	50	>35

* Estimated accuracy is $\pm 33\%$ for this stage

Note that the value of A is less sensitive to error in the estimate of armature length as λ increases from the few millimeters at peak power. Unfortunately the greatest uncertainty in length occurs in early shot life.

Plasma velocities required for the calculation of A are given in the following table.

**Lower and Upper Limits of Plasma Centroid Velocity
for Representative Shots at Three Firing Phases**

Firing Phase	Energy Density (^{min} / ^{max}) (MJ/m ²)			
	RIP306	RIP307	RIPAL2	RIPLAM
Peak Power	1.1/1.4	.9/1.4	1.2/1.3	1.1/1.25
Peak Current	1.6/1.7	1.45/1.55	1.6/1.7	1.6/1.7
Shot-out	1.75/1.8	2/2.2	1.7/1.8	1.7/1.8

Using the exact expression for A , and the above armature length and velocity data, the following values of A are obtained.

**Lower and Upper Limits of Rail Surface Energy Density,
A, at Three Phases of the Firings**

Firing Phase	Energy Density (^{min} / ^{max}) (MJ/m ²)			
	RIP306	RIP307	RIPAL 2	RIPLAM
Peak Power	.33/.58	.72/1.3	.091/.15	.10/.18
Peak Current	.15/.16	.33	.16/.17	.16/.17
Near Shot-out	.12/.13	.12/.14	.14/.15	.13/.14

An immediate observation is that, even allowing for armature length and velocity uncertainties, the rails of the aluminium foil RIP306 and RIP307 shots experienced significantly greater energy density at the peak-power phase than the other two shots. To enable a correlation of energy density and damage to be made for shots RIP 306 and 307 it is necessary to know the position of the plasma at the time of the relevant phase. These data are given in the table below.

Armature Displacement Data for RIP306 and RIP307

Shot	Firing Phase					
	Peak Power			Peak Current		
	Time (μ s)	Front Displacement (mm)	Approx. Centroid Displacement (mm)	Time (μ s)	Current (kA)	Centroid Displacement (μ m/min/max) (mm)
RIP306	50	76	68	168	82	215/225
RIP307	29	43	26	107	126	125/145

Inspection of the rails for these two RIP shots shows severe damage in a short zone corresponding to the short deviation power peak, in good agreement with the tabulated position. The 'narrow' power peaks can be seen in Figs. 30(a) and (b). The damage on the RIP 307 rails at this location is more severe than on the RIP 306 rails, as would be expected from the higher density for the former shot. Figure 31 illustrates the point.

Rail damage after the zone of peak energy-density (and power) is also more extensive on the RIP 307 rails than on the other set, consistent with higher energy density on the RIP 307 rails out to the peak-current zone at least. Figure 31 again illustrates the point. The figure shows broad bands of damage, due to severe surface melting, extending for at least 100 mm along the rails of both shots. Some of this damage is similar to that described previously [5] for static-start shots.

For the RIP 306 shot (and the other shots in its group) the broad, intense type of damage comes to an end before the location of peak current. In this region the damage is variable and difficult to define, and suggests that a transitional damage state is involved. For the RIP 307 shot (and the other shots in its group) the intense damage extends beyond the peak current region. As for the RIP 303, 305 and 306 shots, damage is then highly variable. Such shot-to-shot variability can be seen in the full-length prints of the rails (Fig. 9). Duration of the variable damage is different for each shot in both RIP groups. Nevertheless, for both groups the damage can be seen to generally decrease with displacement along the bore, once the peak power (energy density) zone has been passed.

It therefore appears for all the RIP shots (303 to 311) for approximately the first half of the firing, that the variation of rail damage with displacement correlates with rail energy-density. It should be pointed out, however, that the correlation applies equally well to armature power, though it would be difficult to argue for the use of armature power alone as a damage predictor. Objective damage indicators would be required to make the discrimination.

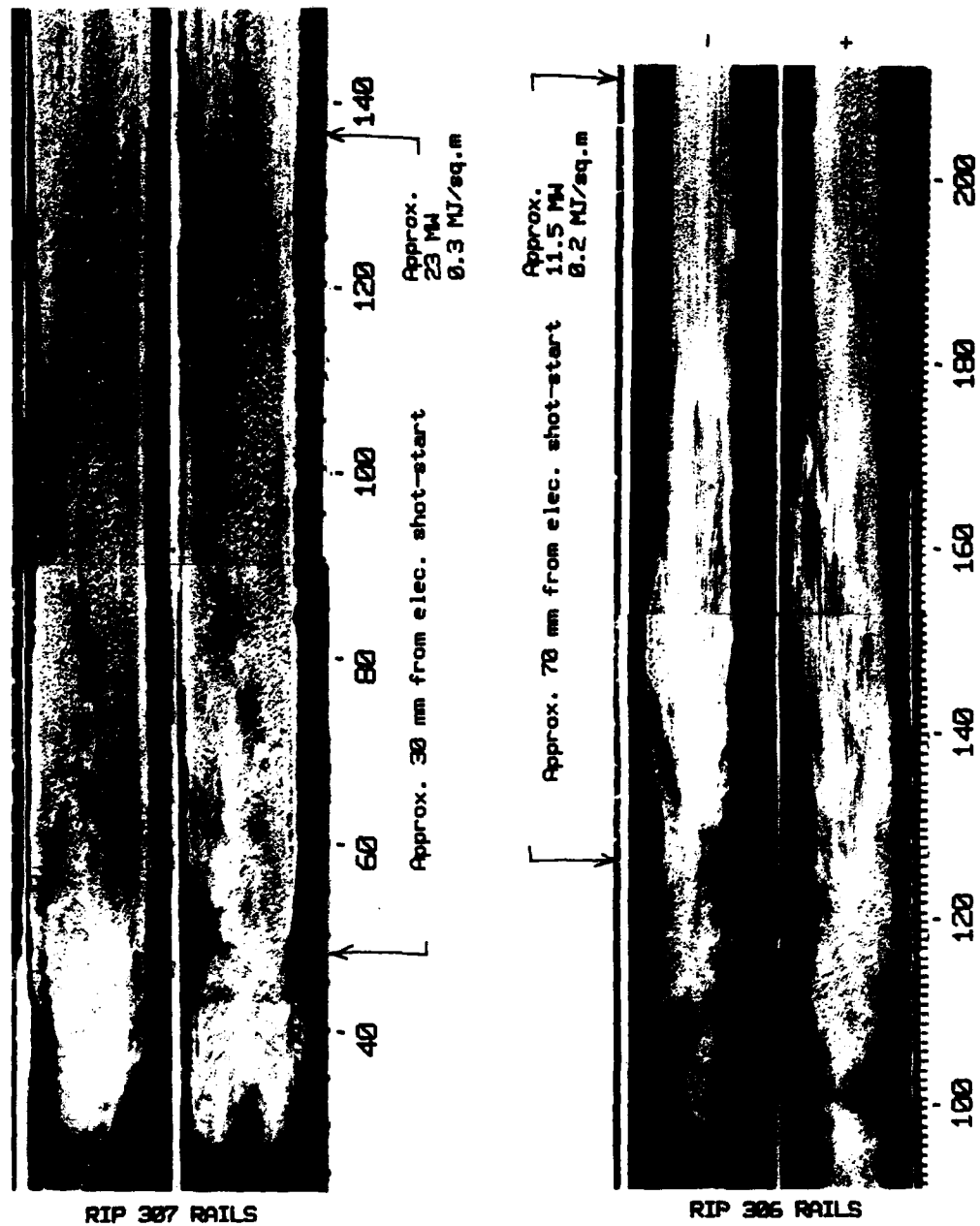


FIGURE 31 Examples of rail damage at the time of peak armature power, and for a short region subsequently. This damage was typical for shots initiated with aluminium foil. Rails are shown folded out. Rail polarity is marked at the muzzle end. Scale is in mm and is breech-end referenced.

Leaving consideration of the second half of the firing cycle for the time being, consider now the shots RIPAL 2 and RIPLAM which were initiated with copper foil on polyester. Referring to the table of energy densities, it can be seen that for these two shots A either remains approximately constant during shot life, or increases slightly from the peak-power to the peak-current phases. If the proposition is true that rail damage is dominated by energy-density considerations, then rail damage should reflect this, i.e. damage should be either relatively uniform for the whole shot length, or show damage increasing progressively with displacement to a relatively constant level (relative to the peak-power phase). As before, to assess if this is so, armature displacement data are required.

Armature Displacement Data for RIPAL 2 and RIPLAM

Shot	Firing Phase				
	Peak Power		Peak Current		
	Time (μ s)	Approx. Centroid Displacement (mm)	Time (μ s)	Current (kA)	Approx. Centroid Displacement min/max (mm)
RIPAL 2	35	40 to 43	184	82	250/260
RIPLAM	35	39 to 44	184	82	255/270

Study of the RIPAL 2 rails in conjunction with the above data shows significant departure from prediction, viz. there is a relatively long zone of damage between the locations of peak-power and peak-current, which is significantly more severe than at either these locations or near shot-out. This is true also for other firings which used copper foils. (For both RIPAL shots, the zone of increased damage covers approximately the region between the first and second inserts. Figures 34(a to d) show the two ends of this region. Note that for the study covered in this Section, interest is confined to the copper surfaces, as copper is the rail material common to all shots).

Interpretation of the damage to the RIPLAM rails is not simple. Non-uniform current distribution across the face of the rails may have caused localized intensification of damage. Nevertheless, the visual impression here, as for the other shot, is that the overall damage in a region between peak-power and peak-current is more intense than elsewhere. This region of the RIPLAM rails is shown in Fig. 32(a).

The conclusion for the copper-foil shots is that, in the firing phase from peak-power to peak-current, observable rail damage does not correlate with energy density. This conflicts with the initial conclusion for the aluminium-foil RIP shots at the same phase of firing.

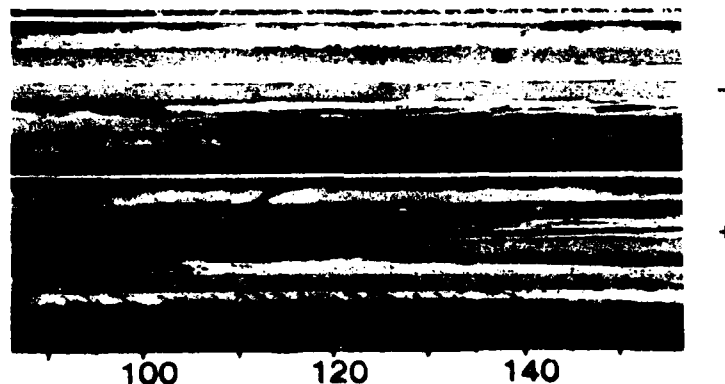


FIGURE 32(a) RIPLAM rail damage in the region of increased damage following the maximum armature power phase. Rails shown folded out. Rail polarity marked at muzzle end. Scale in mm referenced to breech end.

Two more rail damage general observations help to clarify whether the original proposition is true or not. They are firstly that for a given energy density there is great variability of damage both within a shot, and shot to shot. For example, for shots RIPAL 1 and 2 the positive rail suffered more damage than the negative rail in the phase after peak-power*. Further, the damage did not extend across the full bore height. This effect can be seen in Fig. 32(b).

* The phenomenon of increased positive electrode damage is not new [12], although it was not noticeable in any of the other firings in the reported series. However, it was noted for all firings of an earlier MRL experiment (ERGS-1M) [16,17].

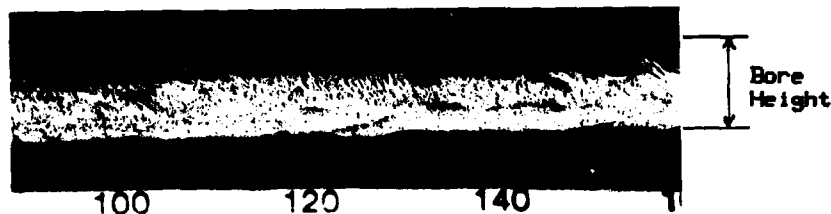


FIGURE 32(b) Damage to the positive rails of RIPAL 1 (shown) and RIPAL 2 is in the form of pitting, and significantly less than the full height of the bore. Scale in mm is breech referenced.

Secondly there is considerable contrast between the appearance of surface damage in early-to-mid shot life and the arc-track damage of late shot-life, sometimes at similar energy densities. Mid- to late-life arc tracks have been observed for all firings of both aluminium-foil and copper-foil shots. Thus damage not only varies in degree, but also in nature along the length of the bore.

These two pieces of evidence, combined with the evidence of damage variability in general, represent a strong case against the proposition that early damage correlates simply with energy density at the rail surface. However, the correlation evident for the aluminium-foil shots in the 'melt-damage' early phase is not easily dismissed. It may be that there is some energy density threshold below which other processes interfere or play an equal role in determining rail damage effects. In this matter it is interesting to note that, for all shots, rail energy density at the stage of damage transition to arc-tracks falls into a reasonably small range of values around 0.2 MJ/m^2 . The table below summarizes this data.

An estimate of armature parameter values during
damage transition from obvious surface melting
to arc-tracks

Shot/s	Centroid Displacement (mm)	Armature Power (MW)	Energy Density (MJ/m ²)
RIP 305/6	200	11.8	.18
RIP 307/10	220	17.4	.21
RIPAL 2	230	11.6	.17
SUBAC 4			
Positive rail	150	13.4	.22
Negative rail	250	12.3	.17

For both foil groups, variability of damage in early to mid life, and variability in the transition to arc-tracks appears to be governed more by processes associated with the foil 'explosion', plasma development, and plasma fluid stability than by the apparent level of the rail surface energy-density.

4.4.2 The Plasma Initiating Foil

As indicated in Sections 4.1.2 and 4.1.3, there is convincing evidence that the peak in the plasma armature voltage corresponds to the transition from foil vapourization to significant ionization. Aluminium needs approximately twice as much energy per unit mass as copper to reach this state. Power plots reflect these different energy requirements. Power differences for similar firings using different metals can readily be seen in the whole-of-life plots of Fig. 30 for RIP 306, RIPAL 2, and RIPLAM. Although the mass of the RIPAL 2 and RIPLAM foils was appreciably less than that for RIP 306, the peak power for these two shots was much less. The expanded early-life plots of Fig. 33 show more detail in this important plasma development phase. Such differences are reflected in early-life damage, as discussed in the previous Section, and as elaborated below:

(i) A unique pattern of damage near 'peak-power' was evident on the rails of the aluminium foil shots. This is evident in Fig. 31 in the few centimeters at the left-hand-side of the photographs. It probably corresponds to the greatly increased energy density during the narrow power peak.

(ii) The rails for shots using copper foils seemed to be characterized by more variable and pitted damage than their aluminium-foil counterparts during plasma development. That there would be differences between the rail sets other than in the immediate vicinity of peak power might be expected from a further inspection of the energy plots. Although the copper-foil fully vapourizes with lower energy than the aluminium foil, the rate of energy

expenditure is greater in the copper-foil at this time, e.g. at 35 μ s (peak power for the copper foil) energy expended was 225 J, but for the aluminium foil this figure was only 100 J.

(iii) A feature of aluminium foils was the alloying of aluminium with copper. The alloying was visible as gold coloured patches on the rails. One explanation for the alloying is that aluminium vapour (at about 3000 K) condensed from the plasma onto the rail surface, which was at melting temperature (about 1400 K). An alternative explanation is that the alloying took place within the plasma, which contained both aluminium and copper. Copper foils, of course, could not reveal such interactions. One thing is clear, however, and that is that the initial appearance of the alloy effect on the rails (sometimes called 'plate-out') is associated with the vapour state of the foil, and not its molten state. The aluminium foil was in its molten state about 40 nm before evidence of plate-out.

(iv) The maximum-temperature history of the armature from electric-shot-start to the time of the muzzle voltage peak (foil fully vapourized) is well defined, as the energy history, and melting and boiling points are known. Likewise, the temperature-displacement profile is fairly well defined, as the foil displacement-time profile is known within reasonable limits.

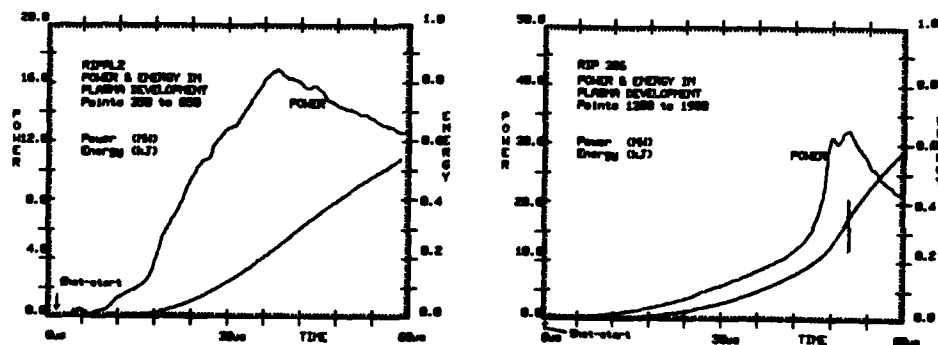


FIGURE 33 Power and energy histories for (a) a copper-foil shot (RIPAL 2) and (b) an aluminium-foil shot (RIP 306) during plasma initiation

4.4.3 I^2R Contribution (Joule Heating)

Rail current may contribute to damage by heating the rail surface, an effect sometimes referred to as joule heating. The joule heating will be greatest where both the current is high and the surface resistivity is high. The surface resistivity will be highest in the region of the plasma because of the heating as the plasma passes by. (Resistivity increases by an order of magnitude at the melting temperature of metals, as compared with room temperature). However it is usually supposed that, in a practical gun, I^2R rail heating, and hence related rail damage, is insignificant compared with heating and damage due to the arc.

For all reported shots, the worst surface damage occurred either in the vicinity of peak armature power, or in a band of some 100 mm between power peak and current peak, but generally decreased as the plasma moved further along the bore. There appeared to be no particular pattern of deviation from the general reduction of surface damage through the broad peak current phase, i.e. I^2R damage did not appear to be significant compared with that due to armature power.

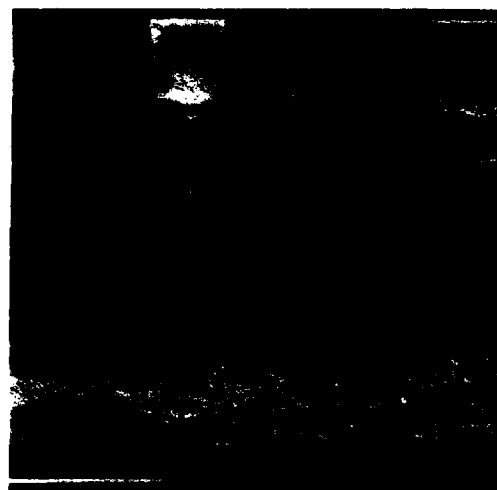
Because of the variability of damage and lack of metallurgical data it is not possible to make a definite judgement on the effects of I^2R heating. However, the conclusion on the available evidence is that the contribution is at most a minor one.

4.4.4 Rail Material; the RIPAL Experiments

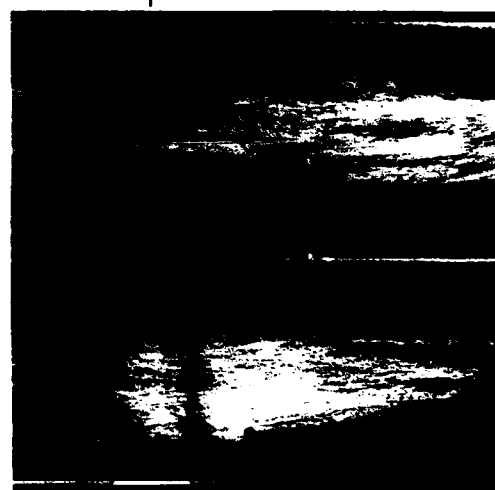
This section examines the experimental information from the two RIPAL aluminium-insert firings, which were described in Section 2.4. Other relevant data may be found in Appendix 1. While the intention of the experiment was to explore transport mechanisms across the plasma, rail damage effects in the vicinity of the inserts were found to be of interest in their own right. Because of the variability of damage, records of all eight inserts are presented (Fig 34), together with detailed observations. Ablation measurements at two sites are also discussed. In the figure, the rails are shown folded out; adjacent edges were at the bore lower surface. The lower rail is positive, and the direction of motion is to the right.

Some general observations on surface damage can be made as follows:

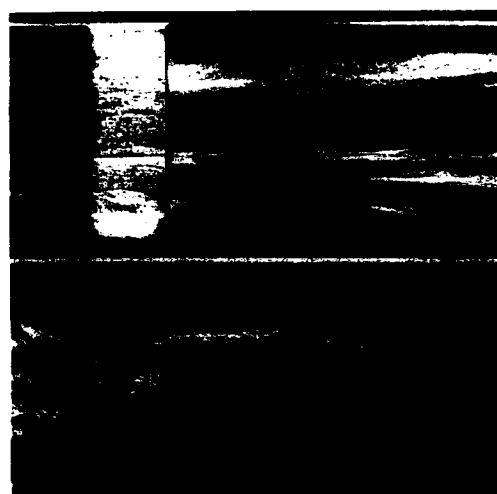
- (i) All inserts suffered more severe damage than the adjacent copper rail.
- (ii) Much of the material removed from each insert was deposited immediately 'downstream' on the same rail.
- (iii) The area of insert-damage was markedly greater for all inserts in RIPAL 2 than in RIPAL 1.
- (iv) Insert-damage appeared to be independent of rail polarity.



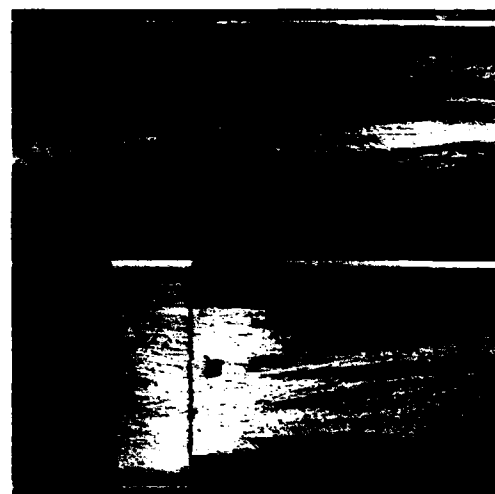
(a) RIPAL1 74mm



(c) RIPAL1 174mm

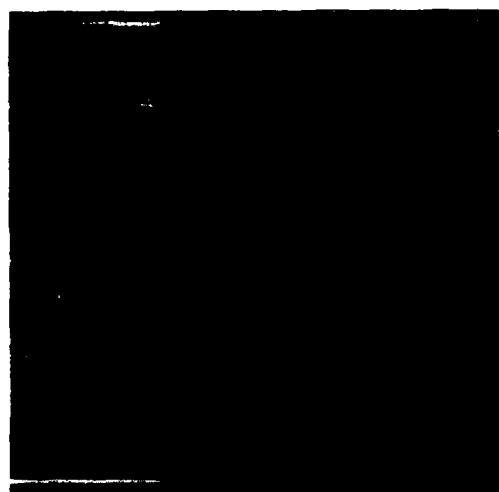


(b) RIPAL2 74mm

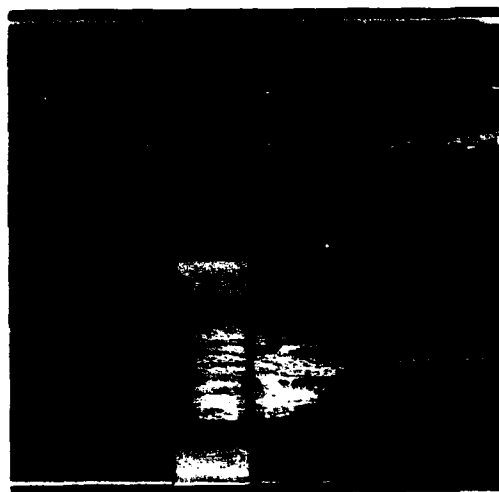


(d) RIPAL2 174mm

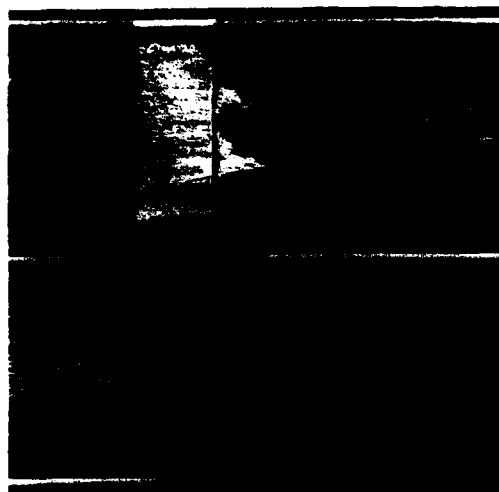
FIGURE 34 Rail damage in the vicinity of aluminium rail-inserts at 74 mm and 174 mm from the rail electrical connectors of RIPAL 1 (top) and RIPAL 2. Rails shown folded out. Upper rail is negative. Talysurf trace direction is marked.



(e) RIPAL1 274mm



(g) RIPAL1 374mm



(f) RIPAL2 274mm



(h) RIPAL2 374mm



FIGURE 34 Rail damage in the vicinity of aluminium inserts at 274 mm and 374 mm from the rail electrical connectors of RIPAL 1 and RIPAL 2 Talysurf trace direction is marked.
(contd)

Examination of the rails showed that molten aluminium swept downstream from each insert had mainly resolidified in a flaky layer. Alloying was evident downstream from the 74 mm sites (Fig. 34(a) and (b)), and beneath and near the edges of some flakes, which had lifted slightly from the rail surface. It could be expected that similar effects would occur with all inserts. The scavenging appears to have mainly occurred immediately after the passage of the main body of the plasma, while the damaged material is still molten.

There is some possibility that the plastic pyramids used for protecting the foil (as explained in Section 3.4) could have interfered with the insert surfaces. Smearing of molten copper surface (evident in Fig 34 (c) and (d)) could perhaps be taken as evidence in support of this case. However, it seems too much of a coincidence that the smear locations would be almost identical. The similarity of the insert damage which was observed within each shot would also lead one to discount this possibility.

Further downstream, aluminium is only evident (at X8) on the arc tracks (c, d, e), and can be seen 3 to 5 cm downstream, with traces to 10 cm, as if aluminium vapour or droplets had been trapped on touching molten arc tracks.

Insert damage appeared to be of two types; firstly, scouring aligned with arc-tracks on both sides of inserts (henceforth referred to as in-and-out-track's), and secondly, general melting. In the RIPAL 2 shot, surface melting outside the obvious band of arc-track scours had generally extended insert damage to the upper and lower bore surfaces, producing the effect, on this shot only, of full height damage to the inserts. Some edge-melted material had been forced beneath the body edges, and condensed in a flaky layer (Fig. 34(d) and (f) particularly). Discussion of insert damage will be considered later in this Section.

Fine copper condensate was evident (at X8) on all inserts of the RIPAL 2 rails, and at least some of the RIPAL 1 rail inserts. This could only have occurred after the molten aluminium had been swept out. The particles or droplets appeared fairly evenly distributed, suggesting a fine cloud sweeping along behind the plasma. This possibility, however, would appear to be countered by the lack of similar evidence on the surface of the downstream aluminium flake, unless this had already dropped sufficiently in temperature (through contact with the copper) that it was not as 'sticky' as the aluminium insert.

The quality of electrical connection between the inserts and the rails must be considered as a potential factor in damage to the inserts and adjacent rail edges. If poor connections existed, this might explain the damage difference between inserts and rails. Erosion of adjacent insert and rail edges, and molten material between surface edges was evident at most, if not all, sites. However, no pattern emerges which might lend support for an argument that the difference between the two shots, or between inserts and rails is supplied by a consistent difference in electrical connection. Furthermore, the good correspondence between the band of in-and-out arc-tracks and the width of insert damage (note (g) particularly) reinforced the view

that the insert damage was not dominated by insert-to-rail connection influences.

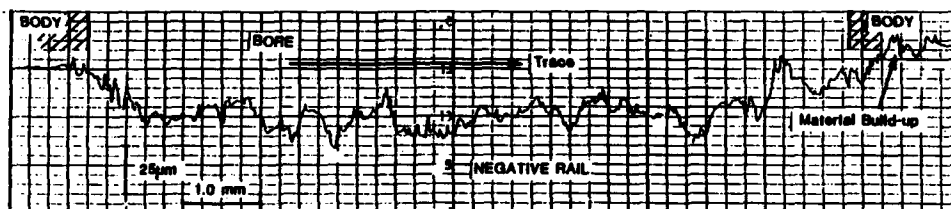
It seems unlikely that the copper 'condensate' on the inserts would have come from boiling metal at an upstream edge of an insert, as such material would, most likely, have been highly alloyed. It is therefore possible that a cloud of copper vapour was carried along in the 'cold' plasma tail.

Some evidence relating to material transport from rail to rail was obtained from the experiments although no detailed metallurgical studies were done. The positive rails of both shots showed traces of alloy in the 74 mm to 174 mm damage band. This was the only region where there was no upstream insert on the same rail, the insert being on the negative rail. The material could only have come from the upstream negative-rail insert. Hence it must be concluded, at least for this experimental set-up, that material was transported from the negative rail to the positive rail. Because the 74 mm-insert was in the negative rail for both firings, no evidence was produced on the possibility of a reverse flow from the positive rail to the negative.

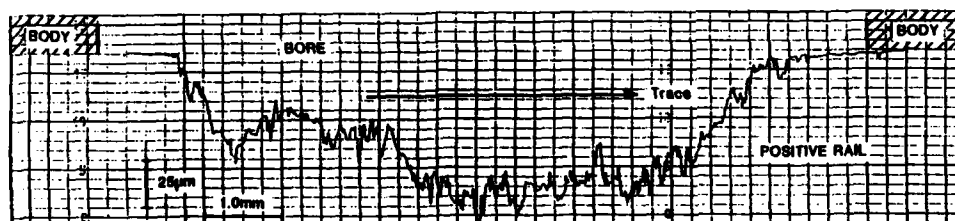
The mechanism of alloying is open to conjecture. The alloying may have occurred in the plasma, mixing with ablated copper, to be eventually dumped out of the plasma, or by way of aluminium vapour swept along behind the plasma being deposited (in part) on the hot positive rail.

Aluminium-copper alloy was also to be seen on a copper smear opposite and downstream from the RIPAL 2 174 mm insert (Fig. 34(d)). However, the presence of an upstream insert also makes this inconclusive.

Particular comment is required on damage to the inserts and the adjacent rails. To obtain an objective measure of insert damage, a single profile measurement was made of two of the inserts, one with 'narrow' damage (RIPAL 1 at 174 mm, Fig. 34(c)), and the other 'broad' (RIPAL 2 at 374 mm, Fig. 34(h)). The power histories and shot parameters of these two firings were similar, enabling some direct damage comparisons to be made. A single slice across the middle of the insert was taken to be a reasonable average. (Damage depth was generally greater at the downstream edge). The contours are shown in Fig. 35. Contour locations are also marked in Fig. 34. A Talysurf instrument was used to obtain surface contours. This has a full-scale-range of 0.1 mm. The diamond stylus has a tip radius of $2.5 \mu\text{m}$ on a 90° cone and has a 50 mg tip load.



(a) Talysurf trace for RIPAL 1 insert at the 174 mm positive rail site. This is an example of the narrower and deeper insert-damage.



(b) Talysurf composite trace for RIPAL 2 insert at the 374 mm positive rail site. This is an example of the broad insert-damage described.

FIGURE 35 Damage profiles across two RIPAL rail inserts. Trace orientations relative to the rail photographs of Figure 34 are shown.

The contrast between the two contours, and hence between the two damaged inserts, can readily be seen. The table below summarizes analysis of the insert data.

Insert surface energy-density and mass losses

Shot	Insert Site (mm)	Approximate Mass Loss (mg)	Energy to Melt (J)(1)	Energy Available (J)
RIPAL 1	174	5.2	5.7	8.5 to 9.5
RIPAL 2	374	3.1	3.4	8.0

(1) assuming all energy used in melting only

On the basis of the information in this table, and on observation of the insert sites, three points can be made.

Firstly, if the same influences were operating on the adjacent copper surfaces as on the insert, it would be expected that significant mass loss would be evident on the copper rails also, i.e. only 1.7 times less by volume than for the inserts. As this is not the case, there must be other factors besides surface energy density which govern material loss. It seems that even the drop in the thermal conductivity of aluminium from the solid to the molten state by a factor of approximately 2 would not account for the difference in damage relative to copper.

As the electrical integrity of the inserts in the rails appears to have been satisfactory (discussed earlier in this Section), some other process must be acting on the rail surface. On the adjacent copper rail surface, the dominant surface-damage effect has been produced by arc-root (or arc track) activity. As there appears to be very good correspondence between the damage markings on the copper due to the insert in-and-out arc-tracks, and the damage markings on the inserts, it seems likely that the difference in damage on the two metals has been caused by a difference in the arc-track processes at the two metal surfaces. Arc theory might provide an explanation, but such an approach has not yet been attempted.

Secondly, from the table, 43% to 60% of available energy has been expended in melting the inserts. Assuming that this figure is valid, only 50% of the plasma energy would be available for raising the molten aluminium to higher states. It seems likely then that only a small percentage of the molten metal would actually reach first-level ionization (review the energy table in Section 4.4.2). This represents a marked departure from a prediction based on the Parker-Parsons (henceforth referred to as P-P) ablation model

[11]*. The P-P model predicts an insert mass loss of only 0.25 mg, all of which would be first-level ionized. This is equivalent to removal of a skin layer 2 μ m thick. The prediction for copper in the same environment is approximately 1 μ m skin-thickness removed. On reviewing copper surfaces unmarked by arc-tracks, it seems possible that copper loss through thermal radiation has been of such a low order. Hence, applicability of the P-P model may depend on the metal used.

Thirdly, the differences in insert damage between the two RIPAL shots probably reflect real differences between the two plasma armatures. The conspicuous difference is the width of the damage to the inserts. (Refer Figs. 34(c) to (h)). It should be noted that both injection and exit velocities were almost identical for the two shots. RIPAL 1, with the narrower damage, used a 12Z heavier initiating foil, and a 6.4Z heavier projectile. From the B-dot data in Appendix 1, it can be seen that the armature length of RIPAL 1 was appreciably shorter than that of RIPAL 2, particularly for the first 150 mm. The relationship between these shot parameters is not understood. An experimental study of foil type and mass versus shot performance has been reported [3].

Finally, on the subject of ablation, it should be noted that when an exposed molten surface is in a high velocity gas stream, higher rates of mass-ablation are to be expected than one would expect from the energy balance equations for the static condition [15]. The railgun plasma environment has some similarity to this situation.

4.4.5 Rail Construction; the 'RIPLAM' Experiment

The rails for the RIPLAM experiment were described earlier (Section 2.4). The reader is also referred to the earlier Section 4.4.1 and Figs. 32 and 33 for comment on rail damage in the early stages of electric-shot-life. The subjective judgement was made that rail damage in early-shot-life was no worse for the RIPLAM rail set, with its reduced copper area, than for full-width rails.

Contour measurements of the rails were made at distances of 210 mm and 375 mm from the breech end of the rails after the shot. Unfortunately no comparative pre-shot measurements were made. Fig. 36 shows the contour traces for both rails, and a photograph of the rails about the 375 mm band.

* In the P-P model, at sufficiently high energy levels, surface evaporation is virtually instantaneous. All the evaporated material is ionized before any more melting occurs, as the vapour is opaque to thermal radiation.

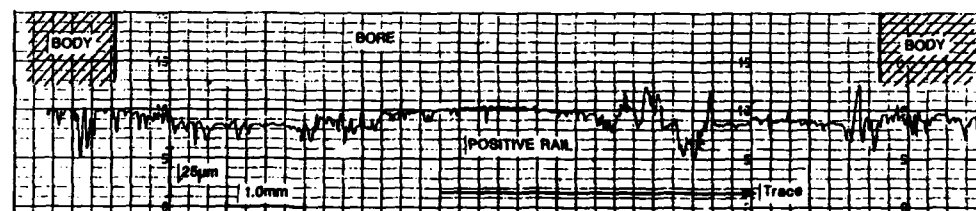
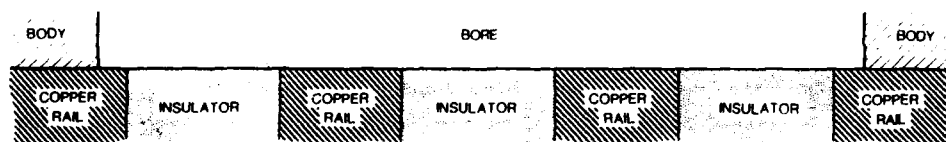
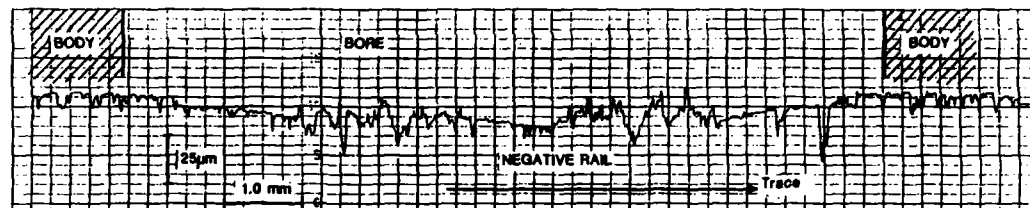


FIGURE 36 (a) Talysurf composite contour traces for RIPLAM rails at 210 nm (referenced to rail breach-end). The central drawing marks the location of the insulating channels.

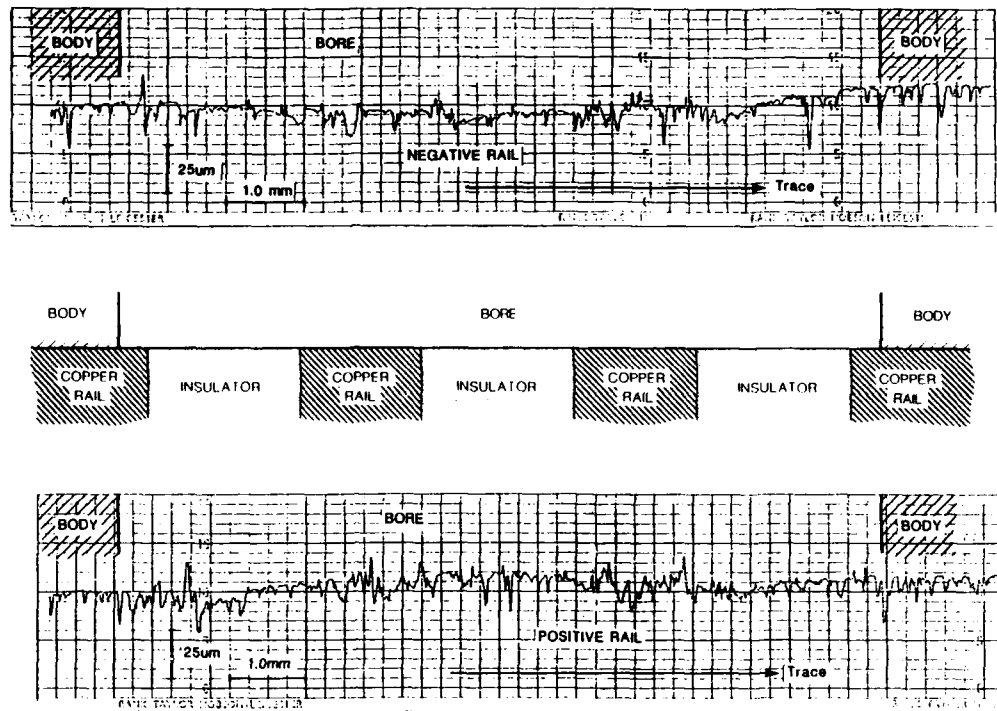


FIGURE 36 (b) Talysurf composite traces for the RIPLAM rails at 375 mm (referenced to rail breech-end).

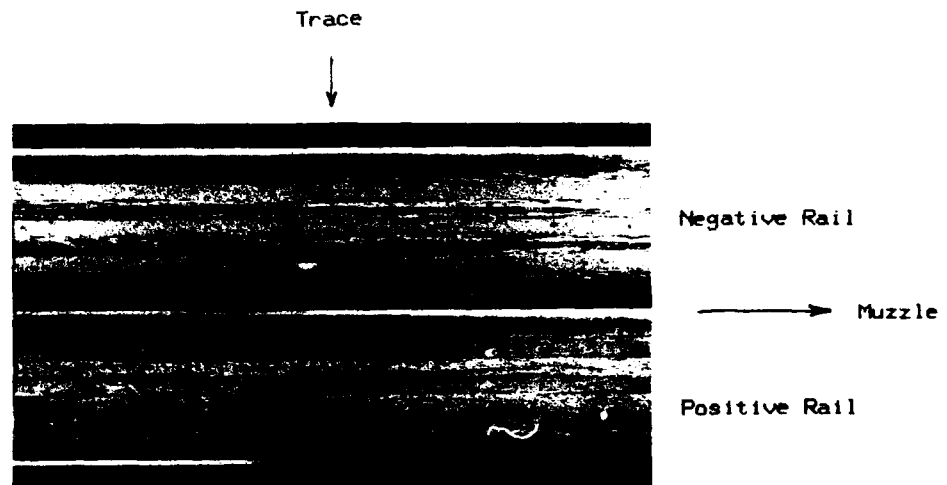


FIGURE 36 (c) The RIPLAM rails near 375 mm with the rails folded out. Talysurf trace direction is marked.

The distinctive wandering arc-track patterns usually seen when general damage was not dominant were not seen on this rail set, as arcs were constrained to the copper strips until they were extinguished. General comments follow:-

- (i) In terms of surface-damage, there is no clear demarcation of insulator and conductor boundaries (Fig. 36(b) particularly). This is not what was expected, as outlined in Section 2.4.
- (ii) Arc-tracks are evident, Fig. 36(a) particularly, as distinguished by damage peaks, i.e. by large localized contour deviations.
- (iii) At 375 mm, fine damage extends the full width of the exposed rail surface, (Fig. 36(b) and (c)) copper and insulate alike.
- (iv) The peak-to-peak damage (36 μ m), is approximately the same at 210 mm and 375 mm, the limits being set by the craters and pits of distinct arc locations (tracks).
- (v) At 210 mm particularly (Fig. 36(a)), the contour indicates that the top surface of the insulators are at different heights. At both sites, the central insulation of the positive rail is higher than the edge insulators, and on the negative rail the reverse effect appears to be true. This unevenness probably reflects deficiencies in rail preparation rather than differences in erosion rates.

As the original rail condition was not recorded, no judgement can be passed on the uneven insulator height. Apart from the appearance of a few blow-holes, and loss of a few short pieces at the very start of the filling, the rail insulators survived well. This loss may have been aggravated by the heating required to soft-solder heavy connectors to the rails. The evidence indicates that these pieces broke away after the passage of shot, and had no effect on electrical operation.

The reduction of surface area available for current flow into the armature appears not to have increased surface damage of the copper.

4.4.6 Arc-Track Damage Evidence

Apart from the points already made about arc-track damage, additional information was available from a scrutiny of the tracks. As noted elsewhere, [5.8] arc-track evidence points to the plasma-rail interface being a complex region. Arc track patterns appear to be unpredictable in relation to number, direction, and aggregation. The transition from general surface damage to arc-track damage is variable from shot to shot, and rail to rail. For example, for SUBAC 4, arc tracks are evident at about 120 mm on the positive rail, but do not appear on the negative rail to any great extent for a further 100 mm. Figs. 34 (d) to (h) provide further examples of the variability of arc-track behaviour. Further evidence is presented in this Section of specific rail damage effects, with objective measurement of rail surface contours.

Figure 37 presents data from SUBAC 4 for the positions 185 mm and 375 mm relative to the breech end of the rails. The difference between positive and negative rail damage, and the change which occurs over a distance of 20 cm is of particular note.

As noted for the RIPLAM shots the classic pits and peaks of the arc-tracks dominate the rail damage, giving the same peak-to-peak damage range of 25 μ m to 35 μ m as on other rails measured, including the RIPLAM rails.

It is interesting to note that the 185 mm (breech-referenced) location was in the region which produced dark areas on the streak photo. It was demonstrated (Section 4.3.1) that this effect did not correspond to a longitudinal plasma current distribution anomaly. Reference to Figs. 37(a) and (b) does suggest that the plasma current was asymmetrically distributed across the rail faces, but it is unclear how this may have modified optical transmission, although a possible mechanism is suggested in Section 4.4.7.

Two firings, namely RIP 303 and 305, are of special interest in that rail damage was notably different from the other shot (RIP 306) of that group, and from all other lower-power shots. For both shots, the number of distinct arc-tracks on one or both rails after 20 cm from electrical start was relatively small. Fig. 38(a) shows a short length of the RIP 305 rails in this unusual region. Fig. 38(b) shows a surface contour across each of the rails at 310 mm (breech-rail-end referenced). Fig. 38(c) shows contours of the rail damage at an earlier rail position (175 mm) for comparison of damage. The damage at 175 mm is of the broad generalized type with evidence of alloying.

The negative rail contour (Fig. 38(b)) shows four deep pits grouped in two pairs, with very little damage to the remainder of the rail surface. Only the two central pits are the result of arc action, the others being scratches. The positive-rail damage is more general in nature, but is concentrated in bands centered on two arc tracks. (The slight angle on these two traces was due to a Talysurf alignment error. The bow in two traces can be taken as post-shot rail distortion. Extreme surface heating causes metallurgical changes and introduces stresses which bend the rails. It is reasonable to expect that bending would occur transversely and longitudinally. The effect has been reported [5,16]). Referring to the negative rail in Fig 38(a), it should be noted that, considering a slice across the rail, the total area of damage in the vicinity of 270 mm seems to greatly exceed that around 290 mm. Two interpretations are that either the plasma current distribution changed, or the conduction mechanisms changed.

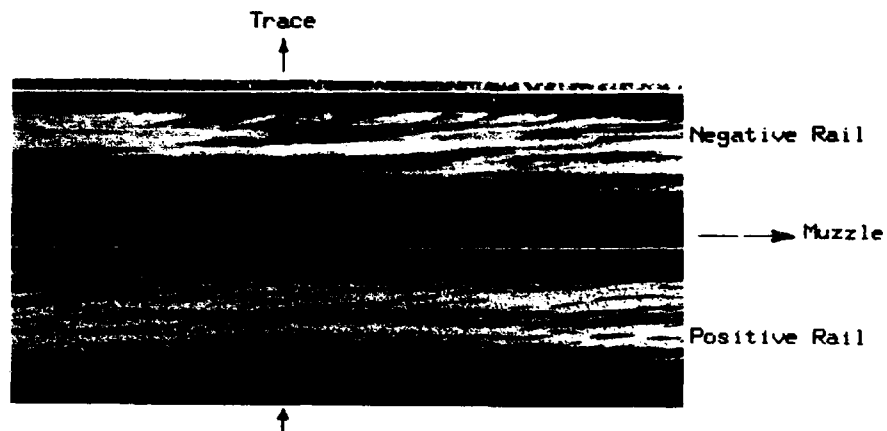


FIGURE 37 (a) The SUBAC 4 rails near 185 mm with the rails folded out. Talysurf trace directions are marked. Distance is referenced to the rail breech-end.

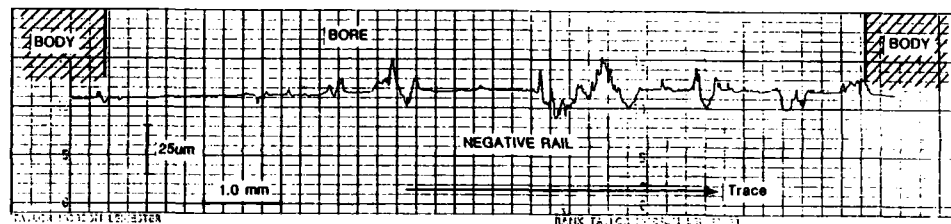


FIGURE 37 (b) Contour trace for the negative rail at 185 mm.

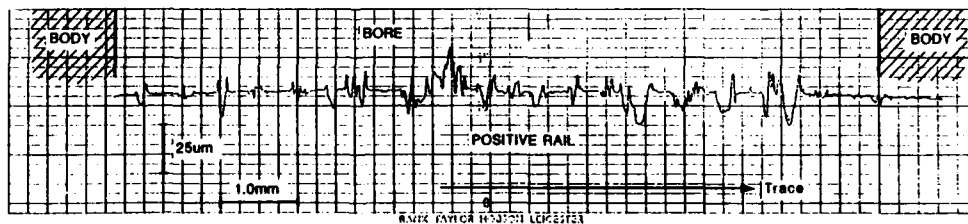


FIGURE 37 (c) Contour trace for the positive rail at 185 mm

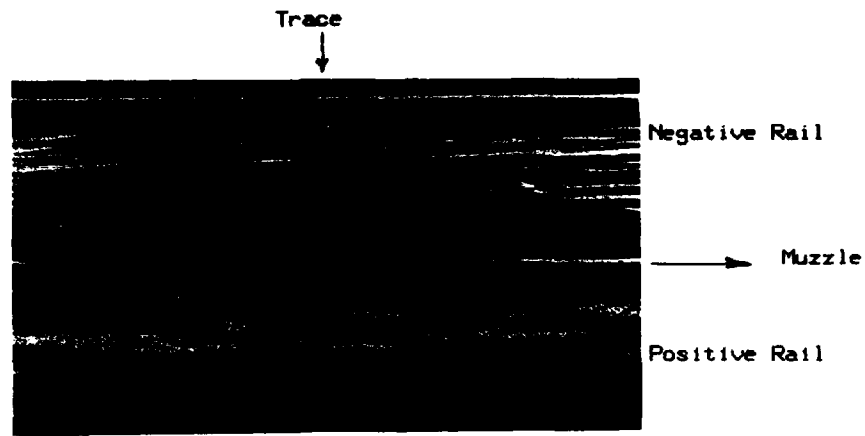


FIGURE 37 (d) The SUBAC4 rails near 375 mm with the rails folded out. Talysurf trace directions are marked. Distance is referenced to the rail breech-end.

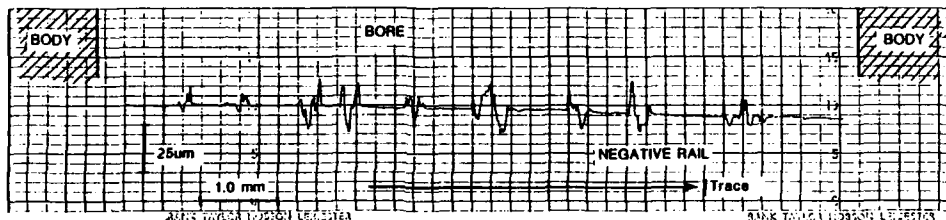


FIGURE 37 (e) Contour trace for the negative rail at 375 mm.

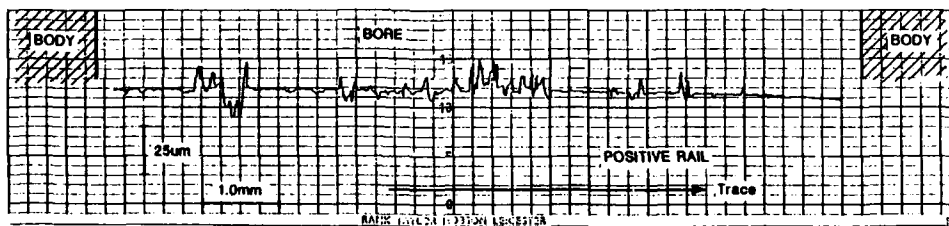


FIGURE 37 (f) Contour trace for the positive rail at 375 mm.

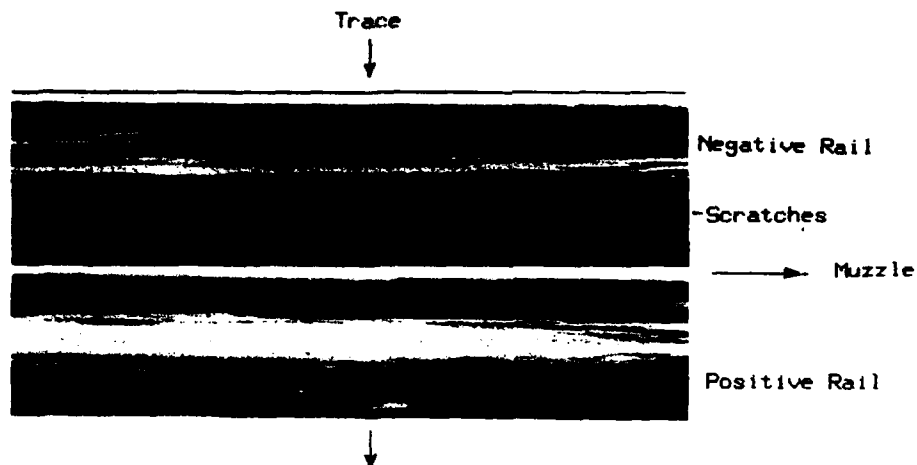


FIGURE 38 (a) The RIP 305 rails near 310 mm with the rails folded cut. Talysurf trace directions are marked. Distance is referenced to the rail breech-end.

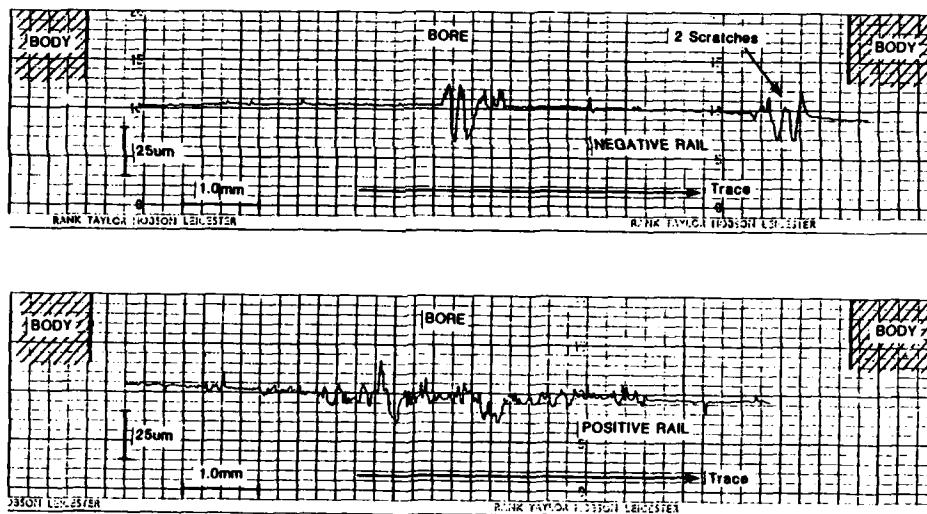


FIGURE 38 (b) Contour traces for the positive and negative rails at 310 mm. The double pit at the right-hand end of the negative-rail trace corresponds to two scratches.

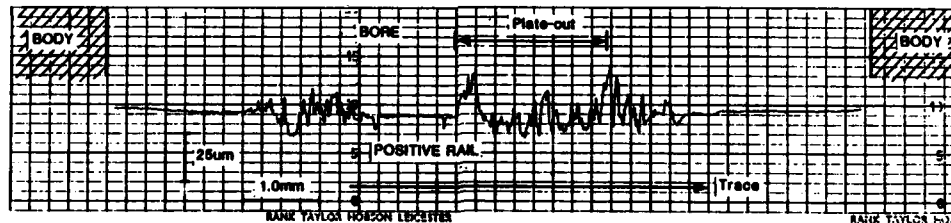
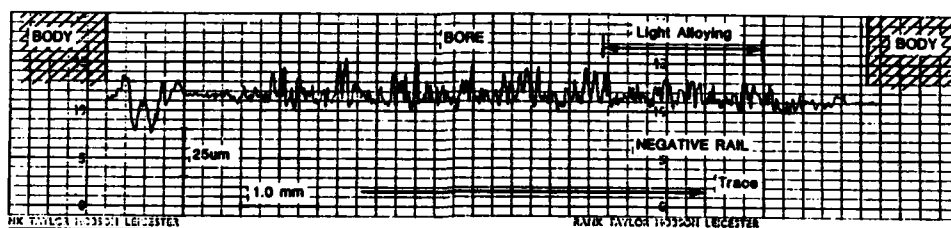


FIGURE 38 (c) Talysurf contour traces for the RIP 305 rails at 175 mm. Distance is referenced to the rail breech-end. This is a region of general surface damage.

The rail damage contours from the 175 mm location further emphasize rail-to-rail damage differences. Significant arc-track positions can be identified on the negative rail, but both at 175 mm and at 310 mm, the arc-track 'crater-and-lip' patterns are absent from the positive rail. General surface melting, as evidenced by broad damage, may have reduced the peak-to-peak damage of the track patterns. Considering the damage to the negative rail at 175 mm, it is difficult to imagine that the same arc caused the two-track damage at 310 mm. Either other tracks were obliterated, or other conduction processes were operative in the early phase. The earlier SUBAC 4 records are similar as shown in Fig. 37.

In attempting to explain the different pattern of arc-track-damage for shots RIP 303/5, distinguishing features of the two shots need to be considered. Although no single feature emerges, RIP 303/5 were the only low-power shots which were initiated with aluminium foil, and had also experienced non-electric firings prior to the recorded shots. RIP 303 experienced two prior shots, and RIP 305 one.

The results from other firings with aluminium present in the plasma have shown clearly that aluminium alone is not the crucial factor. Conditioning of the bore, such as polishing by a projectile pushed only by propelling gases, could conceivably affect arc-surface interaction.

It is known that arc-spot movement is different on smooth and rough surfaces [18]. Arc-spot movement to a new site can only occur when the site is capable of supplying the vapour to support the plasma [18]. In simple terms, this seems to occur by the melting of high-spots (micro-tips) for rough surfaces, and by heating of immediately local spots by bending of the arc-root for smooth surfaces [18]. If a smooth-surface rail is assumed, there may be a tendency for the arc-roots to lag a plasma-front bowed ahead by $J \times B$ forces. This could provide the necessary localized surface pre-heating to enable an arc spot to move or jump, more-or-less in a straight-line, in the bore direction, as against the more random and angled tracks usually seen as an arc-root follows a trail of vaporizing micro-tips.

Other experimental evidence relates to the effect of bore polishing. RIP 310 (aluminium foil) experienced a single preliminary shot, and SUBAC 2 (copper foil) experienced two. One rail only of each of these firings was atypical. The negative rail for RIP 310, and the positive rail for SUBAC 2, showed unusually numerous arc-tracks in the later shot phase. However, neither rail of either shot showed the reduced arc-track pattern observed on the two lower-power RIP shots. Hence, the evidence that surface finish influenced the arc-track damage in the rail-gun environment remains inconclusive.

There is evidence that, at the time the arc-track effects under discussion were being generated, the plasma current-distribution was abnormal. The B-dot record from a probe very close to the RIP 305 region of interest is shown in Fig. 39. The time-integral is included to establish confidence in the validity of the waveform. The waveform is unusual in both the raggedness of the first peak, and in the contrast of the smooth shorter

second peak. The waveform implies that the maximum current density of the plasma occurs slightly to the rear of the physical centre. A more typical plasma has its maximum current density significantly forward of the physical centre. Fig. 39(b) shows the corresponding and more typical B-dot record from RIP306. This observation does not assist explanation of the phenomenon, but confirms the behaviour as being anomalous. Reference to Appendix 1 on B-dot data for the 285 mm and 310 mm positions shows that unusually long plasma transit times were associated with the aluminium foil shots at this point in shot travel.

It might also be expected that surface oxidation of the copper rail, and oxidation distribution, would have some influence on plasma and arc-root behaviour. However the history of rail pairs between preparation and firings was not recorded, so a correlation cannot be attempted.

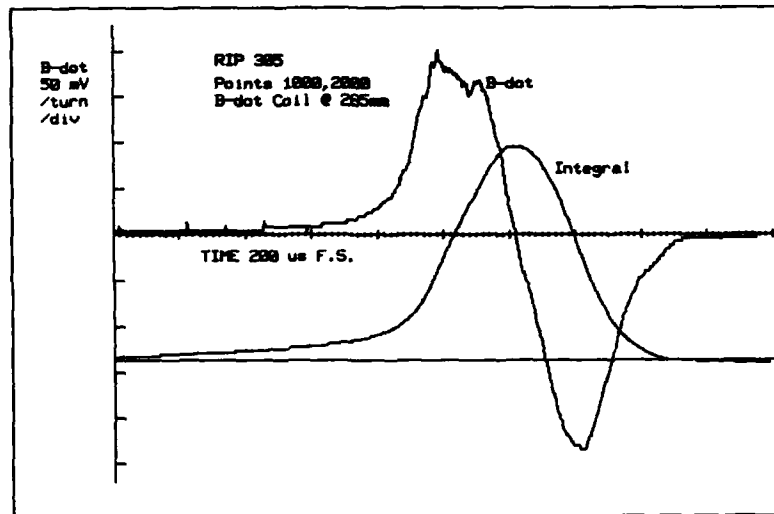
Three pieces of evidence, which bear on the nature of the railgun plasma in general, remain to be presented. The first two relate to turbulence. Fig. 40 shows a section of the rails from firing RIP 310.

Apart from showing damage differences at the two rails, which are in themselves significant, this sample provides clear evidence of turbulence in the current-carrying body of the plasma, as distinct from what might be happening in a 'cooler' tail. The pattern shows the presence of either 'cork screwing' of the whole plasma, or independent effects at the two rails.

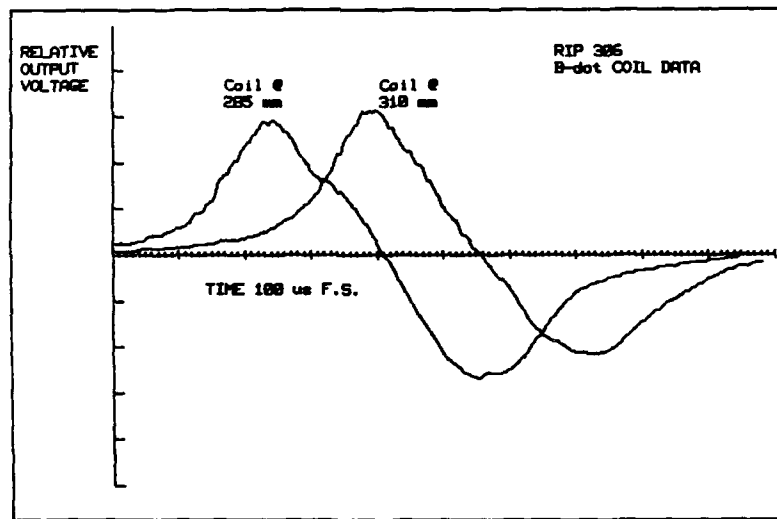
The second piece of evidence arises from a study of rails used in an earlier MRL experiment (ERGS-1M) [17], in which it was observed for a number of the firings that there was no definite position along the rails where melted (or broad) damage finished leaving just arc-track damage [16]. Instead, the damage zones alternated in 1 cm to 7 cm sections. This indicates that the damage mechanisms were also changing.

Finally, there is consideration of surface melting. Data are available from the same set of experiments (Shot 3 of ERGS-1M), which indicate that the minimum depth of surface melting for this shot was 20 μm (shot travel, 520 mm) [16]. For the RIP 305 shot, this scales to approximately 8 μm (minimum), i.e. equivalent to 0.7 mg/mm/rail melted. Note that the depth of the arc pits for RIP305 (Fig. 43(b)) is recorded as 15 μm , which is much deeper than the estimated melt depth. The fine surface finish between arc-tracks for the RIP 305 and SUBAC 4 negative rails (Figs 37(e) and 38(b)) should particularly be noted. Clearly rail damage can occur with very little surface evidence. No melt-thickness measurements were made on any of the rails from the firings reported, however.

Two further points need to be made. Firstly, a significant proportion (13%) of plasma energy is being expended in melting the rail surface. This must mean that a P-P based prediction of surface mass-ablation and subsequent ionization is too high. Secondly, it highlights the difficulty of making damage assessments and analyzing surface phenomena without supporting metallurgical analyses.



(a)



(b)

FIGURE 39 Pick-up coil waveforms for (a) RIP 305 coil at 285 mm; ragged first peak. The waveform at 310 mm was similar. (b) RIP 306 waveforms at the same locations are normal.

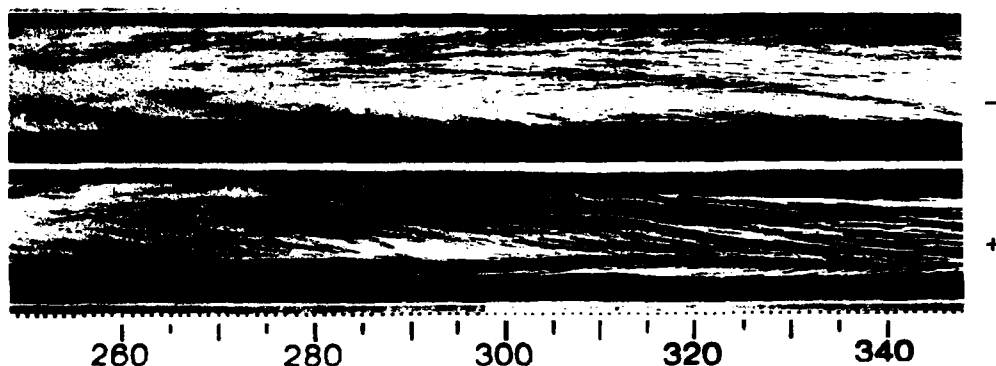


FIGURE 40 An example of evidence of plasma turbulence, RIP 310. Rails shown folded out. Rail polarity marked at muzzle end. Scale in mm is breech-end referenced.

4.4.7 Summary of Damage Data

The main points from the previous Sections are summarized below, together with some additional observations:

- (i) Increased rail damage occurred while the plasma initiation foil was in the metal-vapour-to-plasma transition. Because of the higher energy required to vapourize aluminium, aluminium foil caused more damage than a copper foil.
- (ii) Severe, early, positive-rail damage was observed on some copper-foil shots, but it was not observed on the aluminium foil shots reported here. However the damage has been noted in other experiments at MRL using aluminium foil for plasma initiation. The damage was thought to be the result of electron-bombardment effects.
- (iii) Arc-tracks were observed on all rails. Arc-tracks generated crater-and-lip damage, with both crater and lip measuring up to 15 μm on copper rails. Such peaks were observed to exceed the amplitude of

adjacent diffuse surface-damage. In some diffuse-damage bands there was no evidence of peaks or valleys that might be associated with arc tracks. It was therefore considered unlikely that diffuse damage consisted simply of a smearing or merging of the damage of numerous arc tracks.

- (iv) Aluminium surfaces suffered particularly severe damage relative to that for copper in the same environment, and this was thought to be due to the arc-roots affecting the two surfaces differently.
- (v) The process of formation of a layer of (resolidified) aluminium downstream from the arc-damaged aluminium rail inserts has yet to be explained.
- (vi) Evidence from arc-damage on aluminium suggests, and the depth of surface melting on copper rails indicates, that the P-P 'mass ablation' model results in a prediction of ionized mass which is too high.
- (vii) There was strong evidence for the existence of plasma turbulence at the surface of the rails.
- (viii) Different damage effects were observed on two rail sets, in that the number of arc-tracks was appreciably less than usual. This seemed to correlate best with rail surface history, but the evidence was inconclusive.
- (ix) There is convincing evidence that current conduction paths can occupy considerably less than the full rail height.
- (x) For the three sets of rails used at a peak current of 130 kA, post-shot rail curvature was significantly greater on the negative rail, implying that power dissipation was greater there.
- (xi) In the railguns used in this study, the I^2R heating contribution to rail damage was undetectable.
- (xii) Silica-filled-epoxy rail channels (or rails-within-the rail) survived well. Epoxy damage was no greater than adjacent copper damage, and general damage across the rails was no worse (peak-to-peak) than on the rails of other copper-foil shots.
- (xiii) When aluminium was used as the plasma initiating foil, first 'plate-out' occurred at the site corresponding to peak armature power. Subsequent plate-out was patchy and unpredictable for much of the rail length. This was interpreted as indicating that there was a cool layer 'attached' to the rear of the projectile. Small pieces of foil unconsumed in the initial blast were protected there until swept out occasionally, to be consumed and dumped onto the rails.
- (xiv) The RIPAL experiments provided evidence that material is transported from the negative rail to the positive. No evidence on the possibility of flow in the reverse direction was available. The mechanism of transport is open to conjecture.

4.5 Conjectural Model of the Developed Plasma

In Section 4.1.2 the development of the plasma was considered. A model for the plasma when it is in its steady state is now considered.

The combination of the rail damage evidence, particularly that described in Section 4.4.6, and the current distribution evidence discussed in Section 4.3.2 leads to the following model for the steady-state plasma.

The high temperature of the plasma causes material to evaporate from the bore walls. The plasma cannot transfer energy to the bore walls without its outer surface becoming cooler than its bulk. At the rails, therefore, there is a relatively cool layer of metal vapour. This layer is both optically dense [11,19], and of relatively low conductivity compared with the plasma. To maintain the appropriate high level of current, arcs 'punch' through this layer and connect the plasma to the rails via additional parallel paths. The plasma 'slides' along this layer, giving the impression that the cooler layer travels back along the walls. As discussed in Section 4.3.2, the current in the plasma bulk is diffusely distributed.

Arc-root vapour jets, with velocities up to 1 km/s [12], inject vapour directly into the plasma, through the boundary layer, providing a significant source of vapour for ionization [12]. Arc tracks generated near the plasma front are probably followed preferentially by trains of arc roots. (Marshall has postulated the existence of arc-roots travelling from the rear to the front [9]). Even with semi-continuous surface melting, tracks may not be obliterated, as following arc-roots would 'renovate' the track.

Turbulence at the rail walls occasionally causes metal vapour from the boundary layer to pass over the non-rail bore surfaces and thereby partly obscure the view of the plasma through the polycarbonate walls. This effect is demonstrated in the RIP 305 streak photograph particularly. (Fig. 24(a)).

The turbulence also causes the thickness of the colder layer to fluctuate, and sometimes to become very thin. Due to the closeness of the hot body of the plasma to the rail surface, conduction of current between the rail and the plasma then becomes predominantly diffuse and ohmic. The broadness of the damage, in contrast to the damage due to arc roots, reflects the diffuse nature of the conduction. This broad damage is perhaps closer to the general nature of the interaction implied and envisaged in the P-P model. This interaction may occur over only a portion of the plasma length or rail height, or at one rail-plasma surface and not at the other.

Consequently the rail surfaces may show both arc-track and diffuse types of damage across the same bore section, although arc tracks will probably not be present in a very close encounter between the plasma and a rail surface. An example can be seen on the negative rail in Fig. 38(c). Here two arc-tracks can be seen at the rail edge, but they are isolated from the diffuse damage band.

The above two paragraphs are thought to be a plausible explanation for the variation in damage in regions where the plasma is considered to be well established. Evidence points to there being other damage mechanisms in action in the plasma formation and development stage, as noted in Section 4.4.1.

The arc-root model described here has implications for rail damage and ionized mass estimates. The vapour layer at the rail surface is now seen as having significant thickness. It will reduce the radiant energy component at the rail surface, and a greater fraction of the energy will cause melting. Rail damage will be higher and ionized mass (from direct radiant energy) will be lower than might be expected from a P-P prediction. In the arc-root phase some sort of dynamic equilibrium must be established between vapour-layer thickness and the rail surface-energy that generates the layer.

Whether ionized mass is gained by the plasma predominantly by P-P type ablation, and to what extent arc-root vapour-jetting might contribute, could perhaps be resolved by a RIPLAM-style reduced-rail-surface experiment. If the P-P model is valid, then halving the copper surface in the rails should roughly halve the ablation rate. This should be easily detectable as a velocity improvement in a long gun. If, on the other hand, arc-jetting is the primary source of vapour for ionizing (within the plasma as opposed to at its surface), then no change in performance would be expected, as the number of arc-roots would probably be the same in both cases. On this subject, Cobine [12] states that metallic vapour jets originating at cathode spots are the principal source of vapour in the vacuum arc.

5. SUMMARY AND CONCLUSIONS

5.1 Summary and Discussion

This report has dealt with the equipment developed for, and with the experiments performed in, railgun studies aimed at understanding the plasma armature and rail damage.

The particular features of the equipment used for these purposes were the clear polycarbonate gun-bodies and the powder-gun injector.

The powder-gun injector introduced new problems because the experimental methods used successfully in static-start railguns were not applicable. These problems were solved by:

- (1) developing a new projectile design based upon nested plastic pyramids with a copper foil on plastic film inserted between the rear end pyramids such that the foil was protected from the powder gun blast, while maintaining a light but positive pressure against the rail surfaces.

- (ii) the use of an injector with a scored steel diaphragm to ensure proper confinement and burning of the powder.

With the above injector and projectile design, injection velocities in the range 1.2 to 1.4 km/s were obtained with good repeatability and with excellent obturation throughout the shot life and with reliable connection of electrical power after the projectile entered the railgun.

Examination of the plasma streak photographs and the current and voltage records produced:

- (i) a mechanism for the foil-to-plasma transformation,
- (ii) evidence of a relatively large gas pressure drive during plasma development, and
- (iii) estimates of plasma length.

In addition, detailed examination of the current and voltage records enabled the inductance and resistance components present during charging of the storage inductor and during the inductive drive after crowbar to be determined.

Magnetic pick-up coils were used to cross-check the plasma position, as given by the streak photographs, and to infer the current distribution in the plasma. Interpretation of the pick-up coil waveforms was assisted by reference to a look-up table of waveforms to be expected at various distances from various length plasmas with various current distributions. The pick-up coils showed that current is sometimes symmetrically distributed over the length of the plasma and sometimes is concentrated at the leading edge with a distribution tapering off to the rear. It was clear that the current is generally not uniformly distributed over the full length of the plasma. When examined in conjunction with streak photographs the pick-up coil waveforms showed that opaque layers could be present between the plasma and the bore walls.

Rail damage was considered in terms of armature power, current magnitude and type of arc tracks both for conventional and for experimental rails with aluminium and silica/epoxy inserts. Even though injection at velocities above 1 km/s was used, rail damage was still unacceptable in the breech region. Based on a subjective comparison of rails from aluminium foil-80 kA firings, it is not certain that any improvement was gained above 400 m/s. From a damage aspect, copper has limitations in the plasma-arc environment. On the other hand, copper-tungsten was used as electrode material in both crowbar and main switches in MRL railgun experiments with great success [7]. As these electrodes showed little damage even after extended use, this material was considered for the rails during the early experimental programs. However its supply in suitable sizes, and difficulties of machining, presented major obstacles to its use.

Drawing on damage evidence, and existing ideas about the nature of arc-electrode interfaces, a plasma-arc model was developed. A feature of the

model is its explanation of the presence of the arcs that produce rail track-damage. These arcs are believed to be an inevitable consequence of the development of a reasonably stable low-conductivity metal vapour layer at the rail surface. Electrical conduction through this layer is primarily by multiple arc breakdown.

An experiment was proposed for obtaining data on the relative contributions to armature mass-addition due to ionization by radiant energy at the rail, and from direct ionization of injected arc-root vapour-jet material.

5.2 Conclusions

The major conclusions from these investigations are as follows:

- (i) For the railguns used at MRL, injection at 1 km/s does not reduce rail damage to a degree that is likely to allow repeated use of the rails.
- (ii) Since early rail damage correlates most directly with the energy required to vapourize the initiating foil, means other than foil explosion should be studied for establishing the plasma.
- (iii) The 500 mm gun was too short to be an effective test bed. The plasma initiation and development phase occupied too much of the in-bore life, and the projectile received a 'non-electric' velocity boost during this time.
- (iv) Arc damage was particularly severe on aluminium rail segments. This feature detracts from the use of aluminium as a rail which otherwise is attractive due to its high vapourization and ionization energies.
- (v) The single experiment using insulating channels along the rail length showed that this scheme for reducing copper surface has potential. Performance was at least equal to that for similar shots with conventional rails, and there was some indication that the plasma was more compact.
- (vi) As the exit velocity in these short guns was unlikely to be significantly reduced by armature mass addition (ablation limiting), the constant velocity phase in the 130 kA shots was probably the result of excessive projectile friction. While 'stacked-pyramid' projectile construction ensured excellent obturation, some variant may be needed for higher-power railguns to reduce friction.
- (vii) The accumulation of evidence pointed to there being two mechanisms for conduction of current between the plasma and rails. One mechanism was a diffusive (ohmic 'contact') mode, and was associated with much higher levels of visible damage. The other mechanism was arc conduction through a low conductivity boundary layer. This latter mechanism results in the arc-track type of damage.

- (viii) Rail energy density during arc-mode conduction was seen as being lower than the Parker-Parsons (et alia) ablation model assumes.
- (ix) The type and extent of arc-track damage might depend on surface effects related to the history of the rail. More experimentation is needed if conclusive evidence is to be obtained.

6. ACKNOWLEDGEMENTS

This work was carried out as part of a joint program with the US Defense Advanced Research Projects Agency (DARPA).

Dr R.A. Marshall was the driving force behind the Ripper railgun design, and the injector and projectile development. Although he left MRL in the early stages of this work his availability for discussion and comment has been much appreciated.

Dr A.J. Bedford devised and supplied the striped rails for the RIPLAM experiment.

Mr G.A. Clark and Mr W.A. Jenkins were closely involved in the development and experimental aspects of the whole electromagnetic launcher program at these Laboratories and their contributions at all stages are gratefully acknowledged. Mr Jenkins' notes on the injector and projectile development were used in compiling Section 3 of this Report.

Mr J. Ferrett, Mr G. Harrison and Mr S. Pattie also provided much valuable technical assistance.

Finally, the authors wish to thank Dr C.I. Sach, Head of Electrodynamics Group, for his encouragement and his constructive criticism in the preparation of this Report.

7. REFERENCES

1. Bedford, A.J., Clark, G.A. and Thio, Y.C. 'Experimental Electromagnetic Launchers at MRL' MRL-R-894, Materials Research Laboratories, Melbourne, Victoria, Australia 1983.
2. Macintyre, I.B. 'High Speed Photographic Analysis of Railgun Plasmas Proceedings', 16th International Congress on High Speed Photography and Photonics, Strasburg, France 1984, pp 938-945.
3. Kowalenko, V., 'Analysis of a Series of Electromagnetic Launcher Firings', MRL-R-1053, Materials Research Laboratories, Melbourne, Victoria, Australia. 1986.
4. Sadedin, D.R. and Stainsby, D.F. 'Experimental Investigation of a Three-stage Railgun Incorporating Puff-switching', MRL-R-1056, Materials Research Laboratories, Melbourne, Victoria, Australia 1986.
5. Bedford, A.J. 'Rail Damage in a Small Calibre Railgun', IEEE Trans. Magnetics, Vol MAG-20, No 2, March 1984, pp 348-351.
6. Clark, G.A. and Kowalenko, V. 'Temperature Measurement of a Free Flowing Railgun Plasma', MRL Report in preparation. Materials Research Laboratories, Melbourne, Victoria, Australia 1986.
7. Clark, G.A. and Thio, Y.C. 'Design and Operation of a Self Activating Crowbar Switch', IEEE Trans Magnetics, Vol MAG-20, No 2, March 1984, pp 364-365.
8. Stainsby, D.F. 'Experimental Study of Plasma Structure in a Small Railgun', MRL-R-1057, Materials Research Laboratories, Melbourne, Victoria, Australia 1986.
9. Marshall, R.A. 'Structure of Plasma Armature of a Railgun', 3rd IEEE Symposium on Electromagnetic Launch Technology, Austin, Texas, April 1986.
10. Chung, M.J. 'Initial Acceleration for Electromagnetic Launchers: A Feasibility Study on Chemical Propellants', MRL-TN-748. Materials Research Laboratories, Melbourne, Victoria, Australia, 1983.
11. Parker, J.V., Parsons, W.M., Cummings, C.E. and Fox, W.E. 'Performance Loss Due to Wall Ablation in Plasma Armature Railguns', AIAA 18th Fluid Dynamics and Plasmadynamics and Lasers Conference, Cincinnati, Ohio, July 16-18, 1985.
12. Lafferty, J.M. (Ed.). Vacuum Arcs: Theory and Application, John Wiley and Sons, 1980, Chapter 1.
13. Parker, J.V., Peterson, D.R., Cummings, C.E. and Fowler, C.M. 'Measurement of Railgun Arc Characteristics', LA-UR-822177 Los Alamos National Laboratory, Los Alamos, New Mexico, 87545, 1982.

14. Kowalenko, V. 'Experimental Results from Railgun Firings Involving Magnetic Flux Probes', MRL Technical Note MRL-TN-509, Materials Research Laboratories, Melbourne, Victoria, Australia, 1986.
15. McLachlan, A.D. Private communication, Materials Research Laboratories, Melbourne, Victoria, Australia, 1986.
16. Baressi, J. Unpublished material, Materials Research Laboratories, Melbourne, Victoria, Australia, 1983.
17. Clark, G.A. and Bedford, A.J. 'Performance Results of a Small-Calibre Electromagnetic Launcher', MRL-R-917, Materials Research Laboratories, Melbourne, Victoria, Australia, February 1984.
18. Lafferty, J.M. (Ed.). Vacuum Arcs: Theory and Application, John Wiley and Sons, 1980, Chapter 7.
19. Richardson, D.D. 'Spectroscopic Studies of a Railgun Muzzle Flash', MRL-R-952, Materials Research Laboratories, Melbourne, Victoria, Australia, February 1985.
20. Seely, S. Introduction to Electromagnetic Fields, McGraw Hill, 1958, p 157.

APPENDIX 1. PARAMETERS OF THE 5 EXPERIMENTS AND 12 SHOTS DISCUSSED IN THIS REPORT

SHOT PARAMETER	GROUP 1 (RIP 3 -)			GROUP 2 (RIP 3 -)			GROUP 3 (SUBAC -)				GROUP 4 (RIPAL -)		GROUP 5 RIFLAM
	03	05	06	07	10	11	2	3	4		1	2	
Driven Projectile Mass (g)	.715	.728	.769	.77	.749	.746	.88	.88	.88		.80	.80	.86
Foil Mass (mg) (1)	66	38	30	38	33	35	58	52±6	51		55	45.8	48.7
Foil Material (1)	Al.	Al.	Al.	Al.	Al.	Al.	CCP	CCP	CCP		CCP	CCP	CCP
Driven Projectile Construction (2)	5A	5A	5A, G	5	5	5	5	5	5		5	4+PE	5
Injected Projectile Mass	.951	.933	.971	.96	.94	.94	1.248	1.245	1.242		1.16	1.09	1.24
No of Projective Pyramids (2)	/	/	/	/	/	/	1+T	1+T	1+T		1+T	1+T/PE	1+T
Injection Velocity (km/s), V_{inj}	1.36	1.40	1.36	1.40	1.40	1.40	1.23	1.36	1.255		1.295	1.300	1.230
ϕV_{inj} Tolerance ($\pm \frac{m}{s}$)	40	20	40	20	50	50	50	90	25		5	20	5
Exit Velocity (km/s), V_{exit}	1.80	1.80	1.80	2.15	2.05	2.05	1.70	1.75	1.775		1.790	1.780	1.775
ϕV_{exit} Tolerance ($\pm \frac{m}{s}$)	20	20	20	50	50	50	25	25	25		10	20	25
Electric Shot Start (3) (mm ± 3)	45	32	40	4	47	-13	4	14	4		6	6.4	28(4)
Shot Travel (electric) (mm ± 4)	403	416	408	442	399	(5)	442	432	442		440	440	418
Time to Peak Muzzle Volts (1s)	-	52	-	31	-	-	37	-	6 40		40	6 30	35

NOTES: (1) CCP indicates copper-clad polyester. (2) Variants of pyramid or stack:- A = 2nd and 4th pyramids cut down, Mass of copper was 82% of G = glued stack, T = 6th pyramid trimmed 0.1 mm at rail faces, tabulated foil mass. PE = polyethylene pyramid.
(3) Position relative to centre-line (4) Delay setting increase caused later start.
of rail current connector. (5) Meaning of Travel for negative (premature) start is unclear.

APPENDIX 1 (CONTD) B-DOT DATA FOR PLASMA POSITION AND LENGTH

Time to Zero-cross-over (Xn) Referenced to Electric Shot-start,
and times from Xn to 1st Peak (P₁) and 2nd Peak (P₂)(2) (Is)

BONE (1) POSITION (mm)	WAVE- FORM FEATURE	RIP 3 -			SUBMC -			RIPAL -			RIPLAN
		05	06	07	10	11	2	4	1	2	
51	P ₁										-6
	X ₁										20
	P ₂										+3.5
135	P ₁				-9.2			-6.5		-12.5	-8.6
	X ₂				78			101		102	87.5
	P ₂				+8.8			+9.5		+14	+9
160	P ₁				-9.8			-7.5		-10.5	-9.5
	X ₃				X ₂ +16.8			X ₂ +15		X ₂ +18	X ₂ +19
	P ₂				+9.2			+8.5		+16	+12.5
285	P ₁	-18	-17	-12	-9.5			-10			
	X ₄	196	185	191	165			197			
	P ₂	+19	+15	+12	+16			e14			
310	P ₁	-20	-16.3	-12	-10.4			-10			
	X ₅	X ₄ +19.2	X ₄ +14.5	X ₄ +13.4	X ₄ +13.4			222.5			200.4
	P ₂	+19	+17.5	13.5	+15.2	14	14.5				

APPENDIX 1 (CONT'D) B-DOT DATA FOR PLASMA POSITION AND LENGTH

Time to Zero-cross-over (X_n) Referenced to Electric Shot-start,
and times from X_n to 1st Peak (P_1) and 2nd Peak (P_2)⁽²⁾ (I_s)

BORE ⁽¹⁾ POSITION (mm)	WAVE- FORM	FEATURE	RIP 3 -			SUBMC -			RIPAL -			RIPLAM
			05	06	07	10	11	2	4	1	2	
360		P_1										
		X_6						-10	-10.4	-12	-9	-8
		P_2						265	252	245.5	243	229±2
385		P_1						18		14	+18	±11
		X_7										
		P_2										
410		P_1										
		X_8										
		P_2										
447		P_1										
		X_9										
		P_2										
±1		SHOT										
		OUT										

(1) Referenced to rail-connector centre-line. Refer to shot-start data calculating shot displacement.

(2) For noisy peaks the times are mean values.

APPENDIX 2

Calculated Magnetic Pick-up Coil Waveforms

Magnetic pick-up coils may be used to infer the distribution of current in the plasma, if they are oriented so as to link the plasma magnetic flux and to ignore the rail flux. The coil axis must be parallel to the gun axis to obtain such flux linkage. To properly interpret the waveforms obtained from pick-up coils (also called "B-dot" i.e. dB/dt coils) it is necessary to compare them with waveforms obtained by calculation for various plasma lengths, coil locations and current distributions.

A convenient distribution to begin with is uniformly distributed current, which may be divided into $M \times N$ filaments.

Consider a point P at height Y above the top of the railgun bore and midway between the rails (Fig 41).

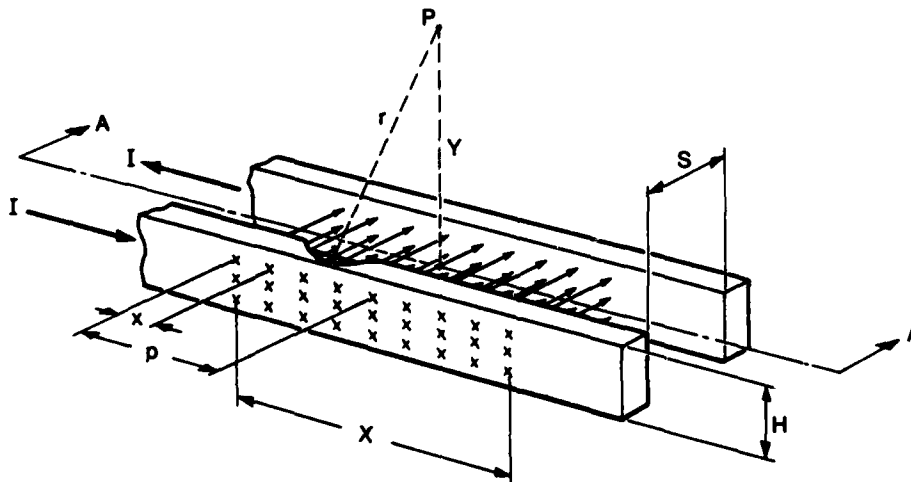


FIGURE 41 Geometry for calculation of magnetic flux density at a point P above the centre of the railgun bore, due to $M \times N$ filaments of current passing from one rail to the other.

Since P is at distance r from the centre of a general filament, as shown in Fig 42, the magnitude of the flux density, ΔB , at P due to the filament is [20]:

$$\Delta B = \frac{\mu_0 \Delta I}{2\pi r} \cos \alpha \quad (1)$$

where ΔI is the filament current and μ_0 is the permeability of free space.

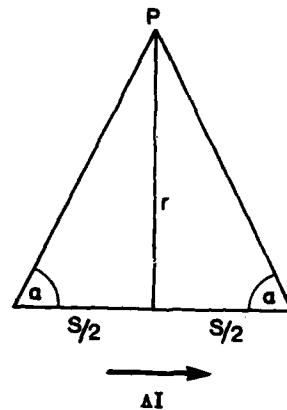


FIGURE 42 Point P is located distance r from the mid point of current filaments of length S

If the general filament is located at distance x from the left hand end of the plasma, and is distance h below the top of the plasma, (Fig 43), distance r is:

$$r = [(\rho - x)^2 + (Y + h)^2]^{1/2} \quad (2a)$$

and $\cos \alpha$ from Fig. 42 is given by:

$$\cos \alpha = \frac{S}{2\sqrt{(r^2 + \frac{S^2}{4})}} \quad (2b)$$

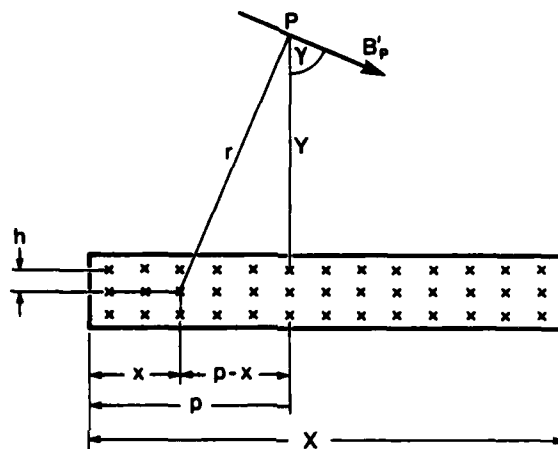


FIGURE 43 Geometry for calculation of distance r

The total field at P is found by adding the horizontal and vertical field components due to all the current filaments. For the general filament located at (x, h) the horizontal and vertical components of the field at P are (Fig 44):

$$\Delta B_H = \Delta B \sin \gamma = \Delta B \frac{(Y + h)}{r} \quad (3)$$

$$\Delta B_V = -\Delta B \cos \gamma = \Delta B \frac{(x - p)}{r} \quad (4)$$

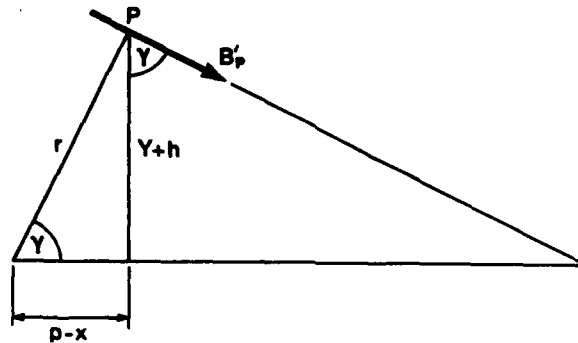


FIGURE 44 Geometry for horizontal and vertical components of flux density at P due to filament at (x, h)

If in distances X and H there are N and M equally spaced filaments respectively, then:

$$x = (n-1) \frac{X}{(N-1)} \quad (5)$$

$$h = (m-1) \frac{H}{(M-1)} \quad (6)$$

where the general filament at (x, h) is the (n, m)th filament.

Combining the above expressions and summing over all the filaments yields the total horizontal and vertical flux density components at P to be:

$$B_H = \frac{\mu_0 IS}{4\pi NM} \sum_{n=1}^N \sum_{m=1}^M \frac{Y + \frac{(m-1)}{(M-1)} H}{[(p - \frac{(n-1)}{(N-1)} X)^2 + (Y + \frac{(m-1)}{(M-1)} H)^2 + \frac{S^2}{4}]^{1/2}} \quad (7)$$

and:

$$B_v = \frac{\mu_0 IS}{4\pi NM} \sum_{n=1}^N \sum_{m=1}^M \frac{\frac{(n-1)}{(N-1)} X - p}{[(p - \frac{(n-1)}{(N-1)} X)^2 + (Y + \frac{(m-1)}{(M-1)} H)^2 + \frac{S^2}{4}]^{1/2}} \times \frac{1}{[(p - \frac{(n-1)}{(N-1)} X)^2 + (Y + \frac{(m-1)}{(M-1)} H)^2]} \quad (8)$$

where I is the rail current, i.e. $I = MN AI$.

If a magnetic pick-up coil is oriented so that its cross section is normal to the horizontal component of the flux, that is the coil axis coincides with the direction of the barrel axis, the voltage induced in the coil, e, is dependent only on the B_H component, i.e.

$$e = NA \frac{dB_H}{dt} \quad (9)$$

where N is the number of turns on the coil, A is the cross sectional area presented to the flux and dB_H/dt is the time rate of change of flux density. If the rate of change of flux is due to the plasma moving past the pick-up coil with velocity $v = dx/dt$, then

$$\frac{dB_H}{dt} = \frac{dx}{dt} \frac{dB_H}{dx} \quad (10)$$

If the velocity, v, is constant, (9) and (10) yield:

$$e = K \frac{dB_H}{dx} \quad (11)$$

where $K = Nav$.

The rate of variation of Eqn (7) with respect to x therefore gives the magnetic pick-up coil voltage waveform, at constant plasma velocity.

Equations (7) and (8) give the field components for equal current AI in each filament. If the number of filaments per unit length is the same horizontally and vertically the results are for a uniform current distribution.

Fig 46 shows the results from evaluation of Eqns (7) and (11) for 6 H/S values and 6 distances (Y) above the bore, for uniform current distribution. The boxes below the waveforms represent the plasma geometry in a square bore railgun and are scaled so that each point on the waveform gives the induced voltage when the position coil is at that horizontal position relative to the plasma.

By applying a weighting factor to the numerators of Eqns (7) and (8) the field strengths and induced voltages due to other current distributions may be found. For example, if the current density rises linearly from zero at the left hand end of the plasma to a maximum at the b^{th} filament and then falls linearly to zero at the right hand end, (Fig 45a), the factor to be applied to the numerator inside the summation in Eqn (7) is:

$$\frac{2(n-1)}{(b-1)} \quad \text{if } 1 < n \leq b$$

and
$$\frac{2(N-n)}{(N-b)} \quad \text{if } b \leq n \leq N$$

In terms of the gun geometry, this means that the current varies linearly in the barrel-axis direction.

Figs 47 and 48 show the calculated pick-up coil waveforms for current linearly distributed about the centre of the plasma and for current that rises linearly to its peak a quarter of the distance from the left hand end and falls to zero over the remainder of the plasma.

Another distribution of interest is one in which the current density is constant from the left hand end to the b^{th} filament and then falls linearly to zero at the right hand end (Fig 45b). The factors to be applied to the numerator for this case are:

$$\frac{2N}{(N+b)} \quad \text{if } 1 < n \leq b$$

and,
$$\frac{2N}{(N+b)} \frac{(N-n)}{(N-b)} \quad \text{if } b \leq n \leq N$$

Waveforms for the case where the current is uniformly distributed over half the plasma and falls linearly to zero at the other end are given in Fig 49.

The plots of calculated pick-up coil waveforms show that a great variety of waveforms is produced according to the height above the bore, the length of the plasma and the current distribution. Study of the waveforms leads to the following conclusions.

- (i) The pick-up coils should be as close as possible to the railgun bore. The closer the coils are, the greater is the variety in waveforms and hence the more easily can the current distribution and plasma length be deduced by inspection. All waveforms become sinusoidal if the pick-up coils are several bore heights from the plasma. The coils need to be within one bore height of the plasma surface in the case of plasmas five to ten times as long as they are high and closer for shorter plasmas.
- (ii) The peaks of the waveforms correspond closely to the ends of the plasma only for uniform current distributions and then only for plasmas that are at least as long as they are high. For plasmas that are shorter than their height, the peaks occur a considerable distance either side of the plasma.
- (iii) Uniform current distribution is characterized by sharp peaks separated by an inflection or flat region that becomes more pronounced as the plasma length increases and the distance from the plasma decreases. Uniform current distribution is also characterised by waveforms which have odd-function symmetry, i.e. waveforms which are symmetrical about the horizontal axis.
- (iv) Linear current distributions symmetrical about the centre of the plasma produce relatively rounded waveforms which are symmetrical about the horizontal axis.
- (v) Unsymmetrical current distributions produce waveforms with a sharper peak corresponding to the region of greatest current density and a bulbous peak corresponding to the region of lower current density.

It should be remembered that the waveforms assume constant plasma velocity. When the plasma is long (e.g. 100 mm), the velocity may alter significantly during the passage of the plasma past the pick-up coils. Increasing velocity would sharpen the trailing peak and increase its amplitude. The converse is also true, i.e. a decreasing velocity would broaden the trailing peak and decrease its amplitude.

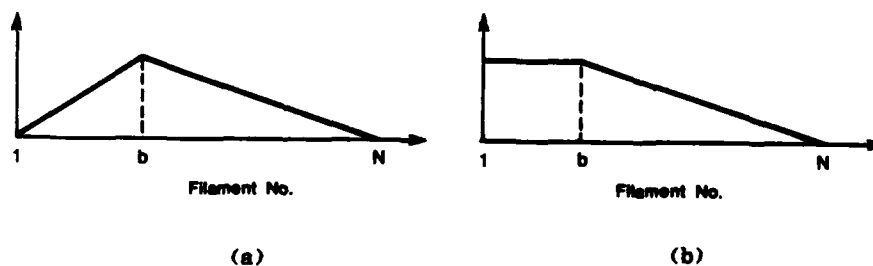


FIGURE 45 Linear and uniform-plus-linear current distributions

UNIFORM CURRENT DISTRIBUTION

CURRENT
DENSITY



X

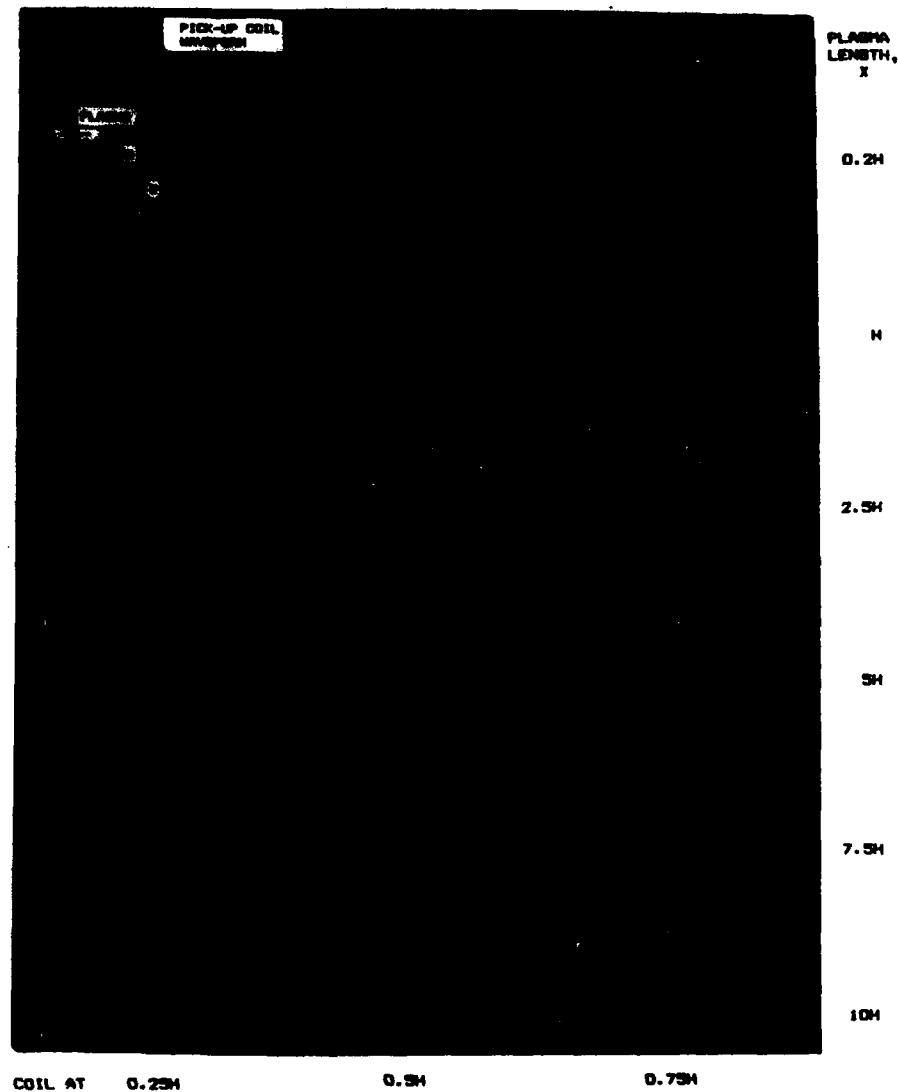


FIGURE 46 Pick-up coil waveforms for uniform current distribution within the plasma.

Waveforms are given for pick-up coils which are located (i) $0.25H$, (ii) $0.5H$ and (iii) $0.75H$ from the plasma surface where H is the size of the bore of a square bore railgun. The plasma cross-section along the length of the railgun is shown beneath each waveform. The plasma length, X , varies from $0.2H$ to $10H$. Plasma motion is right to left.

UNIFORM CURRENT DISTRIBUTION

CURRENT
DENSITY



X

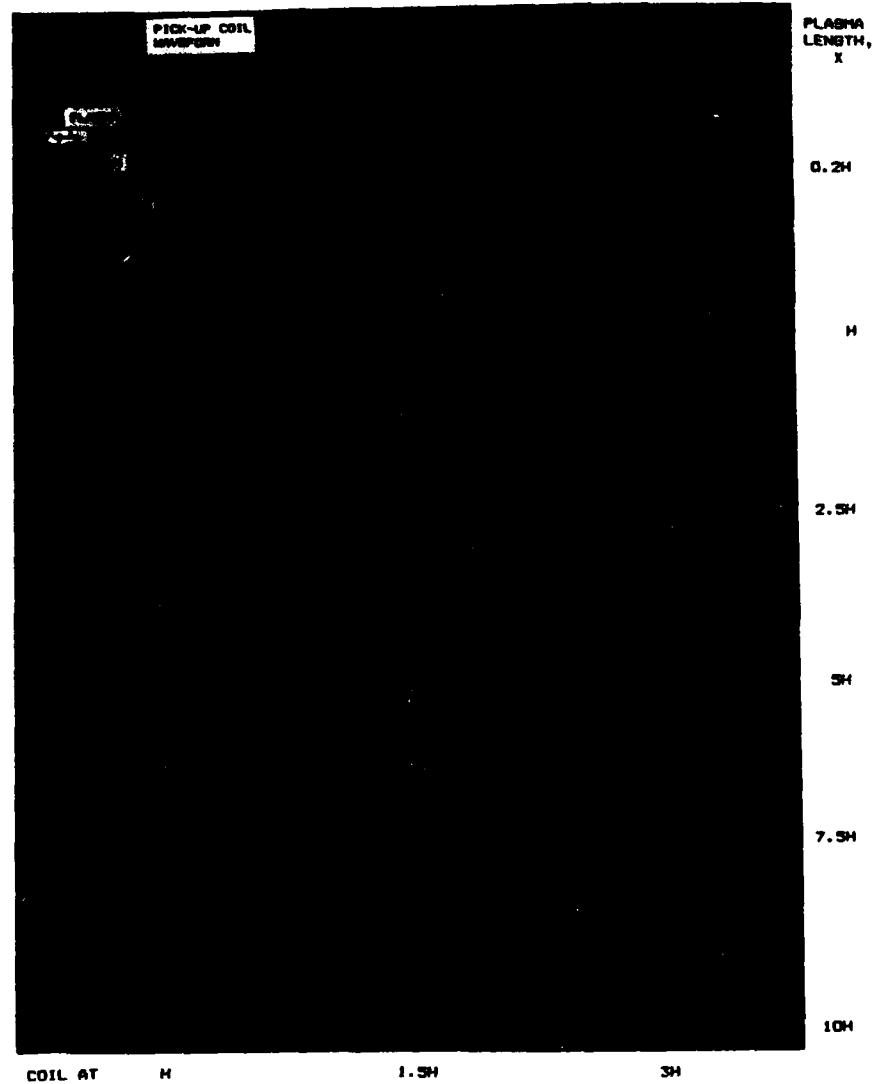


FIG. 46 CONT Pick-up coil waveforms for uniform current distribution within the plasma.

Waveforms are given for pick-up coils located (iv) H, (v) 1.5H and (vi) 3H from the plasma surface.

LINEAR SYMMETRIC CURRENT DISTRIBUTION

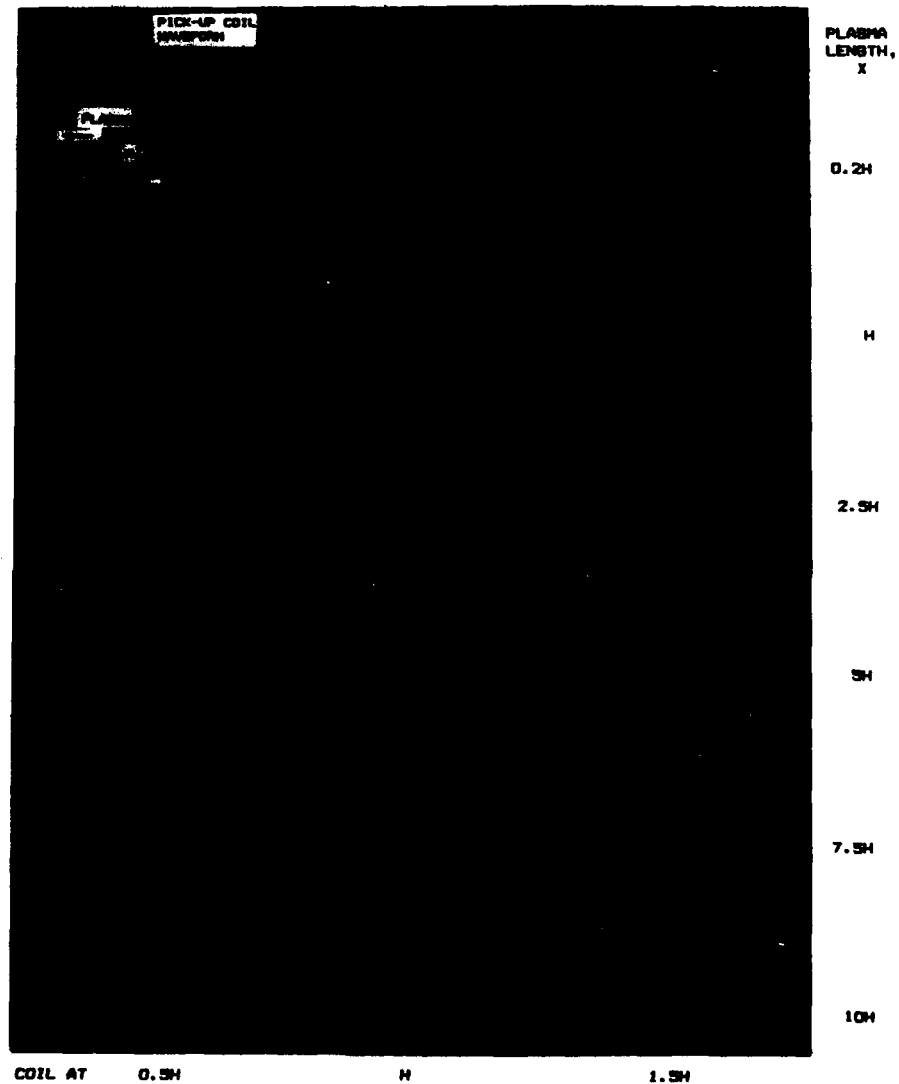
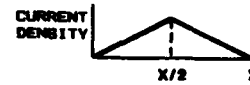


FIGURE 47 Pick-up coil waveforms for linear symmetric current distribution within the plasma.

Waveforms are given for pick-up coils located (i) $0.5H$, (ii) H and (iii) $1.5H$ from the plasma surface.

LINEAR ASYMMETRIC CURRENT DISTRIBUTION

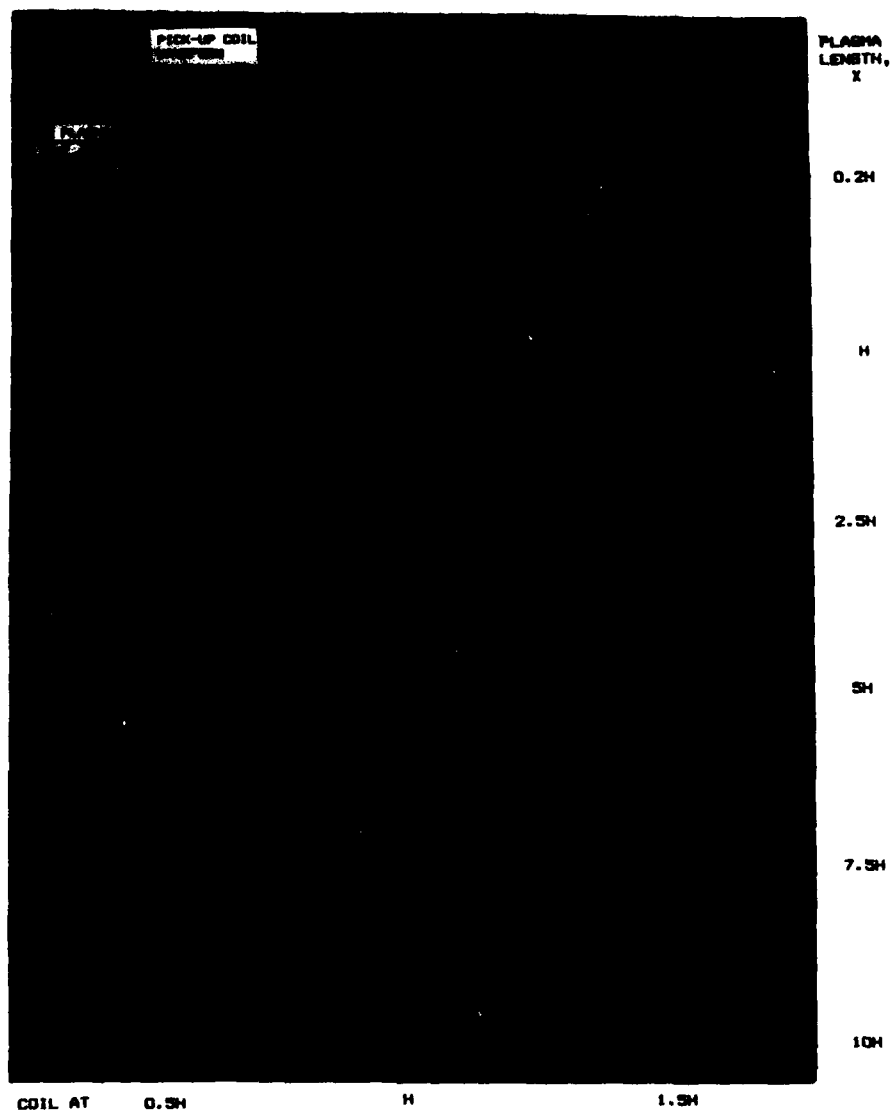


FIGURE 48 Pick-up coil waveforms for linear asymmetric current distribution within the plasma.

Waveforms are given for pick-up coils located (i) 0.5H, (ii) H and (iii) 1.5H from the plasma surface.

UNIFORM PLUS LINEAR FALL CURRENT DISTRIBUTION

CURRENT
DENSITY

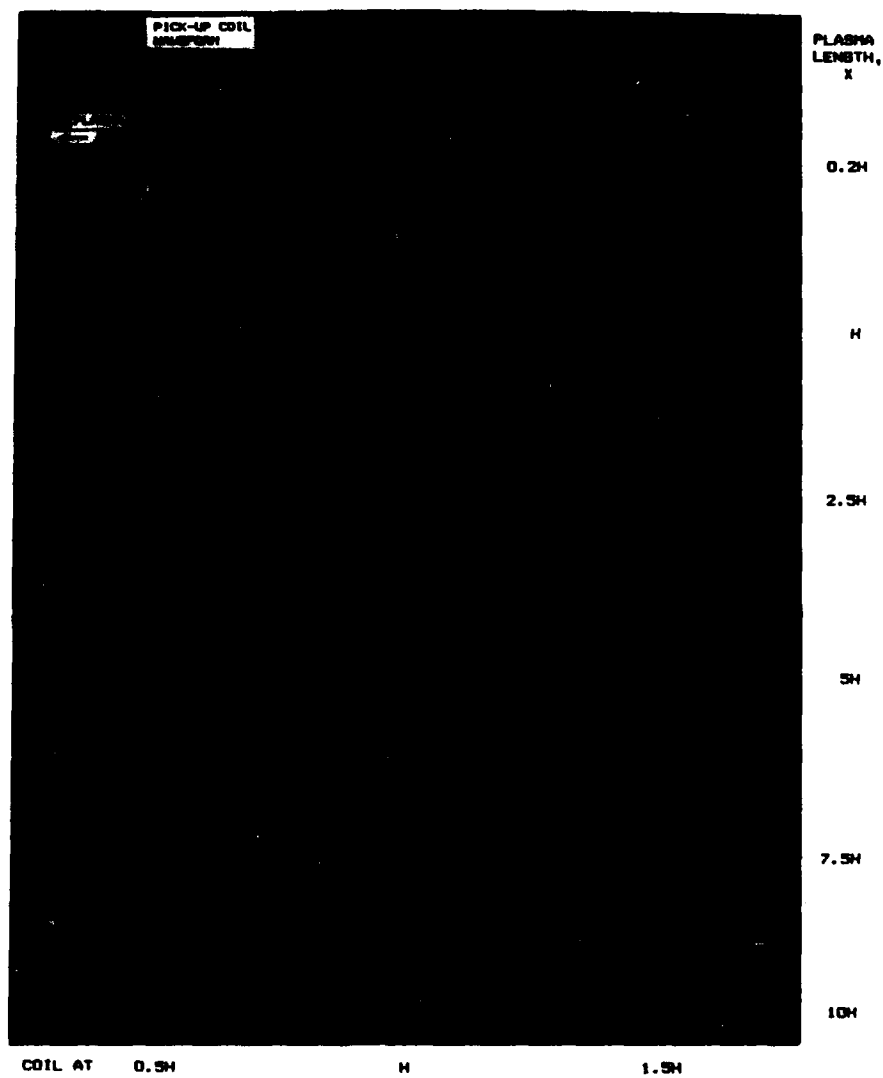


FIGURE 49 Pick-up coil waveforms for uniform followed by linear fall current distribution within the plasma.

Waveforms are given for pick-up coils located (i) $0.5H$, (ii) H and (iii) $1.5H$ from the plasma surface.

SECURITY CLASSIFICATION OF THIS PAGE

UNCLASSIFIED

DOCUMENT CONTROL DATA SHEET

REPORT NO.

MRL-R-1055

AR NO.

AR-005-134

REPORT SECURITY CLASSIFICATION

Unclassified

TITLE

Experiments with a small injected railgun

AUTHOR(S)

D.F. Stainsby and
D.R. Sadedin

CORPORATE AUTHOR

Materials Research Laboratory, DSTO
PO Box 50,
Ascot Vale, Victoria 3032

REPORT DATE

June 1987

TASK NO.

DST 82/212

SPONSOR

DSTO

FILE NO.

G6/4/8-3220

REFERENCES

20

PAGES

118

CLASSIFICATION/LIMITATION REVIEW DATE

CLASSIFICATION/RELEASE AUTHORITY

Chief, Underwater Systems Division MRL

SECONDARY DISTRIBUTION

Approved for Public Release

ANNOUNCEMENT

Announcement of this report is unlimited

KEYWORDS

→ Railgun,
Optical Fibers
InjectorsElectric guns , Rail damage
Electromagnetic launcher

SUBJECT GROUPS

0074B

ABSTRACT

→ Experiments aimed at gaining insight into the plasma arc and rail damage in railguns are described and discussed. The railgun body was constructed of clear polycarbonate to allow streak photographs of the plasma to be taken. A powder-gun injector was used to reduce initial rail damage. The development of the injector and projectiles is described. Rails with plain surfaces, alternating aluminium inserts, and lengthwise insulating stripes were studied. Both aluminium and copper foils were used for plasma initiation. The results from the experiments enable plasma formation to be explained in terms of the vapourization energy of the foil and material taken up from the bore. Magnetic pick-up coils were used to study plasma length and current distribution and the theory of the coils and a look-up table of calculated waveforms is given. A non-metallurgical study of rail damage has been made, and damage mechanisms are identified. A qualitative model of the plasma is described, in which two current conduction modes at the rail-plasma boundary are identified. These are an ohmic (direct contact) mode, and an arc-root mode. The severe rail-surface damage observed is thought to be due to boundary conduction in the ohmic mode rather than to the current-carrying arc-roots leaving and entering the rails. *Keywords:*

SECURITY CLASSIFICATION OF THIS PAGE

UNCLASSIFIED